Breaking Symmetry with Light: Ultrafast Optical Control of Structural Order in Solids

Zhiyang Zeng

St Peter's College
University of Oxford

A thesis submitted for the degree of Doctor of Philosophy

Michaelmas 2025

Abstract

This thesis explores how light can be used to induce and control symmetry-breaking phenomena in solids through resonant excitation of lattice vibrations. Within the framework of nonlinear phononics, the coherent excitation of infrared-active phonon modes by intense terahertz pulses transiently reshapes the crystal potential energy landscape, providing a means for dynamic and selective control of material functionalities. Two case studies are presented. The first demonstrates the light-induced emergence of chirality in the non-chiral crystal BPO_4. By selectively exciting infrared phonons with linearly polarised light, it is shown that the system can be driven into a transient chiral state on ultrafast timescales. The second example focuses on the ferroaxial material $RbFe(MoO_4)_2$, where a conjugate axial field associated with circular phonon excitation is experimentally identified and shown to couple directly to the ferroaxial order parameter. Together, these results highlight the effectiveness of light as a symmetry-selective control parameter for lattice-driven phenomena. The symmetry-based approaches developed in this work are general and are expected to be applicable beyond the specific materials studied. The coherent excitation of phonon modes in strongly correlated systems, together with the use of light fields featuring tailored or complex polarisation profiles, promises a rich landscape of unexplored opportunities for non-equilibrium phase control and the discovery of emergent phenomena beyond equilibrium limits.

Breaking Symmetry with Light: Ultrafast Optical Control of Structural Order in Solids

Zhiyang Zeng

St Peter's College

University of Oxford

A thesis submitted for the degree of

Doctor of Philosophy

Michaelmas 2025

This thesis is dedicated to my family.

Acknowledgements

I would like to express my deepest gratitude to my advisor, Prof. Andrea Cavalleri, for his advice, encouragement, and support throughout my doctoral studies. His insightful advice, patience, and scientific passion have been invaluable in shaping both my research and my approach to problem solving.

I am also profoundly grateful to my co-advisor, Prof. Paolo G. Radaelli, for his insightful guidance and invaluable contributions to the research projects presented in this thesis, as well as for fostering an inspiring scientific environment that has greatly shaped my development as a researcher.

I sincerely thank my collaborators and colleagues at the Max Planck Institute for the Structure and Dynamics of Matter (MPSD) for their stimulating discussions, technical assistance, and the spirit of collaboration that made every stage of this work both productive and rewarding. In particular, I would like to acknowledge Dr. Michael Först, Dr. Michael Fechner, Dr. Michele Buzzi, Dr. Daniele Nicoletti, and Dr. Eryin Wang for their valuable input and contributions to the research projects that form the core of this thesis. I am also thankful to all the other members of the condensed matter dynamics group for maintaining such a supportive and intellectually vibrant atmosphere.

Within the MPSD, I also had the privilege of collaborating with Prof. Philip J. W. Moll, Dr. Carsten Putzke, and Dr. Chunyu Guo (Mark), whose perspectives and expertise broadened the scope of my work. In addition, I am grateful to my colleagues at the Department of Physics at the University of Oxford, including Dr. Hariom Jani, Dr. Jack Harrison and Dr. Dharmalingam Prabhakaran, whose experimental insight and collaboration significantly enriched the depth and impact of this research. Their contributions and stimulating discussions have been a continuing source of inspiration throughout my studies.

During my DPhil research, I had the opportunity to engage in discussions with many inspiring scientists, among whom I am especially grateful to Prof. Roberto Merlin for his profound insights and stimulating conversations that have deeply influenced my scientific thinking. I would also like to thank Prof. Liuyan Zhao,

Prof. Lara Benfatto, Prof. Dominik Juraschek, Prof. Ankit Disa, Dr. Alexander von Hoegen, Prof. James McIver, Dr. Albert Liu, Dr. Roman Mankowsky, Prof. Guru Khalsa, and Dr. Takeshi Hayashida for their valuable discussions. Their perspectives have provided enriching external viewpoints that broadened the conceptual framework of my research and deepened my understanding of the underlying physics and experimental techniques.

I gratefully acknowledge the Max Planck Graduate Center for Quantum Materials (MPGC-QM), excellently led by Prof. Bernhard Keimer and coordinated by Dr. Zrinka Gattin, for providing an outstanding platform for scientific exchange and interdisciplinary collaboration, as well as for their financial and institutional support during my DPhil.

I am also thankful to St Peter's College and the Department of Physics at the University of Oxford for their academic hospitality and stimulating environment during my research, which significantly enriched the breadth and impact of my work.

Finally, I owe my deepest gratitude to my family for their unwavering love, patience, and belief in me. Their support has been the foundation of my perseverance and motivation throughout this endeavor.

Abstract

This thesis explores how light can be used to induce and control symmetry-breaking phenomena in solids through resonant excitation of lattice vibrations. Within the framework of nonlinear phononics, the coherent excitation of infrared-active phonon modes by intense terahertz pulses transiently reshapes the crystal potential energy landscape, providing a means for dynamic and selective control of material functionalities. Two case studies are presented. The first demonstrates the light-induced emergence of chirality in the non-chiral crystal BPO_4. By selectively exciting infrared phonons with linearly polarised light, it is shown that the system can be driven into a transient chiral state on ultrafast timescales. The second example focuses on the ferroaxial material $RbFe(MoO_4)_2$, where a conjugate axial field associated with circular phonon excitation is experimentally identified and shown to couple directly to the ferroaxial order parameter. Together, these results highlight the effectiveness of light as a symmetry-selective control parameter for lattice-driven phenomena. The symmetry-based approaches developed in this work are general and are expected to be applicable beyond the specific materials studied. The coherent excitation of phonon modes in strongly correlated systems, together with the use of light fields featuring tailored or complex polarisation profiles, promises a rich landscape of unexplored opportunities for non-equilibrium phase control and the discovery of emergent phenomena beyond equilibrium limits.

List of Publications

- **Z. Zeng**, M. Först, M. Fechner, D. Prabhakaran, P. G. Radaelli, A. Cavalleri. *Photo-induced non-volatile rewritable ferroaxial switching. Science* **390**(6769), 195–198 (2025). DOI: 10.1126/science.adz5230.
- **Z. Zeng**, M. Först, M. Fechner, M. Buzzi, E. B. Amuah, C. Putzke, P. J. W. Moll, D. Prabhakaran, P. G. Radaelli, A. Cavalleri. *Photo-induced chirality in a nonchiral crystal. Science* **387**(6732), 431–436 (2025). DOI: 10.1126/science.adr4713.
- **Z. Zeng**, M. Först, M. Fechner, X. Deng, A. Cavalleri, P. G. Radaelli. *The Piezochiral Effect.* arXiv:2510.21674 (2025).
- H. Jani, J. Harrison, S. Hooda, S. Prakash, P. Nandi, J. Hu, **Z. Zeng**, *et al. Spatially reconfigurable antiferromagnetic states in topologically rich free-standing nanomembranes. Nature Materials* **23**(5), 619–626 (2024). DOI: 10.1038/s41563-024-01806-2.

Contents

List of Publications **vi**

List of Figures **ix**

List of Tables **xi**

List of Abbreviations **xii**

1 Introduction **1**

1.1 Symmetry Breaking and Emerging Orders in Solids 1

1.2 Nonlinear Lattice Control 4

1.3 Development of Nonlinear Lattice Control 8

2 Experimental Techniques **15**

2.1 Tabletop Strong Field THz Generation 15

2.2 Time-resolved Measurements 17

2.3 Data Acquisition 20

2.4 Electro-optic Sampling 22

3 Light-induced Chirality **24**

3.1 Antiferro-chiral Crystal BPO_4 24

3.2 Inducing Chirality in BPO_4 25

3.3 Theoretical Calculations 26

3.4 Experimental Demonstration 32

3.5 Experimental Setup for Measurements on BPO_4 34

3.6 Summary 37

4 Light Control of Ferroaxial Order **40**

4.1 Ferroaxial Order 40

4.2 Axial Field Engineering 42

4.3 Static Characterisation of Ferroaxial $RbFe(MoO_4)_2$ 44

4.4 Theoretical Calculations 46
4.5 Experimental Demonstration 52
4.6 Estimation of Pump-Induced Heating 56
4.7 Experimental Setup for Measurements on $RbFe(MoO_4)_2$ 59
4.8 Summary 62

5 Conclusion and Outlook **65**

Appendices

A First-Principles Calculations of Nonlinear Phonon Couplings **69**
A.1 Computational Framework 69
A.2 BPO_4 70
A.3 $RbFe(MoO_4)_2$ 72

B Data Analysis of Measurements on BPO_4 **74**
B.1 Permittivity and Optical Activity 74
B.2 Depth Dependence and Jones Matrix Analysis 76
B.3 Time Dependence and Functional Fits 77

C Sample Preparation and Characterisation **80**
C.1 BPO_4 80
C.2 $RbFe(MoO_4)_2$ 81

References **83**

List of Figures

1.1 Spontaneous symmetry breaking. 4
1.2 Optical properties of infrared-active phonon in insulator. 6
1.3 Mechanism of nonlinear phononics. 8
1.4 Experimental demonstration of nonlinear phononics. 9
1.5 Transient x-ray diffraction in pumped $La_{0.7}Sr_{0.3}MnO_3$. 10
1.6 Light control of ferroelectricity in $LiNbO_3$. 13
1.7 Light control of magnetism in CoF_2 14

2.1 Twin-OPA and DFG scheme for THz generation. 18
2.2 Typical experimental geometry for pump–probe measurements. . . . 20
2.3 Comparison of two data acquisition schemes. 22
2.4 Detection of THz electric fields using electro-optic sampling. 23

3.1 Chirality in solid system. 25
3.2 Light-induced chirality in BPO_4. 27
3.3 Simulation of nonlinear phonon dynamics. 29
3.4 Theoretical calculations of light-induced chirality. 31
3.5 Preparation of phonon-resonant pump. 32
3.6 Time-resolved polarisation rotation in BPO_4. 35
3.7 Characterisation of the light-induced ferri-chiral states. 36
3.8 Experimental setup for measurements on BPO_4. 36
3.9 Photograph of the OPA setup. 38

4.1 Ferroaxial order. 41
4.2 Circular phonon excitation as an axial conjugate field. 43
4.3 Ferroaxial transition in $RbFe(MoO_4)_2$. 44
4.4 Probing ferroaxial order with SHG-CD. 47
4.5 Potential energy landscapes of ferroaxial order under circular phonon drive. 48
4.6 Simulation of the dynamical axial field. 50

4.7 Dynamics of the axial order above T_C. 51
4.8 Dynamics of the axial order below T_C. 52
4.9 Pump–probe setup for the light control of ferroaxial order. 53
4.10 Photo-induced axial order above T_C. 55
4.11 Switching of ferroaxial order below T_C 57
4.12 Experimental setup for measurements on $RbFe(MoO_4)_2$. 60
4.13 Design for the twin OPA system. 61
4.14 Characterisation of the THz excitation pulses. 61
4.15 Effective conjugate field for axial order. 64

A.1 Double-well potential energy of the A_{2g} ferroaxial mode in $RbFe(MoO_4)_2$. 73

B.1 Schematic of the light-induced polarisation rotation signal. 77
B.2 Parameter fitting results for the polarisation rotation signal. 78
B.3 Illustration of the birefringence contribution to the polarisation rotation signal. 79

C.1 Static optical characterisation of the $RbFe(MoO_4)_2$ sample. 82

List of Tables

3.1 Fitted E-symmetry phonons of BPO_4. 33

4.1 Effective SHG tensor for $RbFe(MoO_4)_2$ in the para-axial state. . . . 45
4.2 Effective SHG tensor for $RbFe(MoO_4)_2$ in the ferroaxial state. . . . 46
4.3 Calculated E_u phonon modes of $RbFe(MoO_4)_2$. 49

A.1 Calculated phonon parameters of BPO_4. 71
A.2 Calculated optical activity and permittivity change due to B mode displacements. 71
A.3 Calculated optical activity and permittivity change due to E mode displacements. 72
A.4 Relaxed lattice parameters of high-symmetry $RbFe(MoO_4)_2$. 72

C.1 Fitted parameters of the infrared-active E_u phonon modes of $RbFe(MoO_4)_2$. 82

List of Abbreviations

DFG . . . . . Difference-frequency generation.

DFT . . . . . Density functional theory.

EQ . . . . . Electric quadrupole.

FWHM . . . . Full width at half maximum.

IR . . . . . Infrared.

LO . . . . . Longitudinal optical (phonon mode).

MIR . . . . . Mid-infrared.

OPA . . . . . Optical parametric amplifier.

RA-SHG . . . Rotational anisotropy second-harmonic generation.

SHG . . . . . Second-harmonic generation.

SHG-CD . . . Second-harmonic generation circular dichroism.

THz . . . . . Terahertz.

Ti:Sa . . . . . Titanium:sapphire (laser).

TO . . . . . Transverse optical (phonon mode).

Πάντες ἄνθρωποι τοῦ εἰδέναι ὀρέγονται φύσει. Διὰ γὰρ τὸ θαυμάζειν οἱ ἄνθρωποι καὶ νῦν καὶ τὸ πρῶτον ἤρξαντο φιλοσοφεῖν.

All men by nature desire to know. For it is through wonder that men both now and at first began to philosophize.

— Aristotle, *Metaphysics*

1 Introduction

Contents

1.1 Symmetry Breaking and Emerging Orders in Solids . 1
1.2 Nonlinear Lattice Control 4
1.3 Development of Nonlinear Lattice Control 8

1.1 Symmetry Breaking and Emerging Orders in Solids

Symmetry and its spontaneous breaking form the fundamental basis of condensed matter physics and underpin many of the emergent phenomena observed in complex materials [1]. A wide range of technologically relevant and conceptually rich phases of matter—such as ferromagnetism, ferroelectricity, and superconductivity—emerge as a result of spontaneous symmetry breaking. These symmetry-breaking phases are not only central to the classification of states of matter, but also underpin a wide range of functional properties in solids, from switchable polarisation and magnetization to dissipationless transport and nontrivial topological responses.

The profound link between broken symmetry and emergent macroscopic behaviour was elegantly captured by Pierre Curie, who remarked that "it is the dissymmetry that creates the phenomenon" [2]. In many cases, the emergence of new macroscopic behaviour arises directly from the symmetry that is lost at the transition. For example, ferromagnetism emerges from the spontaneous breaking of time-reversal symmetry, while ferroelectricity results from the loss of spatial inversion symmetry. Superconductivity, nematicity, and various charge- and spin-ordered states are all manifestations of ordered phases that emerge from symmetry-breaking transitions [3–5]. These concepts are illustrated in Figure 1.1, which shows how ordered states such as crystalline solids, ferroelectrics, and ferromagnets arise from high-symmetry phases through spontaneous symmetry breaking, with accompanying order parameters that quantify the emergent order.

A foundational conceptual framework for understanding these phenomena was developed by Lev Landau, who introduced the notion of an order parameter—a quantity that characterises the degree and nature of order in a system [6]. Landau's theory not only provides a phenomenological description of phase transitions and connects symmetry properties to the form of the free-energy landscape, but also offers insights into critical behaviour near phase transitions, such as scaling laws and the interplay between fluctuations and external fields. In this view, material functionality can be rationalized by the form of the free-energy surface and by the couplings between relevant order parameters and external controls.

Controlling such broken-symmetry phases is a longstanding goal in condensed matter research, with implications spanning from fundamental physics to device

applications. Traditional routes rely on chemical substitution [7], strain engineering [8], and interfacial engineering [9, 10]. In recent years, advances in ultrafast and nonlinear optics have opened a new frontier: the ability to dynamically manipulate symmetry and induce or suppress order using light [11]. This capability highlights the possibility of accessing phases that are unstable or hidden in equilibrium, and of tailoring emergent orders on demand, potentially on sub-picosecond timescales and far from thermal equilibrium.

In particular, resonant lattice excitation has recently emerged as a powerful approach, enabling selective control of collective modes through the coherent driving of infrared-active phonons [12]. This technique has been successfully employed to enhance superconductivity, switch ferroelectric polarisation, and control magnetic and orbital orders in complex materials [13–15].

Motivated by these recent developments, this thesis aims to explore new pathways for controlling symmetry and order in solids via resonant lattice excitation [16]. By selectively driving infrared-active phonon modes and exploiting nonlinear phonon–phonon interactions, it becomes possible to dynamically lower crystal symmetries and control material functionalities in a mode- and symmetry-selective manner. Two representative examples will be studied: the light-induced emergence of chirality in the non-chiral crystal BPO_4, and the optical switching of ferroaxial order in the oxide $RbFe(MoO_4)_2$. These case studies highlight how light can be used to reshape the energy landscape of a solid and steer the system into symmetry-broken phases with desirable properties, providing a blueprint for dynamic materials design.

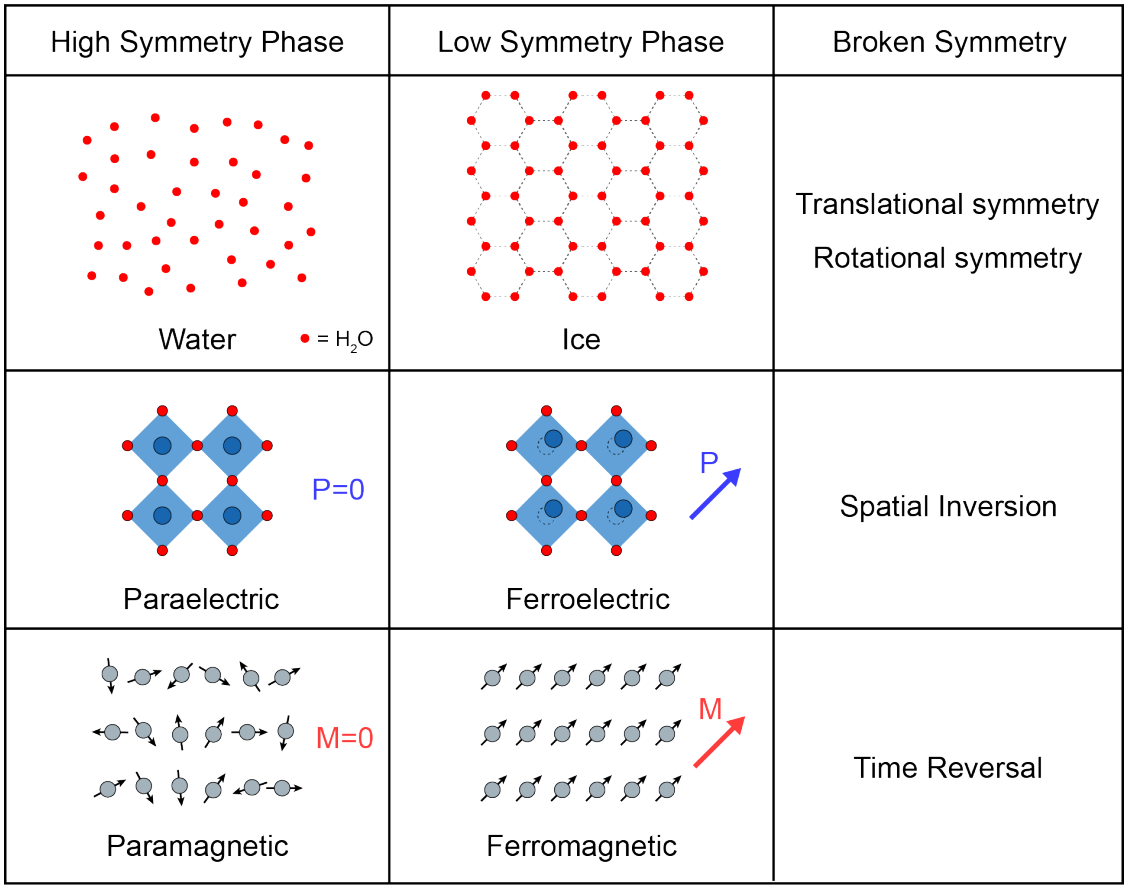

Figure 1.1: Spontaneous symmetry breaking. Top panel: Structural transition from water to ice: at high temperature, water molecules are disordered. Upon freezing, a crystal lattice forms, breaking translational and rotational symmetry. Middle panel: In a paraelectric phase, the structure is centrosymmetric. Inversion symmetry is broken, and a spontaneous polarisation P emerges in the ferroelectric phase. Bottom panel: In the paramagnetic phase, spin orientations are random. In the ferromagnetic phase, the spins align, breaking time-reversal and giving rise to a net magnetization M.

1.2 Nonlinear Lattice Control

Light interacts with various elementary excitations in solids—such as electronic transitions, plasmons, magnons, and phonons—depending largely on the frequency of the incident radiation [17]. In the terahertz (THz) range, light can resonantly couple to infrared (IR)-active phonons, which correspond to lattice vibrations involving dipole-active atomic displacements and typically lie in the meV energy range. Because these energies are well below typical electronic gaps, THz excitation

can manipulate the lattice while largely avoiding electronic heating, providing a highly selective means of controlling structural degrees of freedom.

Figure 1.2a illustrates the typical optical response of an IR-active phonon in an insulating crystal. Near the transverse optical (TO) frequency, the real part of the dielectric function shows strong dispersion, while the imaginary part peaks, reflecting resonant absorption. As the frequency increases further, the real part of the dielectric function crosses zero at the longitudinal optical (LO) frequency. A corresponding behaviour is observed in the optical constants: between the TO and LO frequencies, the real part of the refractive index drops toward zero while the imaginary part remains large and positive—indicative of strong attenuation of electromagnetic waves. As a result, the reflectivity spectrum reveals a region of near-unity reflection between TO and LO, known as the Reststrahlenband [18].

Figure 1.2b depicts the dispersion relation of the resulting phonon polaritons, a hybrid light–matter quasiparticles formed through strong coupling between the IR-active phonon and the electromagnetic field [19].

A promising strategy for ultrafast control of material properties involves the coherent excitation of selected phonon modes to large amplitudes. This forms the basis of nonlinear phononics, where driving a specific phonon mode strongly can induce targeted structural distortions through anharmonic coupling to other lattice degrees of freedom and, crucially, along symmetry-allowed pathways.

A key advantage of this approach is its ability to selectively and efficiently target specific lattice vibrations by resonantly exciting the IR-active phonon modes with low-energy meV photons. Since these photon energies lie well below the electronic band gap in many materials, nonlinear phononics enables precise structural

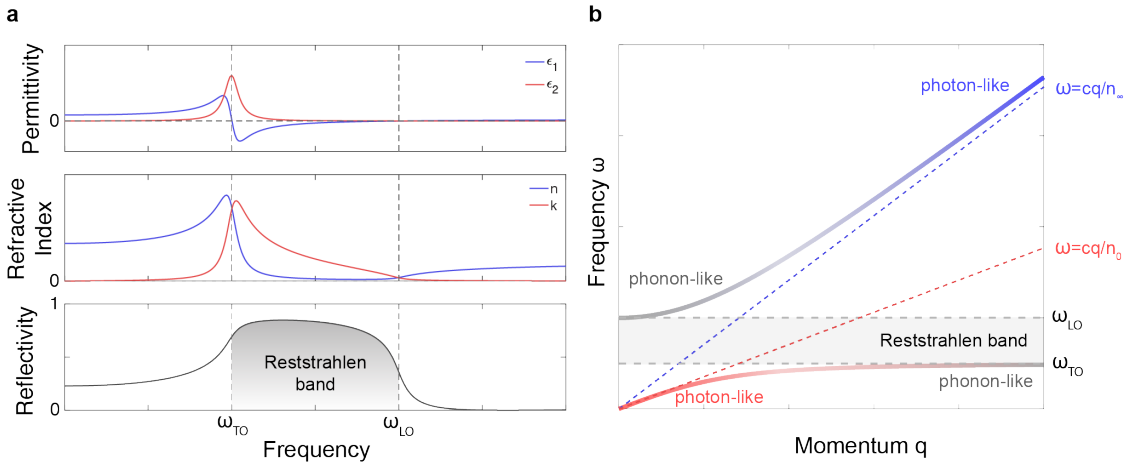

Figure 1.2: Optical properties of an infrared-active phonon in an insulator. a) Top: Real (blue) and imaginary (red) parts of the dielectric function. Middle: Real (blue) and imaginary (red) parts of the refractive index. Bottom: Reflectivity spectrum showing the Reststrahlenband between transverse optical (TO) and longitudinal optical (LO) phonon frequencies. b) Dispersion relation of a phonon polariton. The coupling of light with the infrared-active phonon gives rise to hybrid light–matter excitations known as phonon polaritons.

manipulation without direct electronic excitation or significant heating. This makes it highly selective for dynamically controlling symmetry and functionality on ultrafast timescales, while suppressing unwanted heating and avoiding the irreversible energy deposition and damage that typically occur under electronic pumping.

To illustrate this mechanism (Fig. 1.3a), consider a phonon mode Q_1 that is directly driven by an external electric field. Its harmonic potential is given by

$$U_{\text{harm}} = \tfrac{1}{2}\omega_1^2 Q_1^2, \tag{1.1}$$

where Q_1 is the phonon coordinate and ω_1 is the natural frequency of the mode. When subjected to a resonant electric field pulse, this mode can be coherently driven to large displacements. The corresponding equation of motion takes the form

$$\frac{\partial^2 Q_1}{\partial t^2} + \gamma_1 \frac{\partial Q_1}{\partial t} + \omega_1^2 Q_1 = Z^* E(t), \tag{1.2}$$

where γ_1 is a phenomenological damping constant, Z^* is the mode-effective charge reflecting the coupling strength to the electric field, and $E(t)$ is the time-dependent electric field of the pulse.

This analysis assumes that both the driving light field and the lattice vibrations can be treated classically. The light field is considered coherent, allowing quantum effects of the electromagnetic field to be neglected, and the phonon coordinate Q_1 is described as a classical real variable, such that the non-commutativity of atomic position and momentum operators is ignored.

While the time averaged of Q_1 remains zero after excitation, its large-amplitude oscillations can strongly influence other phonon modes through nonlinear interactions. A particularly important case involves cubic anharmonic coupling between Q_1 and a second mode Q_2, represented by the interaction term

$$U_{\mathrm{NL}} = \alpha Q_1^2 Q_2, \tag{1.3}$$

which is allowed by symmetry when this coupling term remains invariant under all the symmetry operations of the system. This nonlinear interaction modifies the effective potential for Q_2, introducing a rectified driving force proportional to Q_1^2 that displaces Q_2 from its equilibrium position (Fig. 1.3b). The resulting dynamics of Q_2 can be described by

$$\frac{\partial^2 Q_2}{\partial t^2} + \gamma_2 \frac{\partial Q_2}{\partial t} + \omega_2^2 Q_2 = -\alpha Q_1^2, \tag{1.4}$$

where γ_2 and ω_2 are the damping and natural frequency of the secondary mode, respectively.

This rectification mechanism enables the generation of a quasi-static lattice distortions using ultrafast pulses (Fig. 1.3c). The induced displacement of Q_2

can directly couple to functional degrees of freedom—such as electric polarisation, magnetic ordering, or orbital occupancy—offering a versatile route for dynamically tailoring the properties of quantum materials. In practice, field strengths of a few MV/cm and pulse durations of a few hundred femtoseconds are sufficient to reach the nonlinear regime, while maintaining crystalline integrity and reversibility of the induced changes.

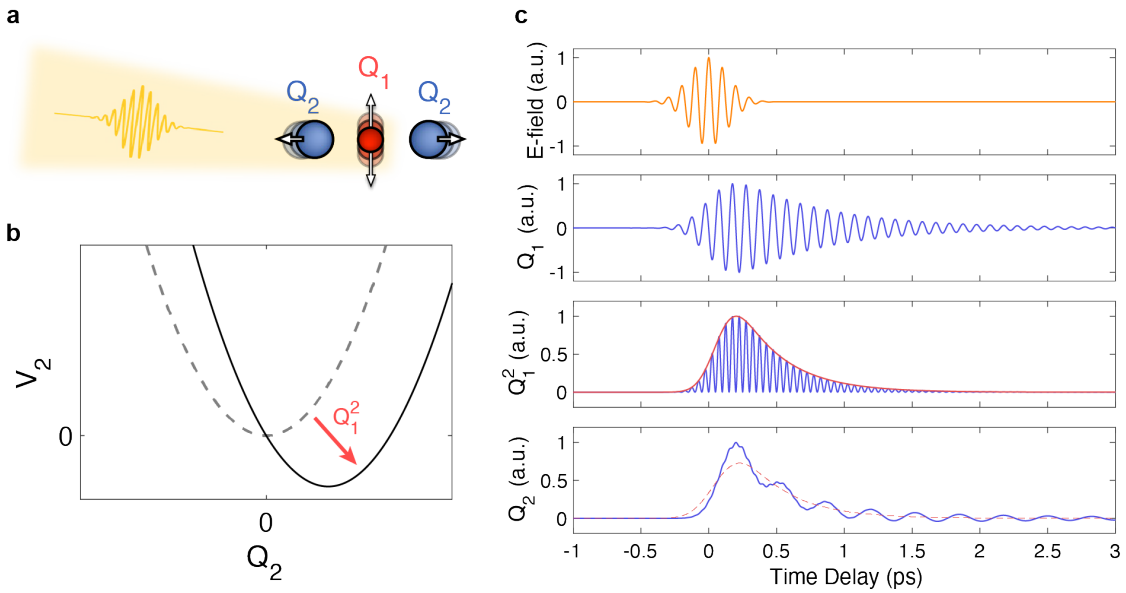

Figure 1.3: Mechanism of nonlinear phononics. (a) A short light pulse resonantly excites the infrared-active mode Q_1, which anharmonically couples to a second mode Q_2. (b) The equilibrium potential of the Raman mode Q_2 is shifted through the nonlinear coupling term $Q_1^2 Q_2$. (c) Dynamics of the process. Top panel: Electric field of the excitation pulse. Second panel: Oscillatory response of the infrared-active mode Q_1. Third panel: Rectified force acting on the Q_2 mode, proportional to Q_1^2. Bottom panel: Dynamics of the Q_2 mode.

1.3 Development of Nonlinear Lattice Control

To date, the first experimental realisation of nonlinear phononics was demonstrated in $La_{0.7}Sr_{0.3}MnO_3$ [20]. In this study, resonant excitation of an infrared-active phonon at 605 cm^{-1} (18.2 THz) coherently drove a Raman-active mode of E_g

symmetry at 40 cm^{-1} (1.2 THz) through anharmonic coupling. The corresponding results are presented in Fig. 1.4. The response differs significantly from that obtained under near-IR excitation at a central wavelength of 1.5 μm, which instead induces coherent oscillations of a totally symmetric A_{1g} mode at 193 cm^{-1} (5.8 THz), highlighting the selectivity of resonant lattice driving.

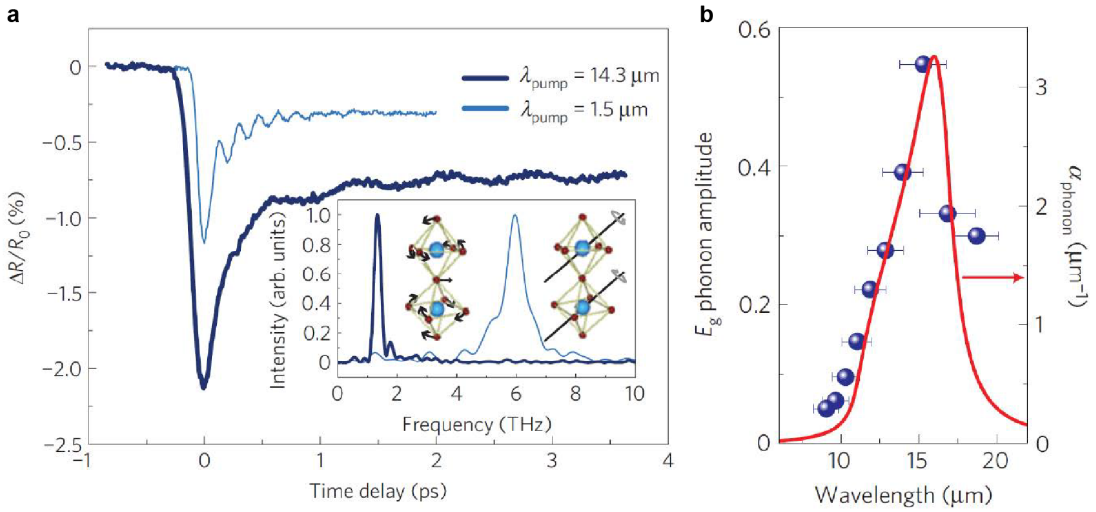

Figure 1.4: Experimental demonstration of nonlinear phononics. (a) Time-resolved reflectivity changes of $La_{0.7}Sr_{0.3}MnO_3$ measured at 800 nm following mid-IR excitation at 14.3 μm and near-IR excitation at 1.5 μm. The inset shows the Fourier transform of the oscillatory signal and the atomic displacements of the corresponding modes. (b) Resonant enhancement of the coherent E_g phonon amplitude. Results were corrected for wavelength-dependent changes in reflectivity. Horizontal bars denote the bandwidths of the mid-IR pump pulses. The red curve shows the linear absorption due to the infrared-active E_u phonon. Adapted from [20].

Subsequent studies employing THz-pump and x-ray-probe techniques provided direct structural evidence supporting the third-order anharmonic mechanism [21]. As shown in Fig. 1.5, the time-dependent changes in the intensity of two Bragg reflections reveal transient, step-like responses of opposite sign following resonant excitation of the transverse optical (TO) mode at 605 cm^{-1} (18.2 THz). For a THz fluence of 1.2 mJ/cm^2, the observed displacements correspond to a 0.09 pm

distortion of the E_g mode, equivalent to a rotation of the oxygen octahedra by 0.035°, consistent with a rectified force proportional to the square of the driven coordinate.

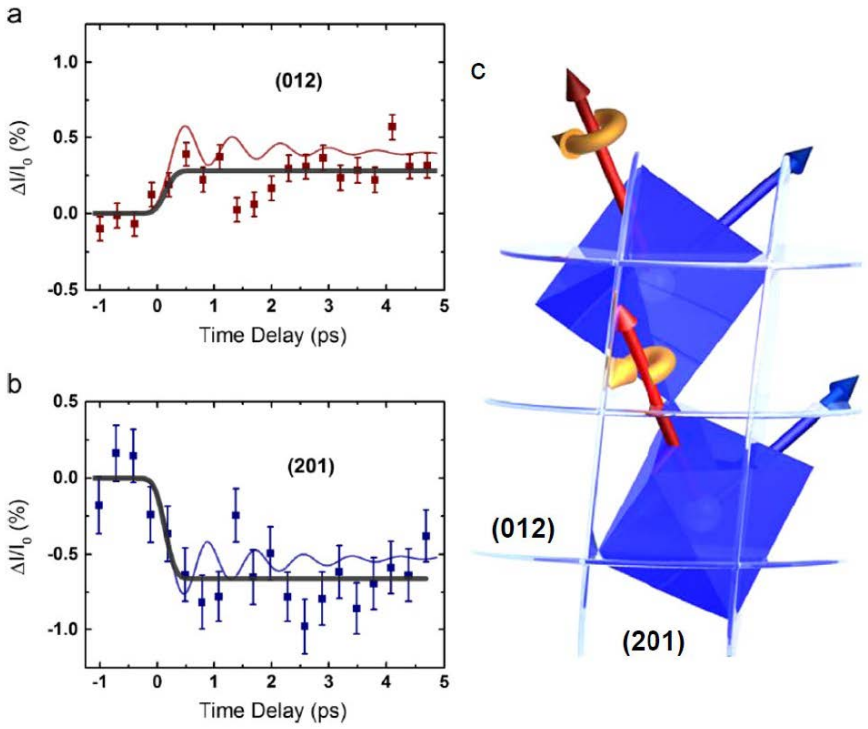

Figure 1.5: Transient x-ray diffraction in pumped $La_{0.7}Sr_{0.3}MnO_3$. Time-resolved changes in the scattered intensity from the (a) (012) and (b) (201) lattice reflections of $La_{0.7}Sr_{0.3}MnO_3$ following resonant excitation of the Mn–O stretching vibration. Red and blue curves show the results of model calculations. (c) Schematic of the nonlinearly driven Raman-active E_g mode, corresponding to a rotation of the oxygen octahedra (red arrow) around an axis perpendicular to the rhombohedral [111] direction (blue arrow). Adapted from [21].

These experiments established that anharmonic coupling between infrared and Raman phonons can induce a transient, dynamical deformation of the lattice structure. Since then, substantial progress has been made along the following two main directions.

In the first direction, extensive experimental and theoretical efforts have elucidated the microscopic mechanisms of nonlinear phononics across systems with diverse symmetries and coupling pathways. Such studies have demonstrated, for example,

symmetry breaking through the simultaneous excitation of multiple modes [22, 23], enhanced energy transfer via sum-frequency resonances [24–26], and the importance of higher-order nonlinearities [27], which enable phonon amplification [28] and interatomic potential mapping in complex solids [29, 30]. These findings have refined our understanding of the relationship between symmetry-based selection rules, anharmonic interactions, and the experimentally achievable routes for lattice control.

In the second direction, nonlinear phononics has emerged as a powerful approach for deterministically and strongly modifying crystal structures and their associated functional macroscopic properties with light [31]. Because the formation of long-range ordered phases is inherently tied to the breaking of specific crystallographic or time-reversal symmetries, such phases can be driven or stabilized through light-induced lattice control. This strategy has been successfully employed to manipulate ferroelectricity in $LiNbO_3$ [14, 32] and magnetism in CoF_2 [15], and more broadly opens pathways for the on-demand control of ferroic and multipolar orders in correlated and topological materials.

The atomic motions of the ferroelectric mode in $LiNbO_3$ are illustrated in Fig. 1.6(a). The equilibrium potential energy surface of the ferroelectric mode exhibits a double-well structure along the coordinate Q_P, where the equilibrium value of Q_P resides in one of the minima (Fig. 1.6(b)). Considering the nonlinear coupling between the driven infrared (IR)-active mode and the ferroelectric mode, the total lattice potential can be expressed as [14, 33]

$$V(Q_P, Q_{\mathrm{IR}}) = -\frac{1}{2}\omega_P^2 Q_P^2 + \frac{1}{4}c_P Q_P^4 + \frac{1}{2}\omega_{\mathrm{IR}}^2 Q_{\mathrm{IR}}^2 - \frac{1}{2}a Q_{\mathrm{IR}}^2 Q_P^2, \tag{1.5}$$

where ω_P and ω_{IR} denote the frequencies of the ferroelectric and high-frequency IR-active modes at 19 THz, respectively, c_P is the quartic anharmonic coefficient, and a characterises the coupling strength.

For finite displacements Q_{IR}, the minimum of the potential is shifted to a lower value and the double-well potential further becomes a single-well potential when Q_{IR} exceeds a threshold value, as shown schematically in Fig. 1.6(b). Notably, although the model above includes only the quadratic term Q_{IR}^2 for the driven phonon mode, higher-order contributions (e.g., Q_{IR}^4) should also be considered when the IR phonon coordinate is driven to large amplitudes (see Ref. [29]).

The corresponding dynamics of the two coupled modes are governed by the equations of motion

$$\ddot{Q}_{\mathrm{IR}} + \gamma_{\mathrm{IR}}\dot{Q}_{\mathrm{IR}} + \omega_{\mathrm{IR}}^2 Q_{\mathrm{IR}} = aQ_P^2 Q_{\mathrm{IR}} + Z^* f(t), \tag{1.6}$$

$$\ddot{Q}_P + \gamma_P \dot{Q}_P - \omega_P^2 Q_P + c_P Q_P^3 = aQ_P Q_{\mathrm{IR}}^2, \tag{1.7}$$

where γ_{IR} and γ_P are damping constants, Z^* is the mode-effective charge, and $f(t)$ represents the driving electric field.

Experimentally, time-resolved, phase-sensitive second-harmonic (SH) generation measurements were performed following resonant excitation at 19 THz. The time-dependent SH intensity for selected pump fluences F is shown in Fig. 1.6(c). For $F < 50$ mJ/cm^2, the SH intensity decreases to a finite value within approximately 200 fs. In contrast, for $F \approx 95$ mJ/cm^2, the SH intensity vanishes completely twice near an intermediate value before relaxing back to equilibrium.

The time-dependent interference of the SH field was further analysed by overlapping the pump-induced SH pulse with a reference pulse generated in an unexcited

crystal on a CCD camera. After excitation, the SH intensity initially decreased at a constant phase. At zero time delay, the phase of the SH field flipped by 180°, as evidenced by the sudden sign reversal of the interference fringes. This observation indicates a transient reversal of the ferroelectric polarisation and demonstrates coherent, field-driven switching of the order parameter.

Such vibrational control of polarisation reversal on a sub-picosecond timescale demonstrates the potential of nonlinear phononics for ultrafast control of functional properties in solids. Moreover, this mechanism offers a promising route toward nonvolatile, ultrafast ferroelectric memory devices, and more generally toward reconfigurable quantum materials platforms.

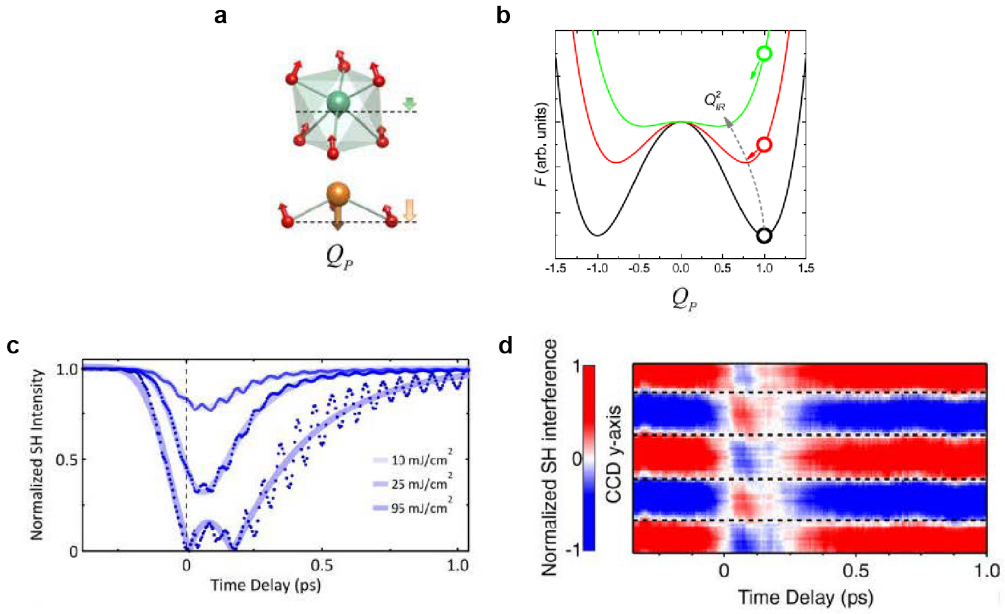

Figure 1.6: Light control of ferroelectricity in $LiNbO_3$. (a) Left: atomic motion of the ferroelectric mode Q_P and the double-well potential $V(Q_P, Q_{\mathrm{IR}})$ along the mode coordinate. (b) Solutions to the coupled equations of motion below and above the excitation threshold. (c) Time-resolved second-harmonic (SH) intensity normalized to its pre-excitation value. (d) Time-resolved measurement of the interference fringes (integrated along the x-direction on the CCD) showing a transient π phase shift following THz excitation. Adapted from [14] and [33].

In the case of CoF_2, the simultaneous excitation of two degenerate infrared-active

modes anharmonically drives a lattice distortion along the B_{2g} Raman coordinate (Fig. 1.7a). This distortion modifies the crystal field environment around the two Co ions, which carry opposite magnetic moments at equilibrium. Because the modulation of the crystal field acts differently on the two sites, the orbital contributions to their local magnetic moments become unequal, thereby inducing a net magnetization. Consequently, this mechanism enables all-optical control of the antiferromagnetic order, driving the material into a ferrimagnetic state with an induced moment far exceeding that achievable by static strain (Fig. 1.7b).

The experimental results on $LiNbO_3$ and CoF_2 underscore the generality of nonlinear lattice control as a pathway to create light-induced phases through symmetry-selective vibrational driving.

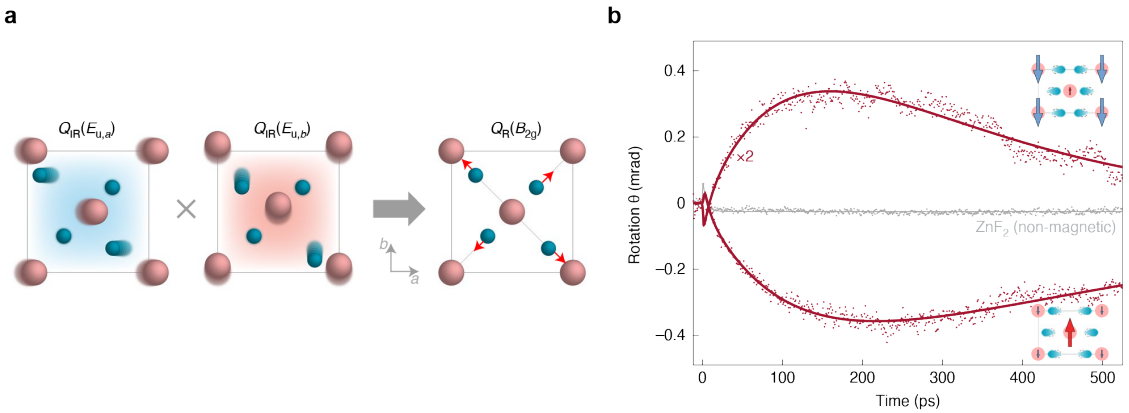

Figure 1.7: Light control of magnetism in CoF_2. (a) Two orthogonal, degenerate E_u phonons mix nonlinearly to displace the lattice along the B_{2g} Raman mode coordinate. The resulting lattice force (F_{Q_R}) is indicated by red arrows. (b) Faraday rotation data for CoF_2 (red) under pump polarisations of $+45°$ and $-45°$ as a function of time delay. Both traces exhibit a similar temporal evolution, with an initial signal that reverses, saturates, and gradually returns to zero. The inset depicts the induced structural distortion (in the a–c plane) and the resulting ferrimagnetic state for the two pump polarisations. For comparison, measurements on ZnF_2 (grey) show no long-lived response. Adapted from [15].

What we observe is not nature itself, but nature exposed to our method of questioning.

— Werner Heisenberg, *Physics and Philosophy: The Revolution in Modern Science* (1958)

2 Experimental Techniques

Contents

2.1 Tabletop Strong Field THz Generation 15
2.2 Time-resolved Measurements 17
2.3 Data Acquisition 20
2.4 Electro-optic Sampling 22

2.1 Tabletop Strong Field THz Generation

Intense terahertz (THz) light sources are powerful tools for exploring and manipulating the nonlinear response of materials. By delivering strong electric fields, THz pulses can drive low-energy excitations such as lattice vibrations, spin waves, or charge density fluctuations into the nonlinear regime—revealing phenomena that are otherwise inaccessible in equilibrium [34].

Depending on the specific experimental demands, strong THz fields can be generated either at large-scale facilities such as free-electron lasers (FEL) [35], or using compact tabletop laser systems that rely on frequency mixing in nonlinear

optical crystals [36]. The latter approach offers greater flexibility and accessibility and has become an emerging technique in ultrafast condensed matter research, particularly when high field strengths and waveform stability are required in a laboratory setting.

This section focuses on THz generation using tabletop sources, where field strengths exceeding 100 MV/cm can be achieved via difference frequency generation (DFG) in second-order nonlinear optical crystals [34]. To produce the tunable near-infrared (NIR) input pulses required for DFG, the system typically employs optical parametric amplification (OPA)—a nonlinear process that efficiently down-converts a high-intensity pump beam into two lower-frequency components while preserving phase coherence throughout the process.

Optical parametric amplification (OPA) [37] takes place in a nonlinear crystal that possesses a second-order nonlinear susceptibility $\chi^{(2)}$. In this process, a strong optical field at frequency ω_p (the pump) interacts with a weaker field at frequency ω_s (the signal) inside the crystal. The nonlinear interaction enables the transfer of energy from the pump to the signal, mediated by the $\chi^{(2)}$ response of the material. To satisfy energy conservation, a third field at frequency ω_i (the idler) is generated simultaneously (Fig. 2.1a). The frequencies of these three waves are related by

$$\omega_p = \omega_s + \omega_i, \tag{2.1}$$

The coupled-wave equations governing OPA can be written as

$$\frac{dE_{\omega_s}}{dx} = \frac{2i\chi^{(2)}\omega_s^2}{c^2 k_{\omega_s}} E_{\omega_p} E^*_{\omega_i} e^{i\Delta k x}, \tag{2.2}$$

$$\frac{dE_{\omega_i}}{dx} = \frac{2i\chi^{(2)}\omega_i^2}{c^2 k_{\omega_i}} E_{\omega_p} E^*_{\omega_s} e^{i\Delta k x}, \tag{2.3}$$

with $\Delta k = k_p - k_s - k_i$. Efficient amplification requires $|\Delta k| \lesssim \pi/L$, where L is the crystal length; the associated *coherence length* $L_c = \pi/|\Delta k|$ sets the scale over which energy transfer remains constructive.

Like OPA, difference frequency generation (DFG) involves the coherent interaction of three optical fields. In DFG, two input beams (often of comparable strength and tunable frequency) mix in a $\chi^{(2)}$ crystal to produce an idler at the difference frequency, which can lie in the THz or mid-infrared (MIR) range (Fig. 2.1c). Assuming perfect phase matching and negligible pump depletion, the idler field amplitude evolves as

$$E_{\omega_i}(z) = i \, \frac{E_{\omega_p} E^*_{\omega_s}}{|E_{\omega_p} E^*_{\omega_s}|} \left(\frac{n_{\omega_s} \omega_i}{n_{\omega_i} \omega_s} \right)^{1/2} \sinh(\kappa_i z), \tag{2.4}$$

where $\kappa_i \propto d_{\text{eff}} \sqrt{I_{\omega_p} I_{\omega_s}}$ is the parametric gain coefficient, d_{eff} is the effective nonlinear coefficient, n_ω are refractive indices, and I_ω the input intensities. This expression highlights the exponential growth under phase-matched conditions.

Realising strong THz output requires engineering both dispersion and nonlinearity. Common crystals include GaSe and $AgGaS_2$ for MIR–THz, $LiNbO_3$ with pulse-front tilting for sub-THz to few-THz, GaP and ZnTe for multi-THz DFG.

Importantly, the carrier-envelope phase (CEP) of the generated THz (idler) field is determined by the difference in CEPs between the pump and signal inputs [38]. Stabilizing their relative phase yields CEP-stable THz pulses [36, 39]—crucial for coherent control, lightwave electronics, and nonlinear phononics.

2.2 Time-resolved Measurements

Pump–probe spectroscopy is a well-established and versatile technique for investigating the ultrafast dynamics of materials driven out of equilibrium by exter-

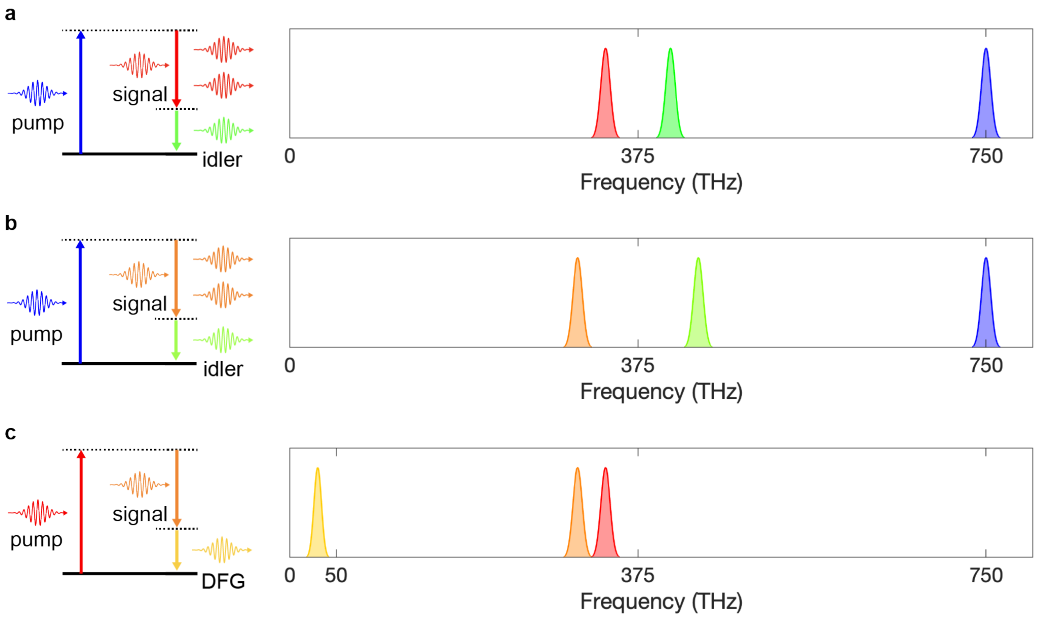

Figure 2.1: Twin-OPA and DFG scheme for THz generation. (a) First OPA branch: A laser pulse from a Ti:sapphire amplifier system (centreed at ∼750 THz) is down-converted into two pulses, referred to as signal and idler. (b) Second OPA branch: The same laser pulse is used to generate another pair of pulses with different frequencies. (c) A THz pulse is generated via difference frequency generation (DFG) between the signal pulses from the first and second OPA branches.

nal stimuli [40]. It enables time-resolved access to the evolution of physical properties—such as optical absorption, reflectivity, polarisation, or structural symmetry—following excitation by an ultrashort laser pulse. Beyond tracking response functions, pump–probe methods provide a route to disentangle coupled degrees of freedom by tuning pump frequency, polarisation, and fluence, and by selecting probe observables with specific symmetry or elemental sensitivity.

In a typical setup, a femtosecond laser pulse is split into two: the pump pulse, which excites the sample and drives it into a non-equilibrium state, and the probe pulse, which interrogates a specific material property at a controlled delay time. By precisely varying the relative arrival time of the pump and probe pulses at the sample, one can construct a temporal map of the material's response to excitation, revealing dynamical processes such as carrier relaxation, coherent

phonon oscillations, phase transitions, or symmetry breaking (Fig. 2.2). The overall temporal resolution is determined by the convolution of pump and probe pulse durations and by timing jitter.

The spectral range of pump–probe techniques spans several orders of magnitude, enabling access to a wide variety of physical phenomena. Pump pulses are typically delivered in the terahertz, mid-infrared, or optical regimes, where they can resonantly drive low-energy excitations such as lattice vibrations, charge density waves, or electronic transitions. Probing, on the other hand, can be performed across a broad spectral range—from THz to visible light and up to soft and hard x-rays. In particular, x-ray probes—often generated at free-electron laser (FEL) or synchrotron facilities—provide element-specific and atomic-scale sensitivity, allowing direct observation of structural and electronic changes with femtosecond resolution. Combining optical and x-ray probes allows direct correlation between the dynamics of order parameters and the evolution of the underlying lattice structure.

Laboratory-based ultrafast laser systems used in pump–probe experiments typically operate in one of following two regimes. Oscillator-based systems run at high repetition rates (tens to hundreds of MHz) and deliver low pulse energies, typically < 10 nJ, ideal for high-throughput, low-excitation measurements. In contrast, amplifier-based systems operate at lower repetition rates (usually 1–10 kHz) but deliver much higher pulse energies, often hundreds of μJ to several mJ per pulse. This high-energy, low-repetition-rate configuration is especially well-suited for driving nonlinear processes or resonant excitations in solids, such as coherent phonon generation or structural phase transitions.

In the experiments described in this thesis, high-energy femtosecond laser systems operating at a 1 kHz repetition rate were employed to generate resonant excitations of vibrational modes in crystalline materials. The corresponding excitation energies, ranging from 10 to 100 meV, were produced via a difference-frequency generation (DFG) process following optical parametric amplification (OPA), both pumped by a Ti:sapphire amplifier system.

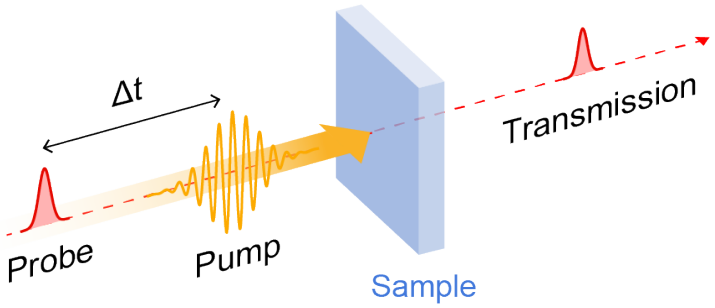

Figure 2.2: Typical experimental geometry for pump–probe measurements. The pump pulse excites the sample, while the probe pulse measures the induced changes as a function of delay time.

2.3 Data Acquisition

Most of the pump-probe measurements are carried out in a stroboscopic fashion, where the sample is excited repetitively by identical pump pulses, and the system's transient response is probed at controlled delay times after excitation. Each pump–probe cycle is assumed to reproduce the same dynamical evolution, as the system fully relaxes back to equilibrium before the arrival of the next pulse. By scanning the delay between pump and probe over many such identical cycles, the time evolution of the material's response is reconstructed from an ensemble-averaged signal.

To enhance the signal-to-noise ratio in pump–probe experiments, it is common practice to modulate the pump pulses—typically by chopping them at a fixed frequency—and to synchronize the detection of the probe signal with this modulation. For pulsed laser systems, the chopping frequency is often chosen to be a rational submultiple of the laser repetition rate. This ensures that the probe pulses can be consistently correlated with either the presence or absence of the pump pulse, enabling differential measurements that isolate the pump-induced signal while suppressing slow drifts noise, such as such as laser intensity variations or detector instabilities.

Two prevalent data acquisition approaches in such setups are lock-in amplification and boxcar integration.

Lock-in amplification is effective when the signal of interest is periodic and narrowband (Fig. 2.3a). The reference is provided by the chopper, and demodulation at its fundamental (or higher harmonic) yields excellent rejection of out-of-band noise. The technique performs best when the response is spectrally concentrated around the modulation frequency. If the response is much shorter than the modulation period, only a small portion contributes to the demodulated output, reducing detection efficiency. The integration time constant sets the trade-off between noise suppression and acquisition speed.

Boxcar integration is better suited for capturing transient signals with a defined temporal profile (Fig. 2.3b). It operates by integrating the signal over a narrow time window synchronized with the probe pulse. This method is advantageous when the response is temporally localized or confined to a specific delay time. Performance

depends on the accuracy of the gate timing and the electronic bandwidth of the integrator; timing jitter broadens the effective gate and degrades amplitude fidelity.

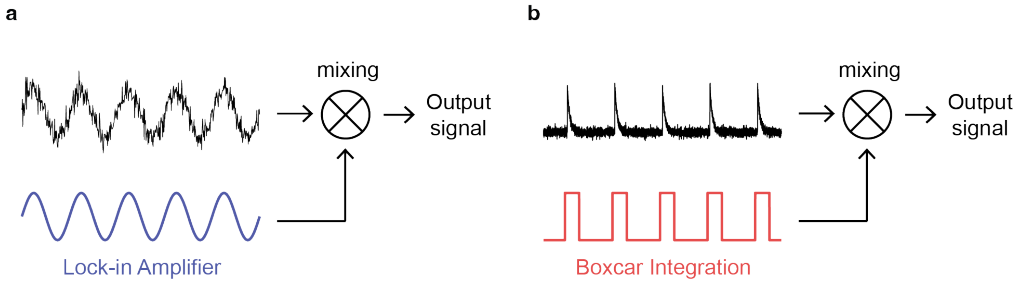

Figure 2.3: Comparison of two data acquisition schemes used in pump–probe experiments. (a) Lock-in amplification is well suited for periodic, sine-wave-like signals. (b) Boxcar integration is more effective for transient, pulsed signals.

2.4 Electro-optic Sampling

The spectral and temporal profile of ultrashort THz pulses can be characterised by electro-optic sampling (EOS) [41], a widely used and powerful technique for THz pulse measurement. EOS directly measures the electric field waveform rather than intensity, enabling retrieval of both amplitude and phase of the THz transient.

In a typical EOS setup, the THz beam is focused into a detection crystal possessing a second-order susceptibility $\chi^{(2)}$. Common detection crystals include GaSe, GaP, and ZnTe[42]. A linearly polarised gate pulse, with duration shorter than the THz cycle to be resolved, is spatially and temporally overlapped with the THz beam inside the crystal. The THz electric field induces a transient birefringence via the Pockels effect, described by $\Delta n_{ij} \propto r_{ijk} E_k^{\mathrm{THz}}$, where r_{ijk} is the electro-optic tensor. This birefringence modulates the polarisation state of the gate pulse and introduces ellipticity proportional to the instantaneous THz field.

After exiting the detection crystal, the ellipticity of the gate pulse is analysed using a quarter-wave plate, a Wollaston prism, and balanced photodetectors

(Fig. 2.4a). In some implementations, detection efficiency is enhanced by phase matching the group velocity of the gate pulse and the phase velocity of the THz pulse [43, 44]. The usable detection bandwidth is usually limited by the crystal phonon resonances (which increase absorption and dispersion), by velocity mismatch, and by the gate pulse duration.

To reconstruct the full temporal waveform, the relative delay between the gate and THz pulse is scanned. Measuring the induced ellipticity versus delay yields the electric field $E_{\mathrm{THz}}(t)$ point by point. A typical multi-THz waveform obtained via EOS is shown in Fig. 2.4b. For absolute field calibration, one may reference the EOS signal to a known electro-optic coefficient and crystal thickness, or cross-calibrate with a pyroelectric detector using energy and spot-size measurements. Polarisation-resolved EOS (rotating the crystal or gate polarisation) allows vectorial field reconstruction [45–48].

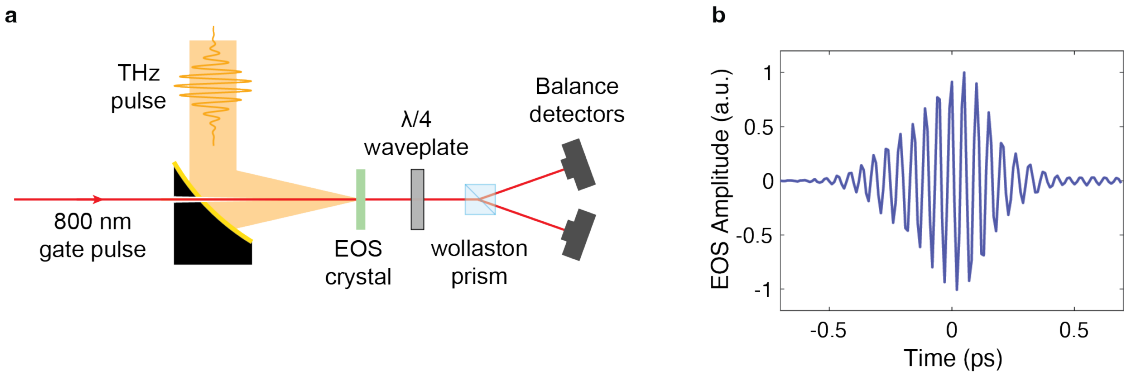

Figure 2.4: Detection of THz electric fields using electro-optic sampling. (a) The THz pulse (yellow) is focused into an electro-optic sampling crystal and overlapped with a short gate pulse (red). The induced ellipticity of the gate pulse is analysed using a quarter-wave plate, a Wollaston prism, and balanced photodiodes. (b) Example EOS waveform for a 19 THz pulse measured using a GaSe crystal.

To see a World in a Grain of Sand, And a Heaven in a Wild Flower, Hold Infinity in the palm of your hand, And Eternity in an hour.

— William Blake, *Auguries of Innocence*

3 Light-induced Chirality

Contents

3.1 Antiferro-chiral Crystal BPO_4 24
3.2 Inducing Chirality in BPO_4 25
3.3 Theoretical Calculations 26
3.4 Experimental Demonstration 32
3.5 Experimental Setup for Measurements on BPO_4 . . . 34
3.6 Summary 37

3.1 Antiferro-chiral Crystal BPO_4

An object is chiral if its mirror image cannot be superimposed to itself by any combination of rotations or translations. Crystals are thus classified as chiral or non-chiral. NaCl crystallizes in the non-chiral rocksalt structure [49] (Fig. 3.1a). In contrast, α-quartz [50] is chiral with two enantiomorphs (space groups $P3_121$ and $P3_221$), distinguished by atomic spirals of opposite handedness within the unit cell (Fig. 3.1b).

In chiral systems, the structural chirality is predetermined by the lattice

structure during the formation process [51], making it challenging to manipulate the handedness of the system after growth.

Antiferro-chiral crystals are a special class of non-chiral crystals, in which sub-structures of opposite handedness coexist within the same unit cell. Boron phosphate (BPO_4, space group $I\bar{4}$) is a prototypical antiferro-chiral material (Fig. 3.1c). It crystallizes in a tetragonal structure and is a wide-bandgap insulator, with an electronic band gap of approximately 9 eV under ambient conditions [52].

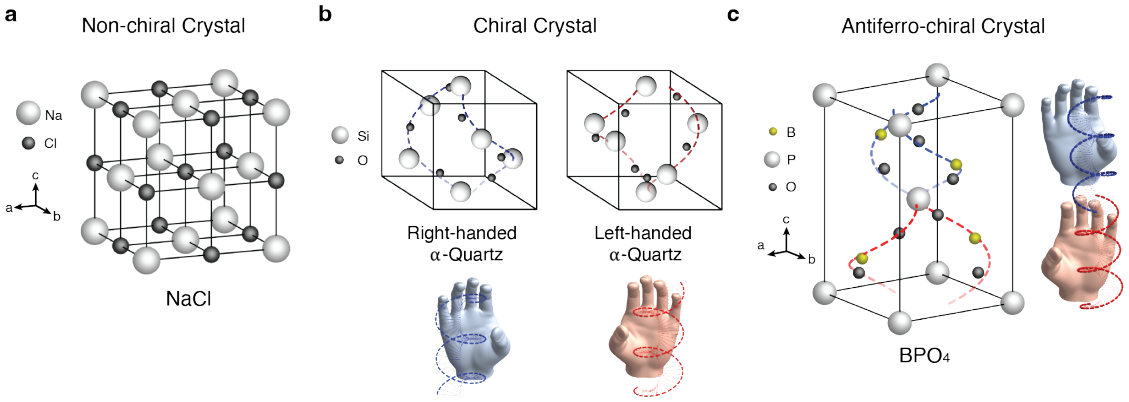

Figure 3.1: Chirality in solid system. (a) NaCl crystallizes in a non-chiral crystal structure. (b) The prototypical chiral crystal α-quartz exists in left- and right-handed configurations, determined by the spiral atomic structure formed during the growth process. (c) The unit cell of the antiferro-chiral crystal BPO_4 is composed of chiral sub-structures of opposite handedness. The equal presence of left- and right-handed sub-structures makes the overall system achiral.

3.2 Inducing Chirality in BPO_4

The equilibrium lattice of BPO_4 consists of left- and right-handed chiral sub-structures. The displacement of the atomic structure along the coordinates of B-symmetry modes (with amplitudes Q_B) lifts the degeneracy between the local structures of opposite handedness, resulting in a chiral state. As illustrated in Fig. 3.2a, the atomic motions along the B-mode coordinates enhance and reduce

the amplitudes of the left- and right-handed local chiral structures, respectively. From a symmetry perspective, the displacement of Q_B lowers the symmetry of the system from non-chiral point group $\bar{4}$ to the chiral point group 2.

In BPO_4, a displacive force on the B-symmetry phonon modes that control chirality can be achieved by driving either of the doubly degenerate infrared-active E-symmetry phonon modes, polarised along the crystal a and b axes respectively. According to the lowest-order coupling term of the form

$$U = -\alpha\, Q_{E,a}^2\, Q_B + \alpha\, Q_{E,b}^2\, Q_B, \tag{3.1}$$

the coherent drive of phonon mode $Q_{E,a}$ by a resonant THz frequency field exerts a rectified force on Q_B in the positive direction, leading to a positive transient displacement of the lattice along the B-mode coordinates away from equilibrium (Fig. 3.2b). Conversely, if the orthogonal mode $Q_{E,b}$ is resonantly driven, the transient displacement Q_B changes direction due to the opposite sign in the coupling term (Fig. 3.2c). Hence, the system can be driven into either one of the two opposite chiral states by controlling the polarisation of the THz frequency excitation pulse.

3.3 Theoretical Calculations

The light-induced chirality is simulated by considering the following two coupled equations of motion for the resonantly driven doubly-degenerate mode $Q_{E,a/b}(t)$ at about 19 THz frequency and the set of four anharmonically coupled B-symmetry modes $Q_{B,i}(t)$ $(i = 1 \ldots 4)$.

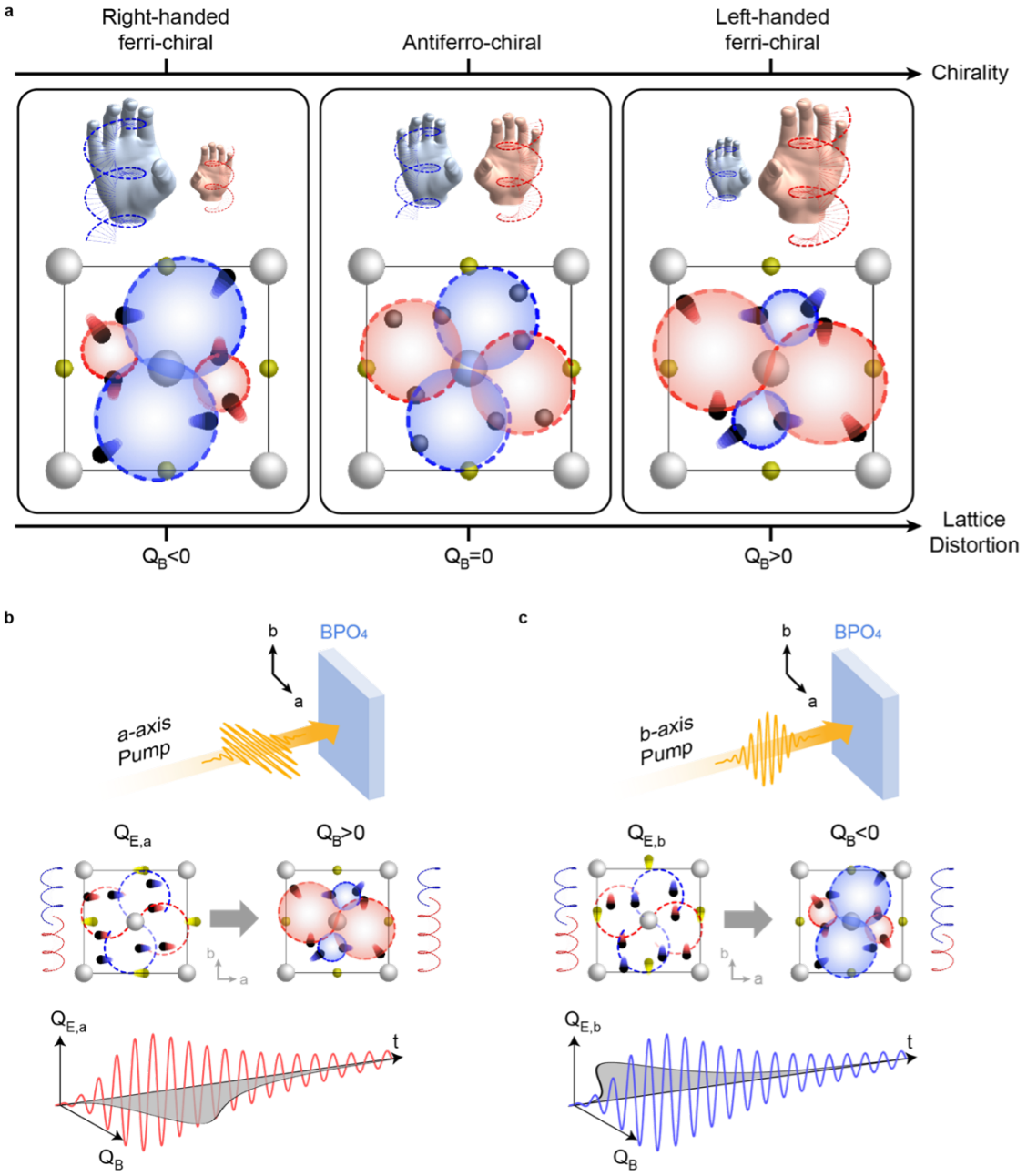

Figure 3.2: Light-induced chirality in antiferro-chiral BPO_4. (a) The atomic displacements in BPO_4 along B-symmetry phonons lift the degeneracy between the local structures of left and right handedness, driving the system from the antiferro-chiral into a ferri-chiral state. A displacement in the opposite direction induces chirality of opposite handedness. (b) A THz pump electric field polarisation along the a axis induces coherent oscillations of the $Q_{E,a}$ mode about its equilibrium position. A positive transient displacement along the B mode coordinates is induced via nonlinear phonon coupling, driving the system into a non-equilibrium ferri-chiral state with left handedness. (c) Exciting the doubly degenerate E-symmetry phonon along the b axis induces coherent oscillations of the $Q_{E,b}$ mode about its equilibrium position. A negative transient displacement along the Q_B mode coordinates is induced via nonlinear phonon coupling, driving the system into ferri-chiral state with right handedness.

$$\ddot{Q}_{E,a/b}(t) + \gamma_{E,a/b}\,\dot{Q}_{E,a/b}(t) + \omega^2_{E,a/b}\,Q_{E,a/b}(t) = Z^*_{E,a/b}\,E(t), \tag{3.2a}$$

$$\ddot{Q}_{B,i}(t) + \gamma_{B,i}\,\dot{Q}_{B,i}(t) + \omega^2_{B,i}\,Q_{B,i}(t) = \pm\alpha_i\,Q^2_{E,a/b}(t), \tag{3.2b}$$

where γ and ω are the damping constants and eigenfrequencies, and $Z^*_{E,a/b}$ is the mode-effective charge that couples the infrared-active $Q_{E,a/b}$ modes to the pulsed THz field

$$E(t) = E_0 \sin(\omega_c t) \exp\left(-\frac{t^2}{2\tau^2}\right). \tag{3.3}$$

Importantly, the sign of the force on the B-symmetry modes (right-hand side in Eqn. (3.2b)) depends on whether the E-symmetry mode is excited along the a or the b axis. DFT calculations are conducted to determine all the relevant phonon parameters and coeffiecients used in these equations.

The left panels of Figure 3.3 show these dynamics for excitation with the optical pump polarised along the crystal a axis. Figure 3.3a shows the THz electric field with a centre frequency of 19 THz and a peak field of 5 MV/cm. Figure 3.3b presents the oscillations of the resonantly driven E-symmetry phonon $Q_{E,a}$, polarised along the a axis. Figure 3.3c depicts the response of all four nonlinearly coupled B-symmetry modes, which are rectified by a force proportional to the square of the amplitude of $Q_{E,a}$ (see Eqn. (3.2b)). Figures 3.3d and 3.3e show the changes in permittivity and optical activity, respectively, arising from the combined rectified motion of all B-symmetry modes. Figures 3.3g–k display the corresponding data set for optical excitation along the crystal b axis.

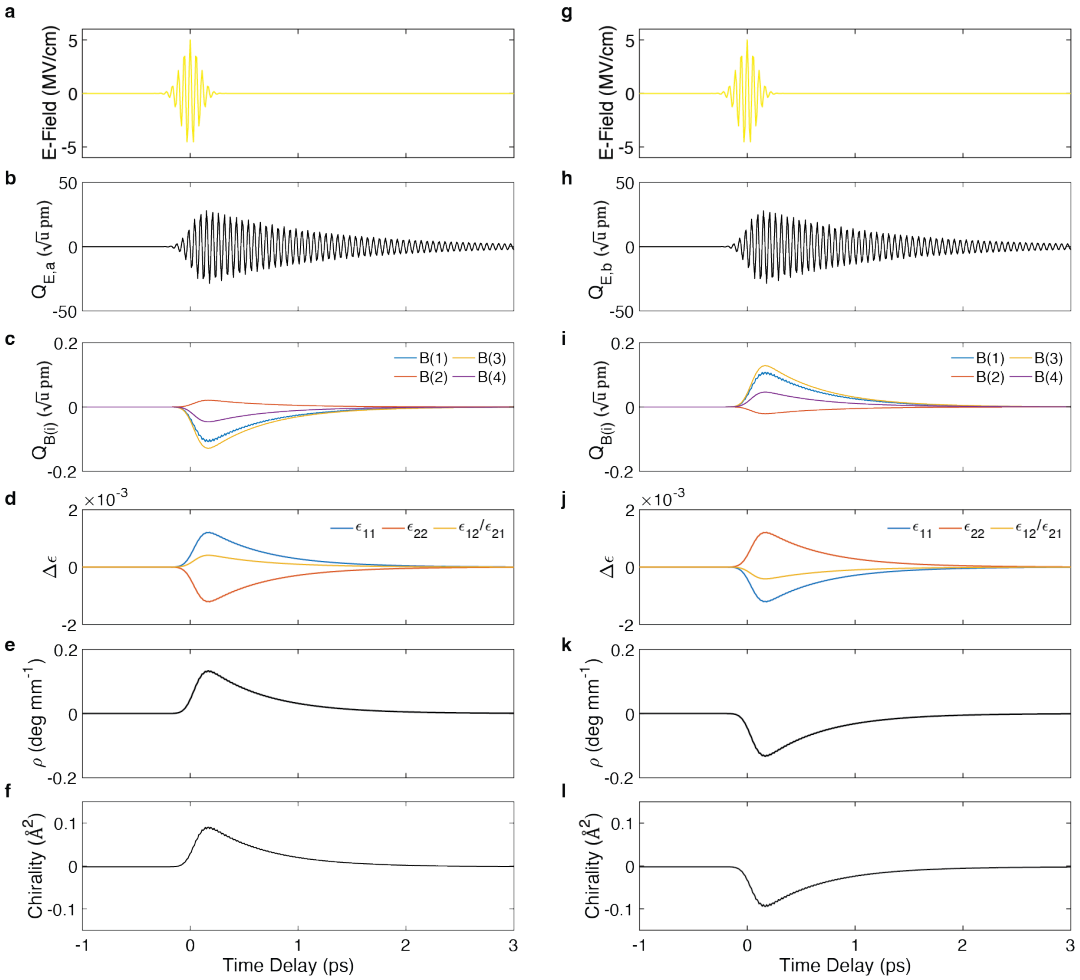

Figure 3.3: Simulation of nonlinear phonon dynamics. (a) THz pump field. (b) $Q_{E,a}(t)$. (c) Responses of four B-modes. (d) Permittivity change. (e) Rotary power change. (f) Chirality order parameter. (g–i) Equivalent data set for pumping along the crystal b axis

To quantify the transiently induced chirality, a geometric chirality order parameter [53] is defined as:

$$\vec{C} = \frac{1}{N} \sum_j \vec{r}_j \times \vec{d}_{ji}, \tag{3.4}$$

where $\vec{r}_j$ runs over the central sites (B and P), and $\vec{d}_{ji}$ corresponds to the bond direction vector to its neighboring oxygen atoms. In this definition, the order parameter vanishes at equilibrium when the system is non-chiral. And the system becomes chiral if $\|\vec{C}\| > 0$. The projection of $\vec{C}$ onto the principal axis allows to

determine the amount of left- or right-handedness of the structure. In Figures 3.3f and 3.3i, it is shown how this measure changes as a function of time, where positive and negative signs correspond to right- or left-handedness, respectively.

The induced chirality can be probed by measuring the polarisation rotation of a linearly polarised probe pulse propagating along the crystal c axis. To compute the total signal, both changes in rotary power and permittivity are taken into account. Figures 3.4a and 3.4b show the time-dependent changes in optical activity and the induced birefringence, respectively, for excitation of the $Q_{E,a}$ mode with the pump polarised along the a axis. The birefringence is derived from the change in the real part of the dielectric permittivity.

The optical activity alone generates a characteristic polarisation rotation which is independent of the incident polarisation of the probe light in the a-b plane [54, 55] (inset of Fig. 3.4a). The birefringence, on the other hand, introduces a modulation of the polarisation rotation response with a four-fold symmetry with respect to the incident probe polarisation (inset of Fig. 3.4b). The total polarisation rotation signal follows the form

$$\theta(\phi) = A_1\rho + A_2(\Delta n)^2 \sin\Big(4\phi - \psi\Big), \tag{3.5}$$

where ϕ is the relative angle between the pump and the probe polarisation, ψ is the angle between the pump polarisation and the optical axis of the transient birefringence, ρ is the rotary power proportional to the optical activity, and Δn is the birefringence-induced difference in refractive index. The overall time-dependent polarisation rotation signal, calculated as a function of the incident polarisation, is shown in Fig. 3.4c for a THz peak electric field of 5 MV/cm.

When the polarisation of the pump is oriented along the crystal b axis to excite the mode $Q_{E,b}$, the induced displacement of the B-symmetry modes changes direction. Hence, both the optical activity and the induced birefringence are reversed (Fig. 3.4d and 3.4e), resulting in a sign change of the overall polarisation rotation signal compared to the excitation along the a axis (Fig. 3.4f).

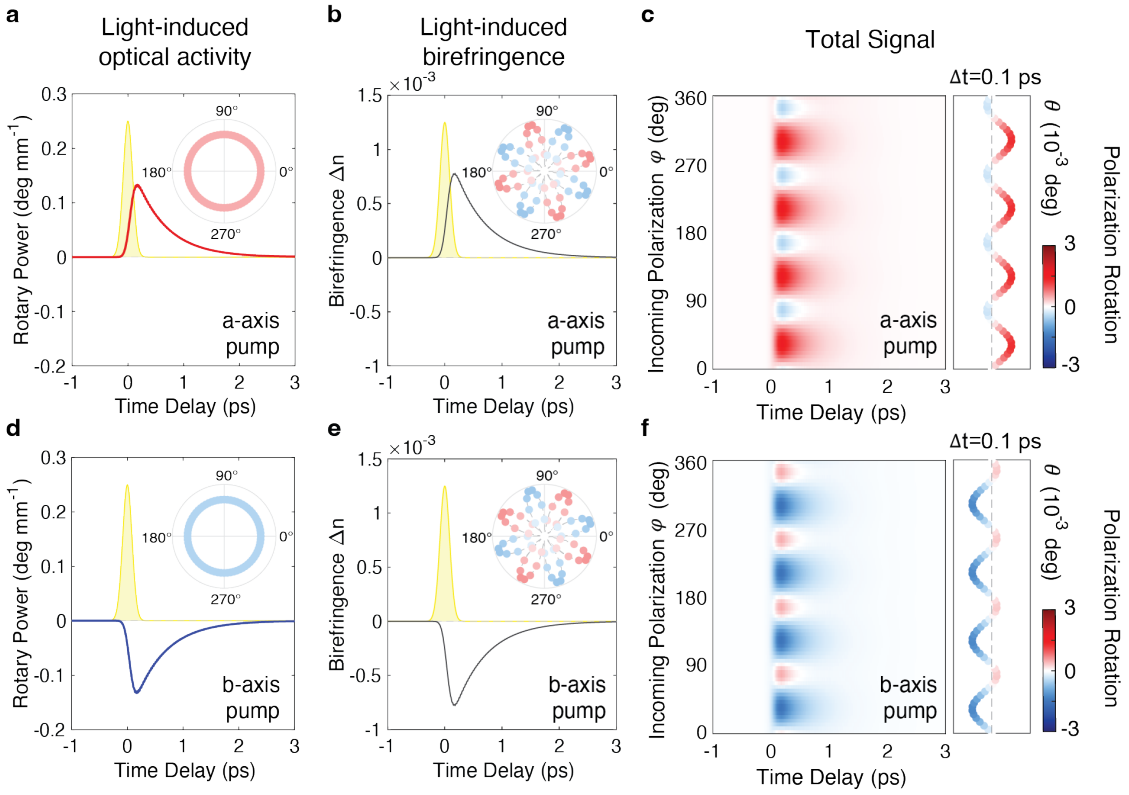

Figure 3.4: Theoretical calculations of light-induced chirality. (a) Light-induced optical activity for the a axis pump as a function of pump-probe time delay. The yellow shaded area is the temporal profile of the excitation pulse. Inset: the corresponding amplitude of the polarisation rotation signal as a function of incident polarisation. (b) Light-induced birefringence for the same a axis pump as a function of pump-probe time delay. Inset: the corresponding amplitude modulation of the polarisation rotation signal as a function of the incident polarisation. (c) The resulting total polarisation rotation signal for the a axis pump as a function of incident polarisation and pump-probe time delay. (d) Same as panel (a) for excitation along the b axis. (e) Same as panel (b) for excitation along the b axis (f) Same as panel (c) for excitation along the b axis. For all these calculations, 19 THz pump pulse with 5 MV/cm peak electric field is employed.

3.4 Experimental Demonstration

Static optical properties of single crystal BPO_4 in the THz frequency range were characterised by Fourier-transform infrared reflectivity (FTIR) measurements, with the electric field polarised along the a axis. Figure 3.5a shows all the four E-symmetry phonon modes of BPO_4 in the detected spectrum, which was fitted (Fig. 3.5b) with the following dielectric function for phonons [56]:

$$\varepsilon(\omega) = \varepsilon_\infty + \varepsilon_\infty \sum_j \frac{\omega_{\mathrm{LO},j}^2 - \omega_{\mathrm{TO},j}^2}{\omega_{\mathrm{TO},j}^2 - \omega^2 - i\,\omega\,\gamma_j}. \tag{3.6}$$

The fitting results are summarized in Table 3.1. In the experiments, the $E(2)$ mode at 18.9 THz was resonantly excited. The THz pulses used were carrier-envelope-phase (CEP) stable and characterised by electro-optic sampling at the sample position using a 50-μm thick GaSe crystal[57]. The corresponding freqeuncy spectrum is shown in Fig. 3.5c.

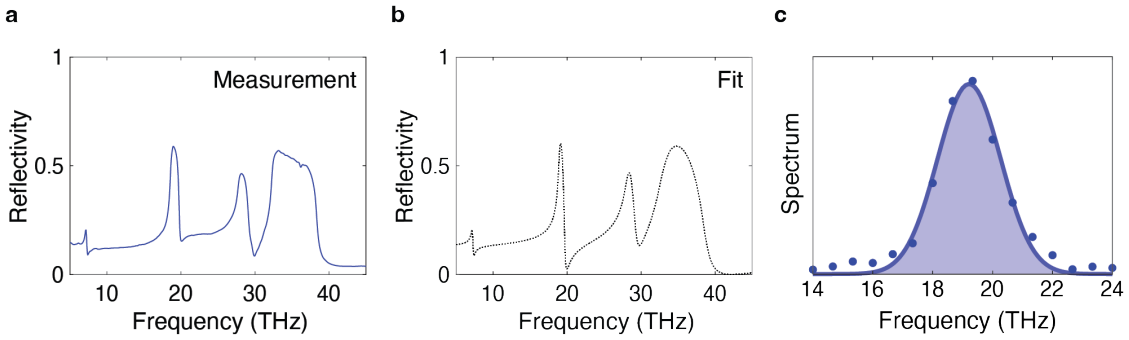

Figure 3.5: Preparation of phonon resonant pump. (a) The static reflectivity spectrum of BPO_4 with electric field polarisation along the a axis. (b) Fit of the measured spectrum using the dielectric function (Eqn. (3.6)) for phonons. c) Frequency spectrum of the THz pump pulse obtained by electro-optic sampling (EOS).

To experiementally validate the proposal, the optical setup illustrated in Figure 3.6a was used. The BPO_4 sample, held at room temperature, was excited by

Phonon Mode	$\omega_{TO,j}/2\pi$ (THz)	$\omega_{LO,j}/2\pi$ (THz)	$\gamma_j/2\pi$ (THz)	ε_∞
$E(1)$	7.2	7.4	0.24	/
$E(2)$	18.9	20.3	0.33	/
$E(3)$	28.2	30.5	0.96	/
$E(4)$	32.8	37.0	2.0	/
/	/	/	/	2.70

Table 3.1: Fitted E-symmetry phonons of BPO_4 polarised along the a and b axes.

19-THz centre frequency pulses of 3 THz full width at half maximum (FWHM), with an excitation fluence of 5.0 mJ/cm^2 and a corresponding peak electric field of 5.1 MV/cm. These pulses were linearly polarised along either the a or the b axis, resonantly driving each of the doubly degenerate E-symmetry phonon mode at its 18.9 THz TO frequency.

As shown in Figure 3.6b, a time-dependent rotation of the probe polarisation was induced by the phonon excitation with a pump polarised along the crystal a axis. At each probe polarisation angle, an onset of a rotation around time zero was observed, followed by a decay lasting few-picoseconds, longer than the 200 femtoseconds duration of the excitation pulse. The signal displayed a 90° periodicity with the incident probe polarisation due to the transient birefringence discussed above.

Since the modulation induced by the birefringence averages to zero over all the probe polarisations [58, 59], the transient optical activity can be extracted by averaging the signal over all the incident probe polarisations at each time delay (Fig. 3.6c). The result shows a finite and positive signal, providing clear evidence for a non-equilibrium chiral state. Its lifetime follows the decay time of the resonantly driven optical phonon.

Same measurement was taken with the pump polarisation rotated by 90° to

resonantly drive the E-symmetry phonon along the BPO_4 crystal b axis. The corresponding time-dependent polarisation rotation and the corresponding optical activity are shown in Figs. 3.6d and 3.6e. As expected, the signals reversed sign, evidencing opposite handedness of the light-induced ferri-chiral state compared to the a axis excitation. From symmetry considerations, the rotary power amplitude should be identical for pumping along the two orthogonal axes. The slight difference observed experimentally is likely due to small variations in pump–probe spatial overlap and to the fact that the sample surface is not perfectly aligned with the crystallographic ab plane.

Further measurements were conducted to validate the predicted nonlinear phononic mechanism. The rotary power was measured as a function of the peak electric fields of the 19-THz excitation pulse (Fig. 3.7a), evidencing a quadratic field dependence and a sign reversal for the two different pump polarisations. This behaviour is consistent with the nonlinear phonon interaction potential Eqn. (3.1).

In addition, the magnitude of the non-equilibrium rotary power was resonantly enhanced when the excitation pulses were tuned to the 18.9 THz transverse optical frequency of the doubly degenerate E-symmetry phonon (Fig. 3.7b). Notably, the light-induced rotary power of BPO_4 is comparable to the equilibrium value of α-quartz, a commonly used material for polarisation rotation in optics [60].

3.5 Experimental Setup for Measurements on BPO_4

A schematic of the pump–probe setup used in the experiment for the measurements on BPO_4 is shown in Fig. 3.8. The THz excitation pulses were generated by

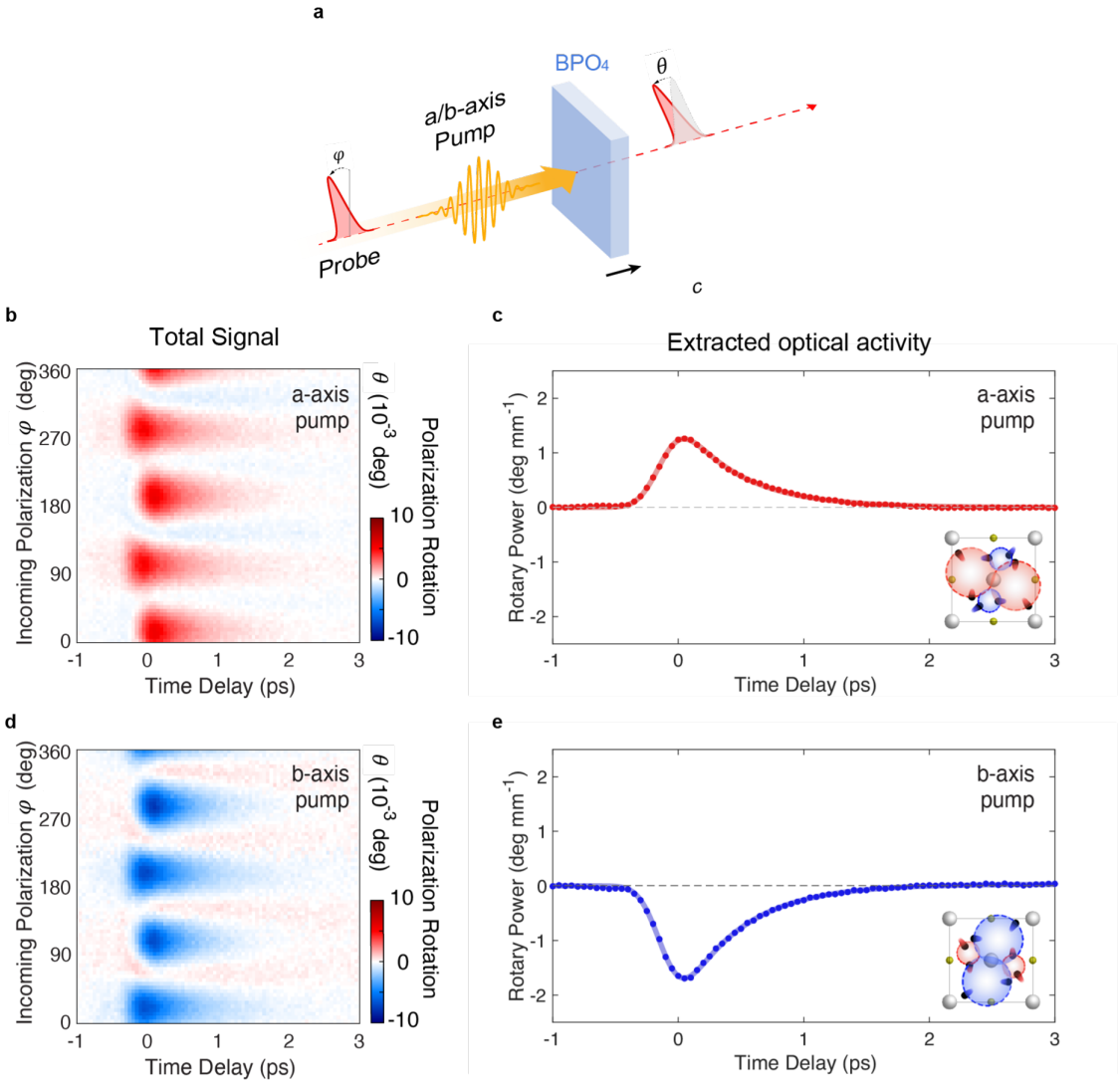

Figure 3.6: Time-resolved polarisation rotation measurements. (a) Schematic of the pump-probe experiment. A linearly polarised mid-infrared pulse, polarised along either the a or b axis, is used to drive the BPO_4 crystal into chiral states. A time delayed near-infrared pulse probes the state by the measurement of its polarisation rotation, carried out as a function of the probe incident polarisation. (b) Time delay dependent polarisation rotation signal for a axis excitation as a function of probe incident polarisation. (c) Time delay dependent rotary power, proportional to the optical activity, extracted from the data shown in panel (b) and considering the finite extinction depth δ of the excitation pulses. d) Same as panel (b) for b axis excitation. (e) Same as panel (c) for b axis excitation.

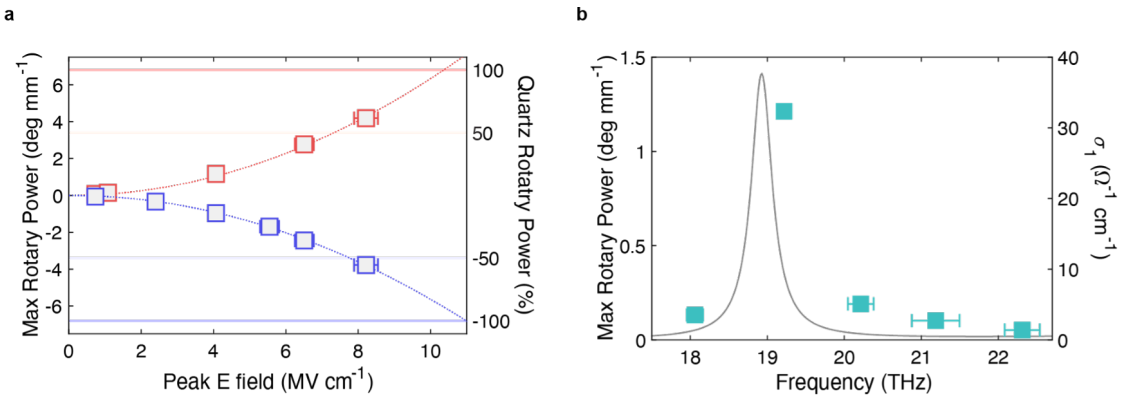

Figure 3.7: Characterisation of the light-induced ferri-chiral states. (a) The rotary power of the transient state as a function of the THz pulse peak electric field for a axis polarised (red) and b axis polarised (blue) excitation. (b) Maximum of rotary power at fixed peak electric field of 5.1 MV/cm as a function of the centre frequency of the excitation pulse. The horizontal error bars are the 1σ confidence interval of the pump centre frequency. Gray curve, real part of the optical conductivity.

difference frequency generation (DFG) in a GaSe crystal, using the two independently wavelength-tunable near-infrared signal outputs of two OPAs. The twin OPAs (Fig. 3.9) were seeded by the same white light and pumped by 1.5 mJ, 30 fs pulses at 800 nm wavelength from a Ti:sapphire amplifier operating at a 1 kHz repetition rate . An off-axis parabolic mirror was used to focus the THz beam onto the sample with a ∼70 µm FWHM spot size. The generated THz pulses were carrier-envelope-phase (CEP) stable and characterised by electro-optic sampling in a second GaSe crystal at the sample position [57].

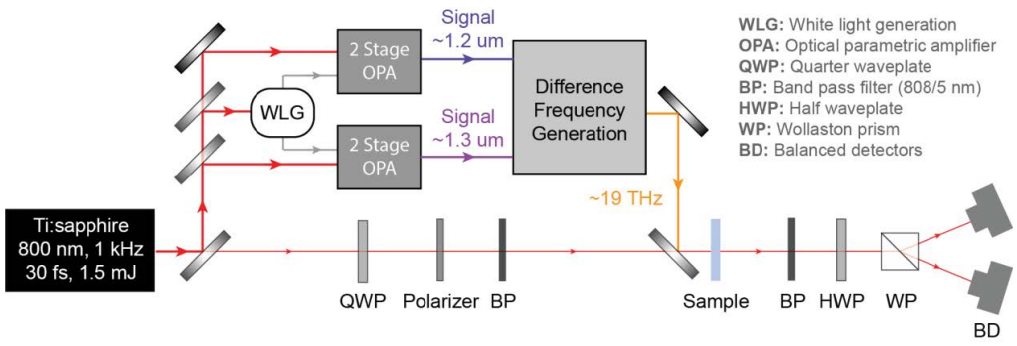

Figure 3.8: Schematic of the experimental setup for measurements on BPO_4.

The probe pulses for the polarisation rotation measurements in the BPO_4 (001) single crystal were sourced by the same amplifier system and focused onto the sample with a lens to a ∼30 µm spot. Polarisation control of the probe incident on the sample was achieved using a quarter-wave plate and a polariser. The pump-induced polarisation rotation was measured using a combination of a half-wave plate, a Wollaston prism, and two photodiodes.

The pump and probe beams were aligned collinearly and at normal incidence to the sample surface. Two identical narrow bandpass filters (centre wavelength 808 nm, bandwidth 5 nm) were placed before and after the sample to filter out high-frequency components in the time-resolved response induced by the Pockels effect, which—in contrast to the light-induced birefringence and optical activity—generates sidebands to the incident probe spectrum. The THz excitation pulses were linearly polarised along the *a*- or *b*-axis of BPO_4 crystal. All measurements were carried out at room temperature.

3.6 Summary

The results presented in this chapter demonstrate the induction of structural chirality via selective phonon excitation, marking the experimental realisation of active control over chirality in a crystalline solid. This represents an extension of the nonlinear phononics framework, which has already been successfully applied to manipulate material properties such as ferroelectricity [14, 32], magnetism [15, 61–63], and superconductivity [13, 64].

The emergence of chirality on the ultrafast time scale, together with the ability to switch between chirality of opposite handedness, offers opportunities

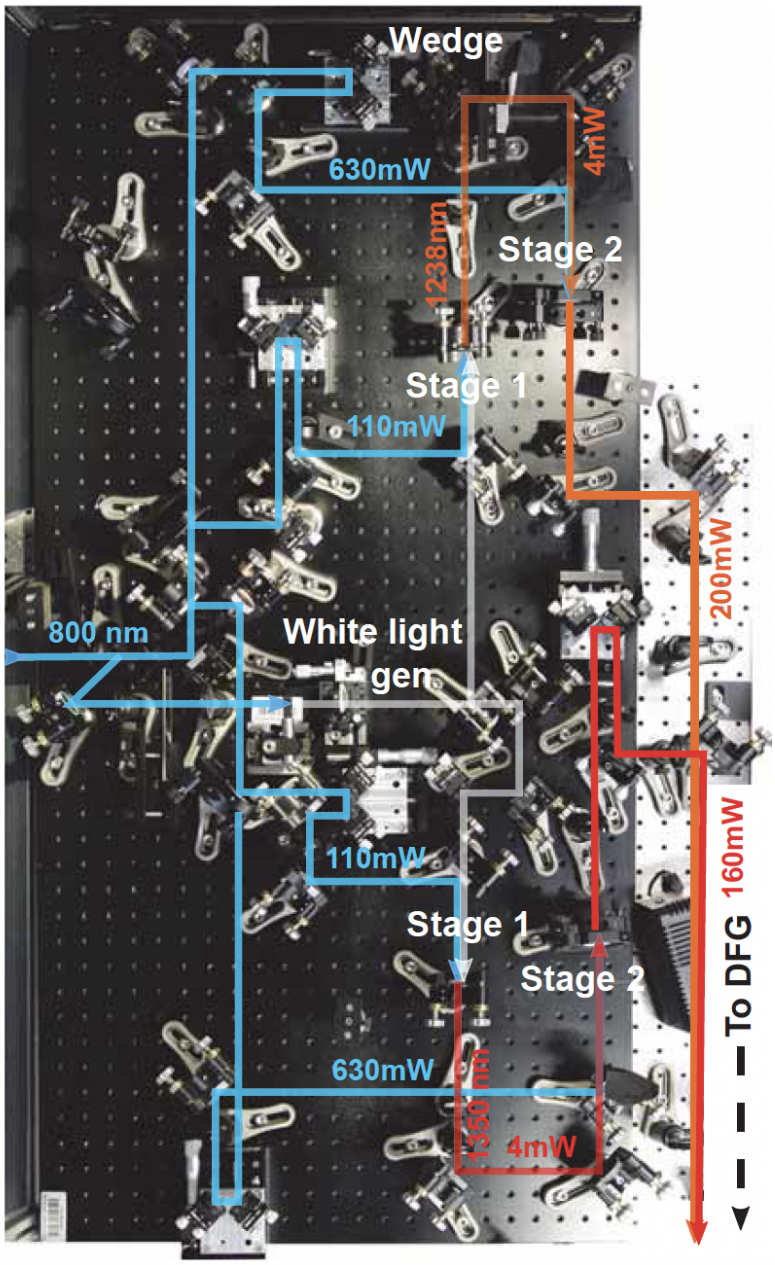

Figure 3.9: Setup for the generation of tunable near infrared pulses by optical parametric amplification. The OPA stages are followed by a difference frequency generation stage to generate mid-infrared pulses. *Adapted from Roman Mankowsky.*

for exploring new phenomena in out-of-equilibrium physics of complex matter, especially in topological [65–67] and correlated systems [68, 69] where chirality plays an important role.

As a perspective, antiferro-chiral systems offers an interesting platform for expanding our understanding of chiral control in solids. These systems inherently host sub-structures of opposite chirality within the unit cell, where strong coupling between structural chirality and external stimuli is anticipated. Such coupling mechanisms may enable tunable and efficient chirality control, making them attractive for potential applications. One particularly relevant area is enantioselective chemical catalysis, where the ability to dynamically modulate chirality could lead to new paradigms in reaction control and asymmetric synthesis.

Das ewig Unbegreifliche an der Welt ist ihre Begreiflichkeit.

The most incomprehensible thing about the universe is that it is comprehensible.

— Albert Einstein, *Physics and Reality* (1936)

4 Light Control of Ferroaxial Order

Contents

4.1 Ferroaxial Order **40**
4.2 Axial Field Engineering **42**
4.3 Static Characterisation of Ferroaxial $RbFe(MoO_4)_2$ . . **44**
4.4 Theoretical Calculations **46**
4.5 Experimental Demonstration **52**
4.6 Estimation of Pump-Induced Heating **56**
4.7 Experimental Setup for Measurements on $RbFe(MoO_4)_2$ **59**
4.8 Summary **62**

4.1 Ferroaxial Order

Ferroaxial order, also known as ferro-rotational order, is one of the fundamental ferroic orders in crystal systems. It is characterised by a rotational electric dipole texture [70] (Fig. 4.1). The ferroaxial order parameter is defined as

$$\vec{A} = \vec{r} \times \vec{P}, \tag{4.1}$$

the cross product of the position vector $\vec{r}$ and the local electric dipole moment $\vec{P}$. Notably, this axial order parameter is invariant under both spatial inversion and

time reversal operations, distinguishing ferroaxial order from other ferroic phases such as ferroelectricity and ferromagnetism.

The concept of axial order was first introduced in the 1980s as a form of long-range order emerging from spontaneous symmetry breakinge [71, 72]. The experimental studies of ferroaxial order is largely motivated by the recognition that ferroaxial order plays an important role in multiferroics by coupling the electric polarisation and magnetic chirality [73, 74].

A symmetry-based classification of ferroaxial transition was proposed by J. Hlinka [75] and further extended through analyses based on 'symmetry operation similarity' [76, 77].

Similar to other ferroic orders, the development of ferroaxial order from spontaneous symmetry breaking leads to the formation of different ferroaxial domains. This was first studied in the ferroaxial compound $RbFe(MoO_4)_2$ with rotational anisotropy second-harmonic generation (RA-SHG) [70].

Domain structures of ferroaxial have also been observed with scanning transmission electron microscopy [78], electric-field induced optical gyration effect [78, 79], circular dichroism SHG [80] and circular dichroism Raman spectroscopy [81].

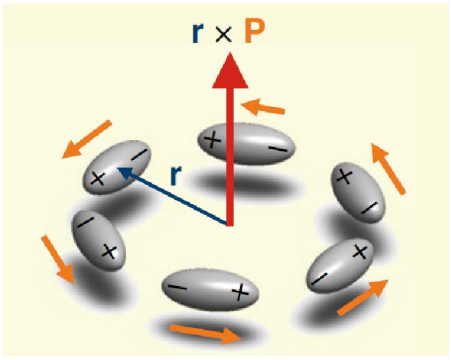

Figure 4.1: Schematic of ferroaxial (ferro-rotational) order. The order parameter $\vec{A} = \vec{r} \times \vec{P}$ is an axial vector invariant under inversion and time reversal. Adapted from [70]

4.2 Axial Field Engineering

Based on symmetry principle, direct external control of this order requires a conjugate field that transforms in the same way as the order parameter under all symmetry operations of the system. Such a field can be realised by the cross product of two different polar fields, $\vec{X} \times \vec{Y}$, applied simultaneously along two different directions.

However, combining conventional fields such as electric fields $\vec{E}$, thermal gradients ∇T or longitudinal strain gradients $\partial_i \varepsilon_{ii}$ in a well-controlled configuration is experimentally challenging [82, 83].

In certain systems, where the ferroaxial transition is accompanied by ferroelasticity, uniaxial strain has been used to control the crystallographic axis along which the ferroaxial order develops [84]. However, this approach does not set the direction of the axial vector $\vec{A}$; therefore, it cannot be used for ferroaxial domain switching to its opposite state. Switching of ferroaxial order by an electric field was reported in a charge density wave material [81], though the observed effect was attributed to the response of local electric dipoles at domain walls rather than a direct coupling to the ferroaxial order parameter.

A promising alternative involves the use of polar phonon modes, which can act as a polar field when coherently displaced. In this case, a ferroaxial conjugate field can be constructed as

$$\vec{F}(t) = \vec{Q}(t) \times \vec{E}(t). \tag{4.2}$$

with a terahertz (THz) light field $\vec{E}$ and the displacement $\vec{Q}$ of an infrared-active phonon resonantly driven by this field.

Linearly polarised THz pulses, which are commonly used to excite atomic motions parallel to the electric field [12, 20], are ineffective at coupling to ferroaxial order. This is because, in such configurations, the phonon mode coordinate $\vec{Q}$ and the electric field $\vec{E}$ are collinear, causing the axial field $\vec{F} = \vec{Q} \times \vec{E}$ to vanish.

This limitation can be overcome by employing circularly polarised THz pulses, which drive circular atomic motions when resonantly exciting a pair of degenerate phonon modes [85–88]. In this dynamical regime, both the electric field and the phonon displacement rotate continuously, while the cross product of the two fields $\vec{F} = \vec{Q} \times \vec{E}$ remains directionally fixed (Fig. 4.2). This configuration offers an experimentally accessible, symmetry-compatible conjugate field to ferroaxial order [89], whose direction can be controlled by the helicity of the THz electric field.

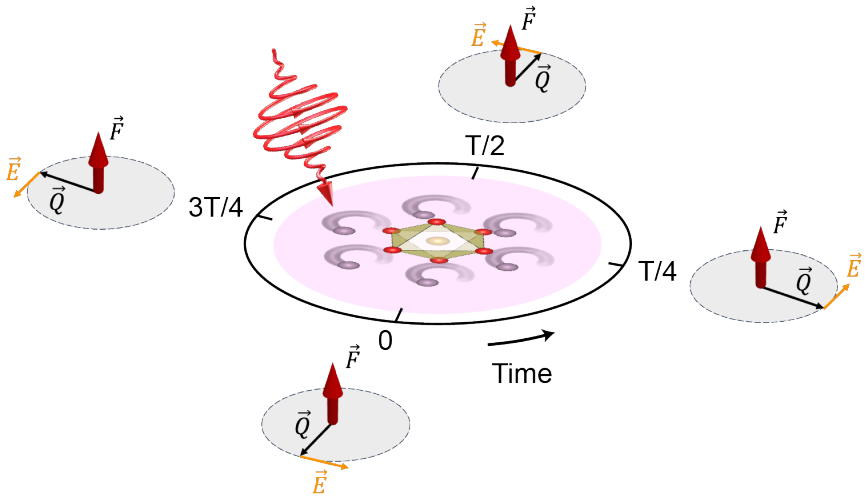

Figure 4.2: Circular phonon excitation as a conjugate field of axial order. A circularly polarised THz pulse, resonant with a doubly degenerate infrared-active phonon, excites circular phonon motion. At each moment during the drive, the electric field $\vec{E}$ and the phonon displacement $\vec{Q}$ are orthogonal, and the direction of the cross product of $\vec{Q} \times \vec{E}$ remains fixed.

Notably,

4.3 Static Characterisation of Ferroaxial $RbFe(MoO_4)_2$

The prototypical ferroaxial material $RbFe(MoO_4)_2$ has been chosen as the system for this study, as high-quality single crystals can be readily synthesized (Fig. 4.3a).As illustrated in Fig. 4.3b, $RbFe(MoO_4)_2$ undergoes a ferroaxial transition at approximately 190 K, breaking the mirror symmetry of the crystal and transforming the system from a high-symmetry state (point group $\bar{3}m$) to a low-symmetry state (point group $\bar{3}$).

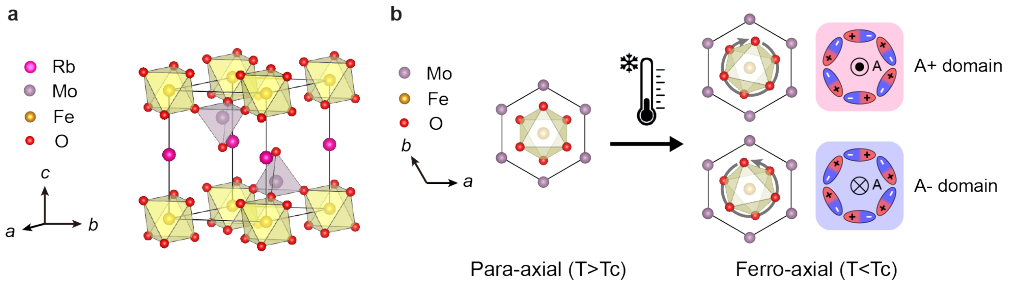

Figure 4.3: Ferroaxial transition in $RbFe(MoO_4)_2$. (a) The crystal structure of $RbFe(MoO_4)_2$. (b) The crystal structure viewed along c axis. Two ferroaxial domain states exist below T_C, corresponding to rotations of FeO_6 octahedra in different directions.

To experimentally characterise the ferroaxial order in the system, second harmonic generation circular dichroism (SHG-CD) probe was applied.

As a centrosymmetric system both above and below T_C, the static SHG signal originates mainly from the electric quadrupole (EQ) contribution [70], as expressed by

$$P_i(2\omega) = \chi^{\mathrm{EQ}}_{ijkl}\, E_j(\omega)\, \partial_k E_l(\omega). \tag{4.3}$$

In the experiment, the probe beam propagates along the crystal c axis and is polarised in the ab plane. Therefore, only tensor elements involving a field

gradient along z direction and field components in the xy plane are relevant. This simplifies Eqn. (4.3) to:

$$P_i(2\omega) = \chi_{ijk}^{\mathrm{EQ,eff}}\, E_j(\omega)\, \partial_z E_k(\omega). \tag{4.4}$$

Above the ferroaxial transition temperature T_{C}, there are only three non-zero components with one independent coefficient in the effective SHG tensor (Table 4.1). Below T_{C}, mirror symmetry is broken, allowing three additional non-zero tensor elements to emerge (Table 4.2). This symmetry breaking results in a measurable imbalance in the SHG signals when probed with right and left circularly polarised light. The SHG intensity for right-handed (E_+) and left-handed (E_-) circularly polarised incoming light are given by:

$$I_+ \propto |a|^2 E_+^4 + 2\,(b''a' - b'a'')\, E_+^4, \tag{4.5}$$

$$I_- \propto |a|^2 E_-^4 - 2\,(b''a' - b'a'')\, E_-^4, \tag{4.6}$$

where $a = a' + ia''$ and $b = b' + ib''$ are complex effective-tensor elements.

Moreover, SHG dichroism also provides information about the probed domain, as different domains yield dichroism signals with opposite signs (Fig. 4.4a).

$\boldsymbol{\chi}_{ijk}^{EQ,\mathrm{eff}}$		$\boldsymbol{i}$	
		x	y
$\boldsymbol{jk}$	xx	a	0
	yy	$-a$	0
	$xy(yx)$	0	$-a$

Table 4.1: Effective SHG tensor for $RbFe(MoO_4)_2$ in the para-axial state ($\bar{3}m$). Non-listed components are zero; a is the single independent coefficient.

The emergence of ferroaxial order in $RbFe(MoO_4)_2$ is evidenced by temperature-dependent SHG-CD, which displays a sharp increase to a finite value around 190

$\chi_{ijk}^{EQ,\text{eff}}$		i	
		x	y
jk	xx	a	$-b$
	yy	$-a$	b
	$xy(yx)$	$-b$	$-a$

Table 4.2: Effective SHG tensor for $RbFe(MoO_4)_2$ in the ferroaxial state ($\bar{3}$). New mirror-odd components appear with coefficient b.

K (Fig. 4.4b). This behaviour suggests a ferroaxial phase transition near 190 K, consistent with previous reports [90], and demonstrates that SHG dichroism is an effective method for probing ferroaxial order in $RbFe(MoO_4)_2$. Spatial mapping further reveals a multi-domain structure below T_C, with domain sizes on the order of 100 μm [79] (inset of Fig. 4.4b).

4.4 Theoretical Calculations

In $RbFe(MoO_4)_2$, the ferroaxial order develops along the crystal c axis and is associated with the axial mode Q_A, subject to a temperature-dependent potential $U(Q_A, T)$. Dynamically, this axial mode couples to the z-component of the conjugate field $\vec{F}(t) = \vec{Q}(t) \times \vec{E}(t)$ via the interaction potential

$$\Delta U = \alpha \, [\vec{Q}(t) \times \vec{E}(t)]_z \, Q_A. \tag{4.7}$$

Above T_C, $RbFe(MoO_4)_2$ is in a para-axial state described by a single-well potential for the axial mode. In this regime, a circular phonon excitation shifts the minimum of the well, transiently inducing as an axially polarised state (Figs. 4.5a and 4.5b). The direction of the torque applied on the ferroaxial soft mode is determined by the helicity of the THz excitation pulse.

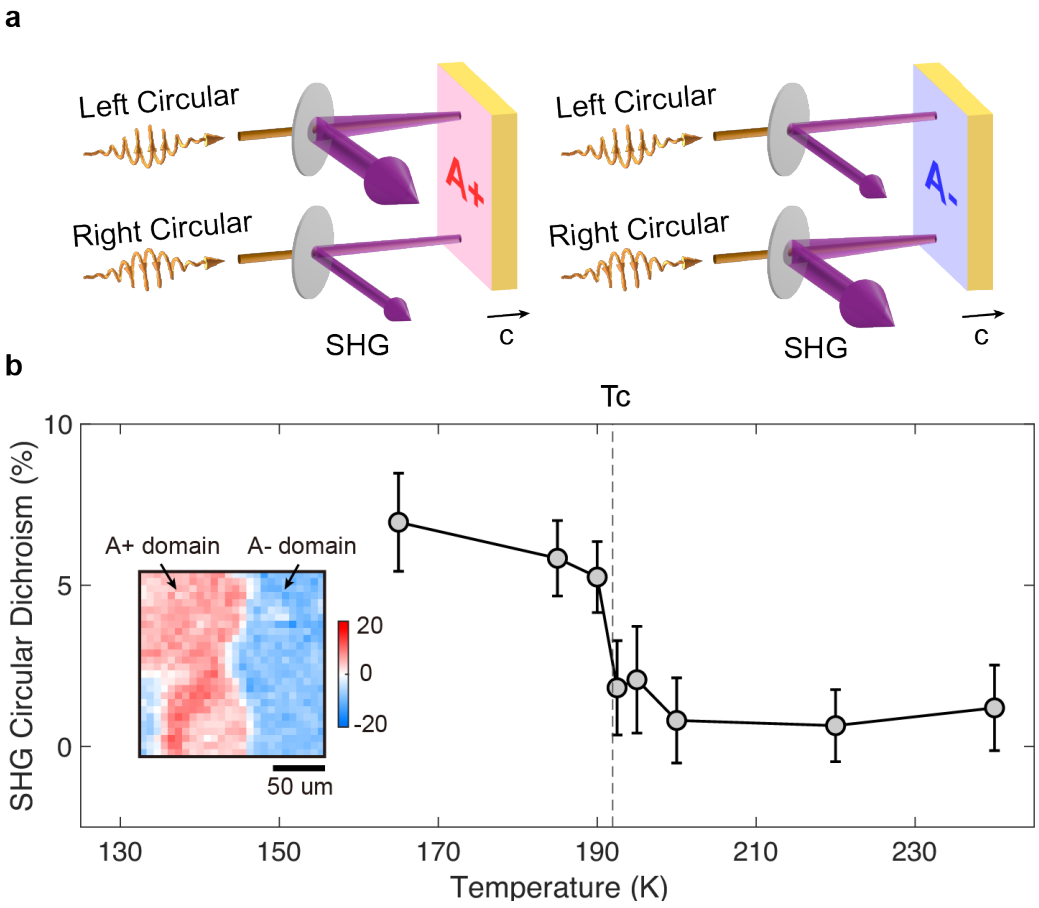

Figure 4.4: Probing ferroaxial order with second-harmonic generation circular dichroism (SHG-CD). (a) Schematic of the SHG-CD measurement. In the A^+ ferroaxial domain, the SHG intensity is higher for the left-circularly polarised probe than for the right-circularly polarised probe, yielding positive SHG-CD signal. In the A^- ferroaxial domain, the SHG intensity is lower for the left-circularly polarised probe than for the right-circularly polarised probe, yielding negative SHG-CD signal. (b) Ferroaxial transition characterised by SHG-CD. An increase in dichroism is observed at $\sim$ 190 K, suggesting a ferroaxial transition. Inset: SHG-CD domain mapping at 170 K (below T_C).

The phonon properties of $RbFe(MoO_4)_2$ have been investigated through numerical simulations based on density functional theory (DFT). Table 4.3 lists all the doubly degenerate optical phonon modes with E_u symmetry in $RbFe(MoO_4)_2$ at the Γ point and their respective mode effective charges, which quantify the coupling strength between each mode and the external electric field.

Among the six optical E_u phonon modes, the $E_u(7)$ mode exhibits the highest

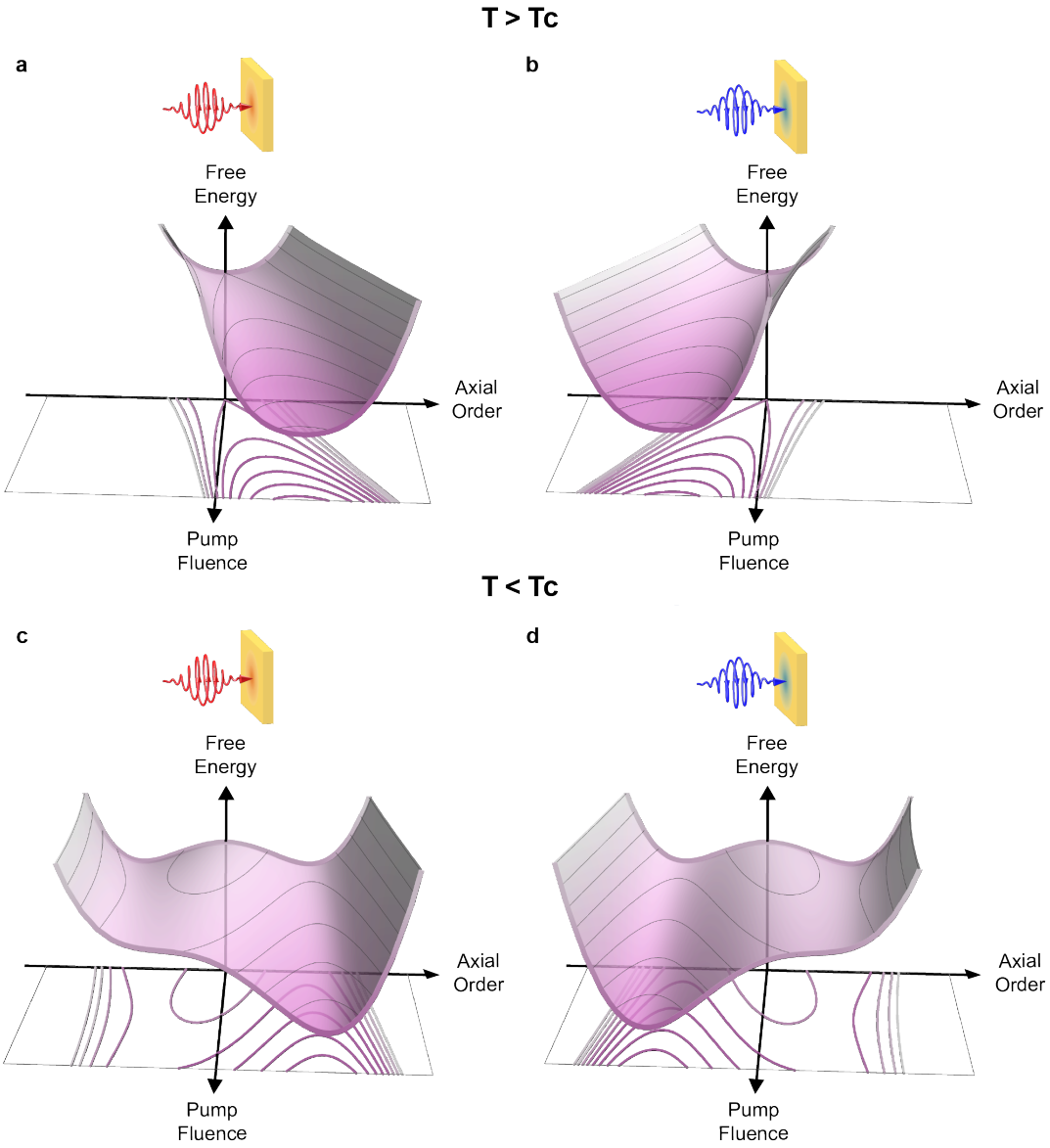

Figure 4.5: Potential energy landscapes of ferroaxial order under circular phonon drive. (a) Potential energy landscape of axial order in the para-axial state above T_C under left circularly polarised excitation. The circularly polarised excitation shifts the potential minimum from zero to a finite value of the axial order parameter. (b) same as (a), but with right circularly polarised THz excitation. The potential minimum shifts in the opposite direction. (c) Potential energy landscape of axial order under left circularly polarised excitation below T_C. A circularly polarised THz pump biases the double-well potential, favoring one domain over the other. (d) same as (c), but with right circularly polarised THz excitation. The opposite domain is favored.

mode effective charge and falls in the mid-infrared range (15-40 THz), where coherent light pulses are readily generated by difference frequency generation (DFG) process in the experiment. The $E_u(7)$ mode at 24 THz is thus selected to be pumped to control the ferroaxial order.

The coupling between the circular phonon excitation and the axial mode is evaluated by calculating the off-diagonal term of the mode effective charge tensor for the doubly degenerate Eu modes as a function of the axial mode displacement Q_A. This quantity characterises the trilinear coupling term (4.7), following the methodology established in a previous literature [89].

Mode	**Frequency** (THz)	**Mode effective charge** $\boldsymbol{Z^*}$ $(e/\sqrt{u})$
$E_u(2)$	1.18	0.11
$E_u(3)$	3.74	0.22
$E_u(4)$	6.91	0.94
$E_u(5)$	8.48	0.39
$E_u(6)$	10.71	0.02
$E_u(7)$	23.42	1.83

Table 4.3: Calculated E_u phonon modes of $RbFe(MoO_4)_2$ at Γ point.

The dynamics of the driven phonon and axial mode are captured by the following equations of motion:

$$\ddot{\vec{Q}}_{E_u} + \gamma_{E_u}\dot{\vec{Q}}_{E_u} + \omega_{E_u}^2\,\vec{Q}_{E_u} = Z^*_{E_u}\,\vec{E}(t), \tag{4.8}$$

$$\ddot{Q}_A + \gamma_A\,\dot{Q}_A + \frac{\partial U}{\partial Q_A} = \alpha\left[\vec{Q}_{E_u}(t)\times\vec{E}(t)\right]_z, \tag{4.9}$$

Here, γ_A and γ_{E_u} are the damping coefficients, ω_{E_u} the frequency of the driven phonon modes. $Z^*_{E_u}$ is the effective charge that couples the in-plane phonon displacement vector $\vec{Q}_{E_u}$ to the pulsed THz electric field

$$\mathbf{E}(t) = E_0\, e^{-t^2/2\tau^2} \begin{pmatrix} \cos\omega t \\ \cos(\omega t + \phi) \end{pmatrix}, \tag{4.10}$$

where the values $\phi = \pm\frac{\pi}{2}$ correspond to left- and right-circular polarisation, respectively.

As illustrated in Figure 4.6, a left circularly polarised THz pulse has equal electric field amplitudes on x and y directions, with a phase delay of $\pi/2$ between them. This induces a phonon excitation with the same helicity. The resulting conjugate field, $(\vec{Q} \times \vec{E})_z$, develops a transient positive value, following the overlap between the envelops of the driving field and the phonon oscillation. Reversing the helicity of the pump changes the phase delay to $-\pi/2$, which changes the sign of the transient conjugate field (Fig. 4.6b).

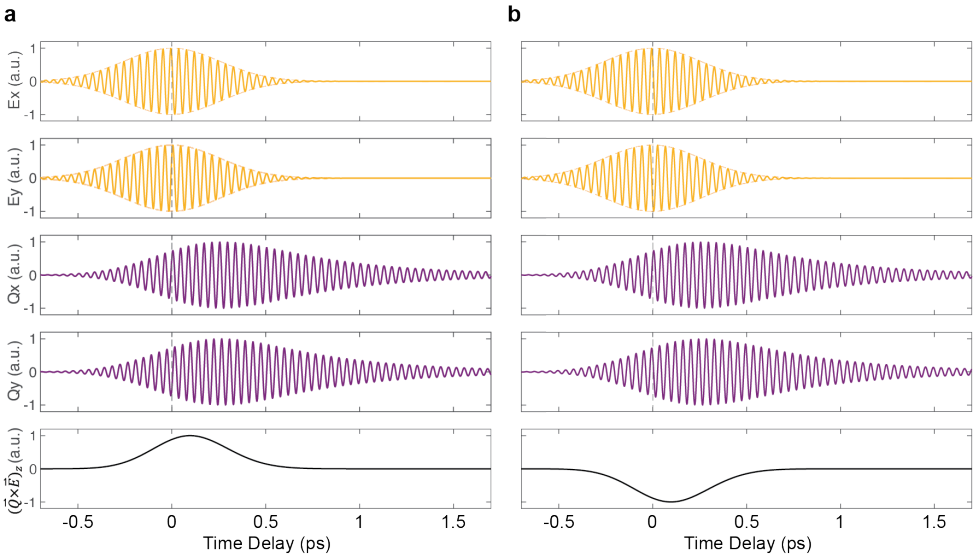

Figure 4.6: Simulation of the dynamical axial field induced by circularly phonon excitation. (a) Dynamics driven by a left circularly polarised THz pulse. From top to bottom: THz electric field pump polarised along the x and y directions, dynamics of the driven E_u phonon mode along x and y directions, and the resulting axial field. (b) Equivalent data set for pumping with the opposite helicity.

The response of the axial order to circular phonon excitation was calculated as a function of temperature above T_C, based on the dynamics of the transient axial field generated by a circularly polarised THz pulse at an excitation fluence of 6 mJ/cm^2. A left-circularly polarised THz pulse induces a transient positive axial order (Fig. 4.7a), while a right-circularly polarised THz pulse induces a transient negative axial order (Fig. 4.7b). In both cases, the amplitude of the transient order increases as the temperature approaches the ferroaxial transition temperature, reflecting the softening of the axial mode. The parameters of the axial mode were obtained from DFT calculations at zero temperature, while finite-temperature effects were incorporated based on the experimentally measured axial mode frequencies in the low-temperature phase [91].

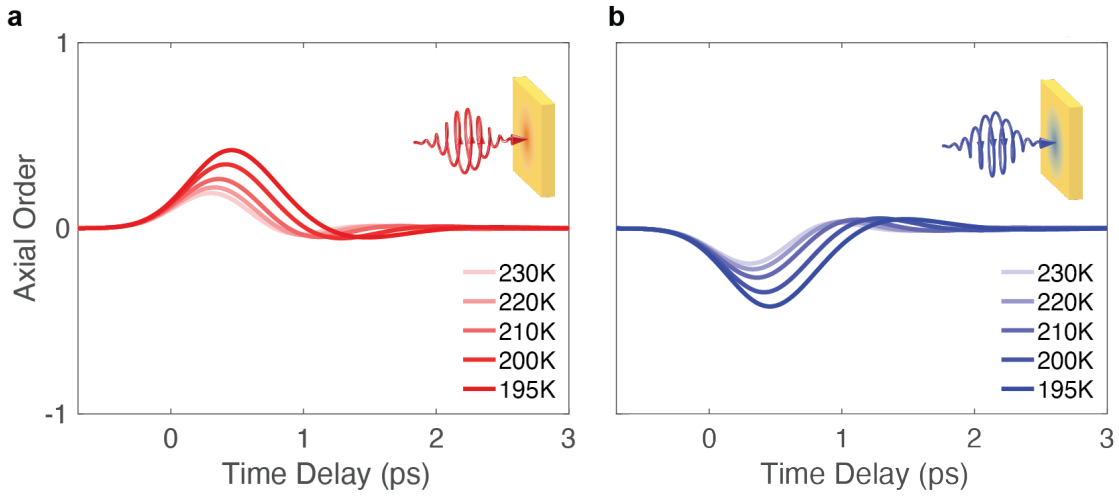

Figure 4.7: Calculated dynamics of the axial order for circularly polarised excitation pulses at different temperatures above T_C. (a) Transient A^+ axial order induced by a left-circularly polarised THz pulse. (b) Transient A^- axial order induced by a right-circularly polarised THz pulse.

The simulated dynamics as a function of fluence below T_C are shown in Figure 4.8. For the A^- ferroaxial initial state, a left-circularly polarised THz excitation pulse above a certain fluence threshold switches the state to the opposite A^+ state

(Fig. 4.8a), while the right-circularly polarised excitation leaves it in the A^- ferroaxial state (Fig. 4.8b). Conversely, for the A^+ ferroaxial initial state, switching to the A^- state is achieved with a right-circularly polarised excitation pulse above the threshold (Fig. 4.8c), while the left-circularly polarised excitation leaves the A^- state unchanged (Fig. 4.8d).

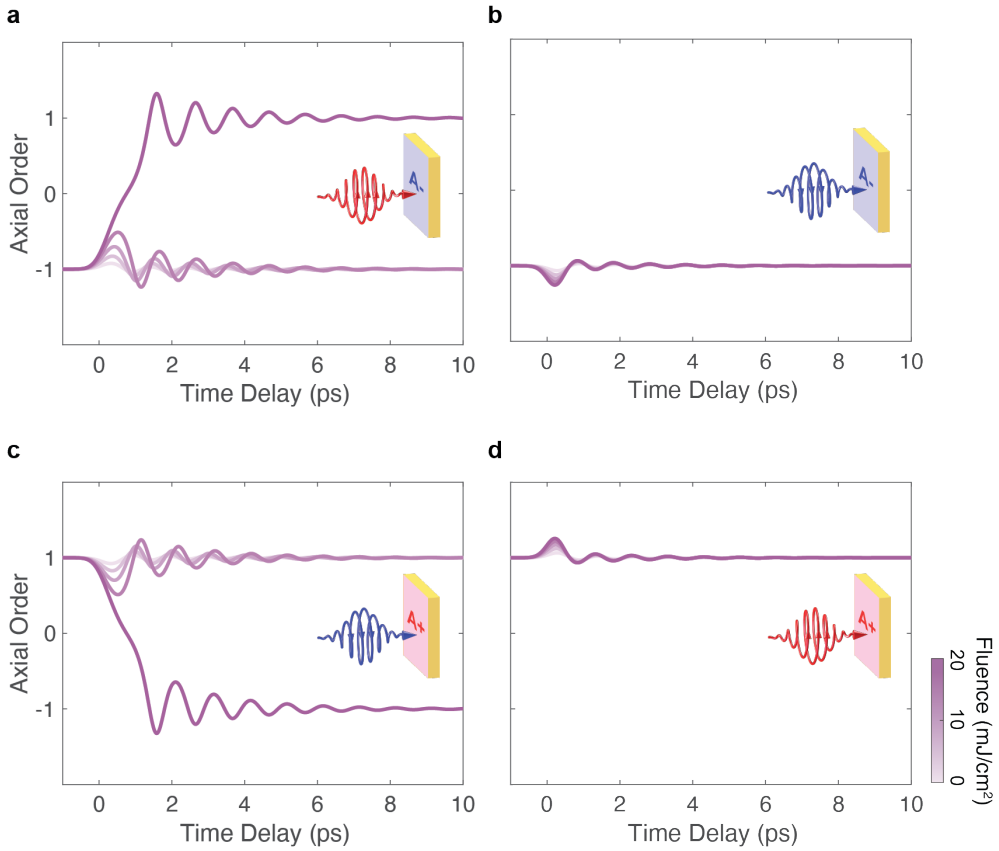

Figure 4.8: Calculated dynamics of axial order for circularly polarised excitation at different fluences below T_C (180 K). (a) Dynamics of an A^- ferroaxial initial state under left-circularly polarised THz excitation. (b) Dynamics of an A^- ferroaxial initial state under right-circularly polarised THz excitation. (c) Dynamics of an A^+ ferroaxial initial state under right-circularly polarised THz excitation. (d) Dynamics of an A^+ ferroaxial initial state under left-circularly polarised THz excitation.

4.5 Experimental Demonstration

To experimentally study the coupling between axial order and circular phonon excitation, circularly polarised THz light pulses were generated to resonantly

drive the selected infrared-active phonons in $RbFe(MoO_4)_2$ with the axial order characterised on an ultrafast timescale using second harmonic generation circular dichroism (SHG-CD) (Fig. 4.9a). The THz pulses were generated by difference frequency generation (DFG) process, with the frequency tuned to match the target phonon mode in the sample (Figs. 4.9b and 4.9c).

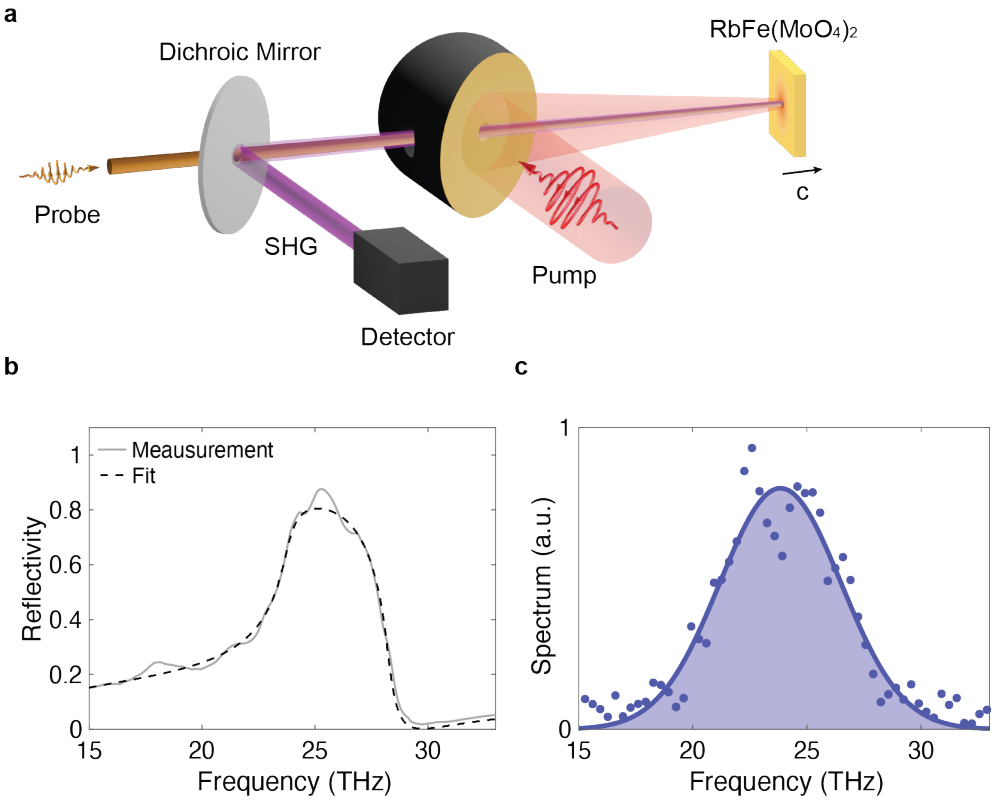

Figure 4.9: Pump–probe setup for the light control of ferroaxial order. (a) Schematic of pump-probe setup. Circularly polarised mid-infrared (MIR) pulse resonant with the phonon mode is used as pump. 800 nm circularly polarised pulse is used as probe with second harmonic generation collected with photodetector. (b) Measured reflection spectrum of the sample $RbFe(MoO_4)_2$, showing the infrared-active E_u phonon mode being pumped. (c) Frequency spectrum of the excitation pulse, characterised by Fourier transform infrared spectroscopy. The central frequency is tuned to 24 THz to match the phonon frequency in the material.

Figure 4.10a shows the time-resolved SHG-CD signal induced by excitation with a 600-femtosecond, left-circularly polarised THz pulse at a fluence of 6 mJ/cm^2 at

200 K (above T_C). The short-lived, positive SHG-CD signal reflects the emergence of a transient A^+ axial polarisation. Its lifetime suggests that the duration of the axial conjugate field is determined by the temporal overlap between the THz pulse and the resonantly driven phonon. Excitation with a right-circularly polarised THz pulse induced a short-lived negative SHG-CD signal (Fig. 4.10b), indicating a transient A^- axial polarisation. The helicity-dependent response above T_C is consistent with the model in which circular phonon excitation serves as the conjugate field for axial order.

The temperature dependence of the photo-induced axial state above T_C is shown in Fig. 4.10c. The amplitude of the transient SHG-CD signal, measured under left-circularly polarised excitation at a fixed fluence of 6 mJ/cm^2, increases as the sample temperature approaches T_C. This response of the axial order parameter is characteristic of ferroic systems, which exhibit increased susceptibility near phase transitions [92, 93].

The frequency dependence of the photo-induced axial state as a function of the centre frequency of the THz excitation pulses, measured at 200K and a constant excitation fluence of 6 mJ/cm^2, is shown in Fig. 4.10d. A resonant enhancement in the transient SHG-CD response is observed at 24 THz, corresponding to the frequency of the doubly degenerate in-plane E_u-symmetry phonon mode. The resonance verifies the essential role of resonant phonon excitation when inducing the axial order by light.

To study the domain switching behaviour below T_C, the sample was first cooled down to 180 K where multi-domain ferroaxial state forms. To investigate the fluence dependence of the ferroaxial state switching, single right-circularly polarised THz pulses were applied to a spot in the A^+ domain with increasing fluence. The static

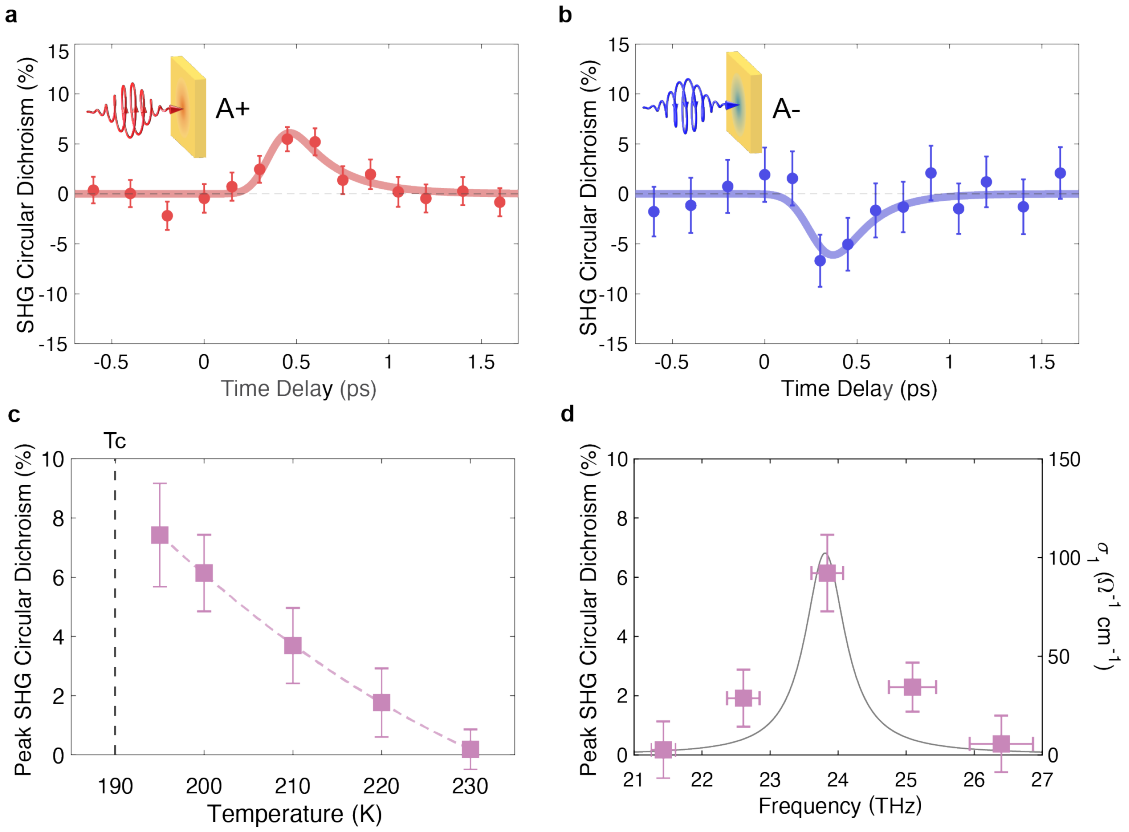

Figure 4.10: Photo-induced axial order in the para-axial state above T_C. (a) Time delay dependent SHG-CD measurement for left-circularly polarised excitation. (b) Time delay dependent SHG-CD measurement for right-circularly polarised excitation. (c) Peak amplitude of the transient SHG-CD response as a function of temperature above T_C. (d) Peak amplitude of the transient SHG-CD response as a function of the centre frequency of the excitation pulse. The gray curve corresponds to the real part of the optical conductivity. Vertical error bars denote the standard error of the mean. Horizontal error bars in (d) represent the 1σ confidence interval of the centre frequency of the excitation pulses.

SHG-CD signal was measured after each excitation pulse. As shown in Figure 4.11a, single THz pulses up to an excitation fluence of 12.5 mJ/cm^2 left the A^+ ferroaxial state unaffected with a positive static SHG-CD. A subsequent THz pulse with a fluence of 14 mJ/cm^2 inverted the static SHG-CD signal to a negative value, evidencing the ferroaxial state switching above this threshold.

This protocol was then repeated on the same sample spot, now in the A^- ferroaxial state, using left-circularly polarised THz pulses of opposite helicity. At

the same excitation fluence of 14 mJ/cm^2, the SHG-CD signal switched back to a positive value, characteristic of the A^+ state. (Fig. 4.11b).

To assess the robustness of the switching behaviour, a sequence of THz pulses with a fluence of 20 mJ/cm^2, above the switching threshold, and alternating helicities was applied to a different spot on the sample. Between successive pulses, static SHG-CD measurements were performed to monitor the ferroaxial state.

The spot was initially in the A^+ domain, as indicated by a positive static SHG-CD signal. After a single right-circularly polarised THz pulse, the static SHG-CD at the excited spot became negative with approximately the same magnitude, indicating that the A^+ state had been locally switched to the A^- state (Fig. 4.11c). In the next step, a single left-circularly polarised THz pulse of the same fluence but opposite helicity was applied to the same spot. Following this pulse, the static SHG-CD reverted to a positive value, evidencing a switch back to the A^+ state. Upon continued excitation with alternating helicities, the SHG-CD signal was observed to alternate between positive and negative values, demonstrating robust and reversible optical switching between the A^+ and A^- ferroaxial states.

4.6 Estimation of Pump-Induced Heating

To estimate the transient heating induced by the THz pump pulse, the energy density deposited in the sample is evaluated and converted into a temperature increase based on the estimated lattice heat capacity.

For an incident pump fluence F, a fraction of the energy is absorbed due to reflection at the sample surface. For a reflectivity R, the absorbed fluence is

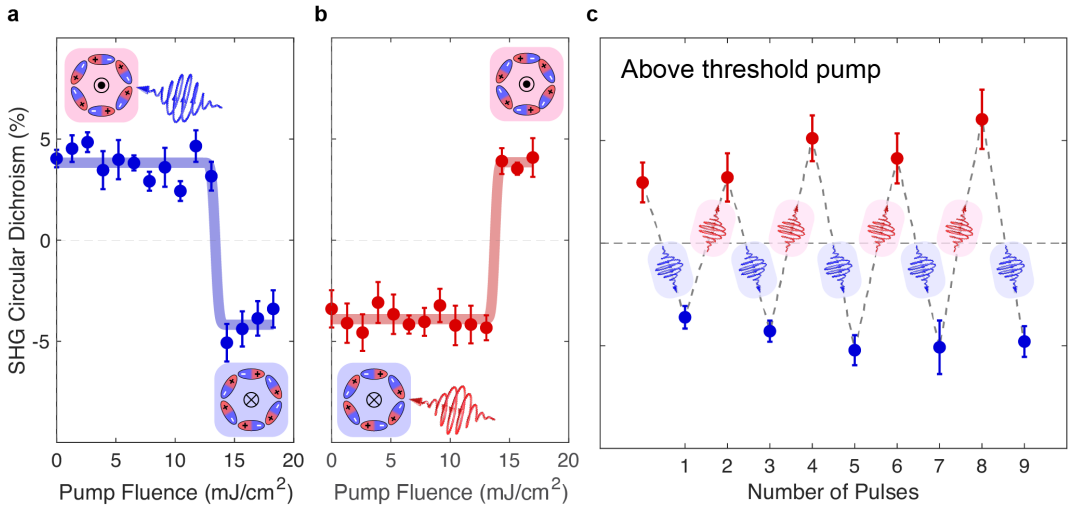

Figure 4.11: Switching of ferroaxial order below T_C (180 K). (a) SHG-CD measurements probing the ferroaxial order after each of the single, right-circularly polarised THz excitation pulses of increasing fluence. (b) Same measurement for left-circularly polarised single-shot pump pulses. (c) SHG-CD measurements tracking the ferroaxial domain state between successive THz excitation pulses of alternating helicity at a fixed fluence of 20 mJ/cm^2. Error bars denote the standard error of the mean.

$$F_{\text{abs}} = F(1 - R). \tag{4.11}$$

The deposited energy is distributed within the penetration depth of the pump. Because the pump pulse has a finite spectral bandwidth, the effective penetration depth is obtained by weighting the frequency-dependent penetration depth with the pump spectrum, yielding

$$d_{\text{eff}} \approx 1.0\,\mu\text{m}. \tag{4.12}$$

The absorbed energy density within the pumped volume is therefore

$$U = \frac{F_{\text{abs}}}{d_{\text{eff}}} = \frac{F(1 - R)}{d_{\text{eff}}}, \tag{4.13}$$

and the corresponding temperature increase is

$$\Delta T = \frac{U}{C_v} = \frac{F(1-R)}{C_v d_{\mathrm{eff}}}, \tag{4.14}$$

where C_v is the volumetric heat capacity of the lattice.

The heat capacity is obtained from the crystal density and the Dulong–Petit specific heat. Since $RbFe(MoO_4)_2$ is an insulating compound with a band gap of approximately 3 eV, the electronic contribution to the heat capacity is negligible, and the lattice contribution dominates.

The molar mass of $RbFe(MoO_4)_2$ is $M \approx 461.2\,\mathrm{g\,mol^{-1}}$. Using the unit cell volume $V_{\mathrm{cell}} \approx 2.3 \times 10^{-22}\,\mathrm{cm^3}$, the crystal density is

$$\rho = \frac{M}{N_A V_{\mathrm{cell}}} \approx 3.3\,\mathrm{g\,cm^{-3}}. \tag{4.15}$$

Using the Dulong–Petit approximation for a solid with $N_{\mathrm{atom}} = 12$ atoms per formula unit [93],

$$c_p \approx \frac{3N_{\mathrm{atom}}R}{M} \approx 0.65\,\mathrm{J\,g^{-1}K^{-1}}, \tag{4.16}$$

which corresponds to the high-temperature limit of the lattice heat capacity. The experiments are performed around $T \sim 200\,\mathrm{K}$, where the actual heat capacity is expected to be slightly smaller than this. The corresponding volumetric heat capacity is

$$C_v = \rho c_p \approx 2\,\mathrm{J\,cm^{-3}K^{-1}}, \tag{4.17}$$

which is typical for oxide crystals [94].

Substituting $R \approx 0.8$ and $d_{\mathrm{eff}} = 1\,\mu\mathrm{m} = 10^{-4}\,\mathrm{cm}$, we obtain

$$\Delta T = \frac{F(1-0.8)}{(2\,\mathrm{J\,cm^{-3}K^{-1}})(10^{-4}\,\mathrm{cm})}. \tag{4.18}$$

For a typical pump fluence used in the experiment, $F \sim 10\,\mathrm{mJ\,cm^{-2}}$, the temperature rise is

$$\Delta T \approx 10\,\mathrm{K}. \tag{4.19}$$

Thus the THz pump pulse produces a transient lattice temperature increase on the order of 10 K. For pump fluences used to switch the ferroaxial order from temperatures slightly below T_c, the estimated temperature increase may transiently bring the system above the transition temperature. In this case, a process involving transient melting of the ordered phase followed by re-establishment of the order upon cooling is possible. Further studies of the transition dynamics are required to clarify the role of such thermal processes in the switching mechanism.

4.7 Experimental Setup for Measurements on $RbFe(MoO_4)_2$

A schematic drawing of the pump–probe setup used in the experiments on $RbFe(MoO_4)_2$ is shown in Fig. 4.12. The THz pump pulses were generated by DFG in a GaSe crystal [36, 57], using the independently wavelength-tunable near-infrared signal outputs of two OPAs. The OPAs were seeded by the same white light and pumped by 11 mJ, 35 fs pulses at 800 nm wavelength from a Ti:sapphire amplifier operating at 1 kHz repetition rate. Following the DFG process, linearly polarised THz pump pulses were temporally stretched to ∼600 fs by passing through two 5 mm–thick

ZnSe crystals positioned at the Brewster angle. The THz spectrum was characterised by Fourier-transform infrared spectroscopy (Fig. 4.14A).

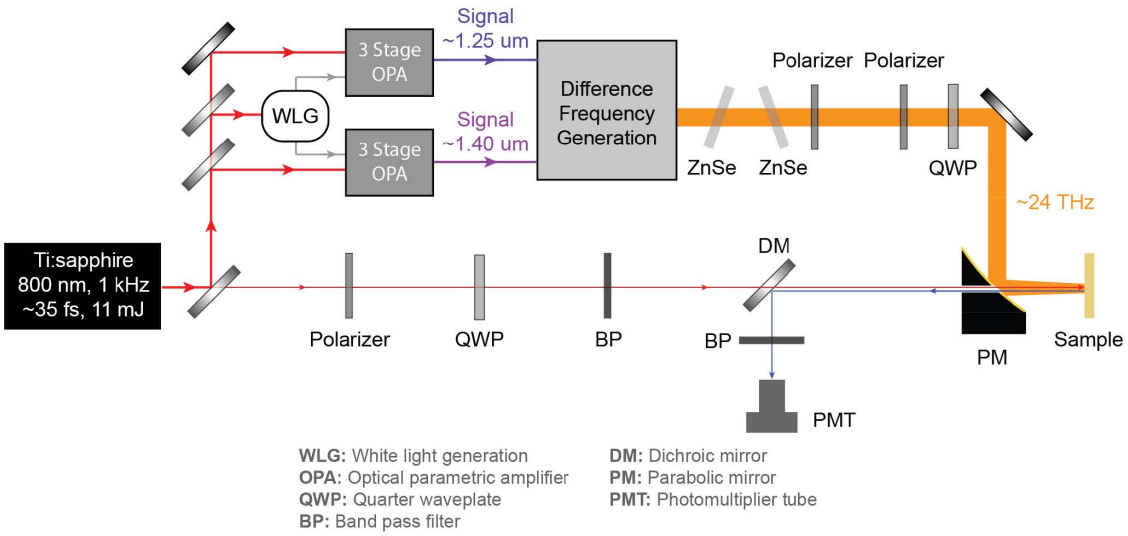

Figure 4.12: Schematic of the experimental setup for measurements on $RbFe(MoO_4)_2$.

A CdSe-based quarter-wave plate (ALPHALAS GmbH) induced circular polarisation of the THz pulses, which was characterised by detecting the optical power transmitted through a rotating linear polariser (Fig. 4.14B). A combination of two free-standing wire-grid polarisers before the quarter-wave plate were used to reverse the helicity of the THz excitation pulses between left- and right-circular polarisation and to control the excitation fluence without rotating the quarter-wave plate. This approach ensured identical alignment and spot position on the sample for both helicities. An off-axis parabolic mirror was used to focus the THz beam onto the sample with a ∼70 µm FWHM spot size.

The design of the twin OPA system used for the experiment is shown in Figure 4.13.

The probe pulses for the measurement of second-harmonic generation circular

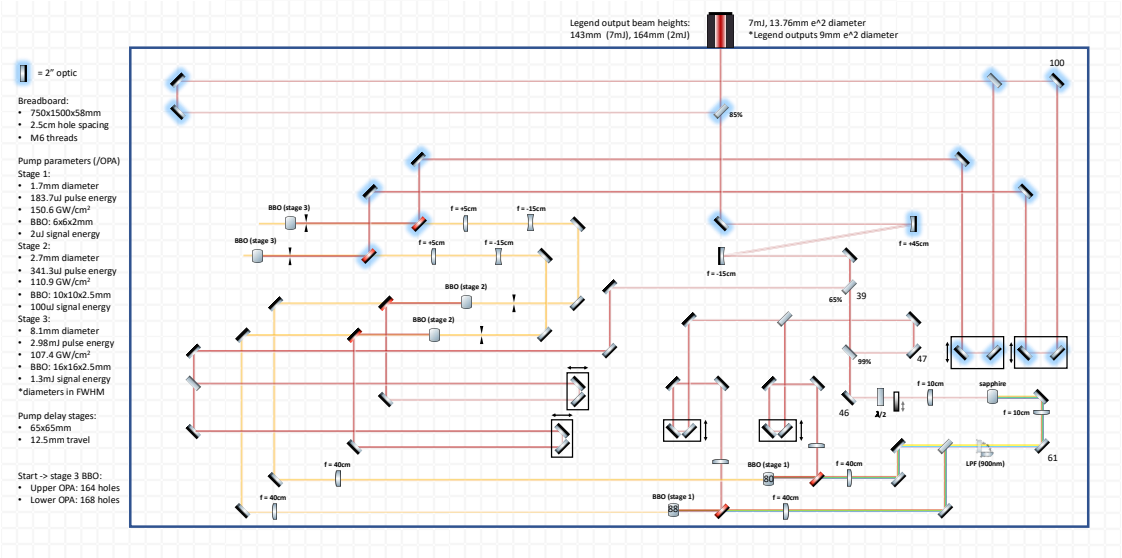

Figure 4.13: Design for the twin OPA system. *Adapted from Albert Liu.*

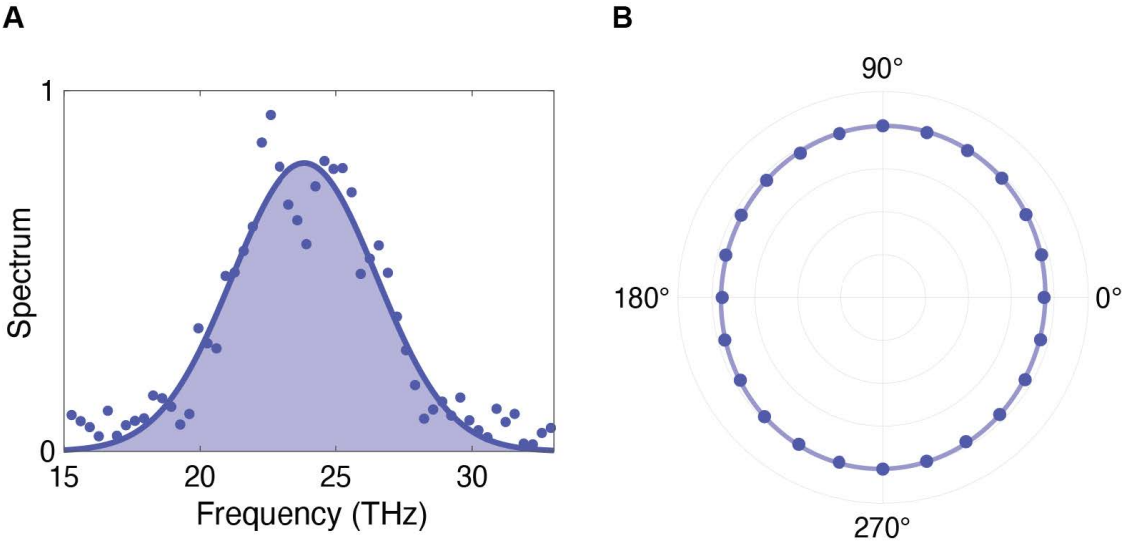

Figure 4.14: Characterisation of the THz excitation pulses. (A) Frequency spectrum of the excitation pulse, centreed at 24 THz, characterised by Fourier transform infrared spectroscopy. (B) Measurement of the polarisation state of the left-circularly polarised 24-THz excitation pulses, showing a 97% ellipticity.

dichroism (SHG-CD) were sourced by the same amplifier system and focused with a lens onto the sample to a spot size of ∼30 µm (FWHM). Circular polarisation of the probe incident on the sample was achieved using another quarter-wave plate. The SHG-CD signals were measured in reflection geometry with a coherence length of about 50 nm [95], shorter than the 500 nm extinction depth of the THz pump pulses at the phonon resonance. A pair of narrow bandpass filters was employed before and after the sample to filter out sideband components in the pump–probe measurements arising from electric-field-induced SHG. The filter before the sample transmitted at 808 nm (5 nm bandwidth), while the filter on the SHG output was centreed at 404 nm (2 nm bandwidth).

The pump and probe beams were aligned collinearly and at normal incidence to the surface of the *c*-cut $RbFe(MoO_4)_2$ single crystal, thereby preserving circular polarisation in both excitation and detection. All measurements were performed in an optical cryostat under vacuum conditions ($< 10^{-6}$ mbar).

For the preparation of single THz excitation pulses, two optical choppers with 10% duty cycle, synchronized to the Ti:sapphire amplifier system, were placed in the THz beam path before the sample, reducing the repetition rate from 1 kHz to 10 Hz. A synchronized fast shutter was then used to select single pulses for optical excitation.

4.8 Summary

The results presented in this chapter demonstrate the generation of an effective conjugate field for ferroaxial order [76]. This axial field, realised through circularly phonon excitation, successfully induces axial order above T_C and enables switching ferroaxial state below T_C in the prototypical ferroaxial system $RbFe(MoO_4)_2$

(Fig. 4.15a). As illustrated in Fig. 4.15b, this discovery experimentally identifies the conjugate field for ferroaxial order, completing the framework of couplings between ferroic orders and their corresponding conjugate fields. Owing to its symmetry-based design, the approach is expected to be broadly applicable across a variety of ferroaxial systems [76, 96–98].

The work also establishes a novel light-matter interaction scheme in which circularly polarised THz excitation drives an exotic ferroic order in crystal systems. Moreover, the ability of optically control ferroaxial state [99] opens opportunities for applications in data storage and next-generation electronic and magnetic devices [98, 100, 101], extending the family of functional materials controllable by ultrafast, symmetry-selective excitations.

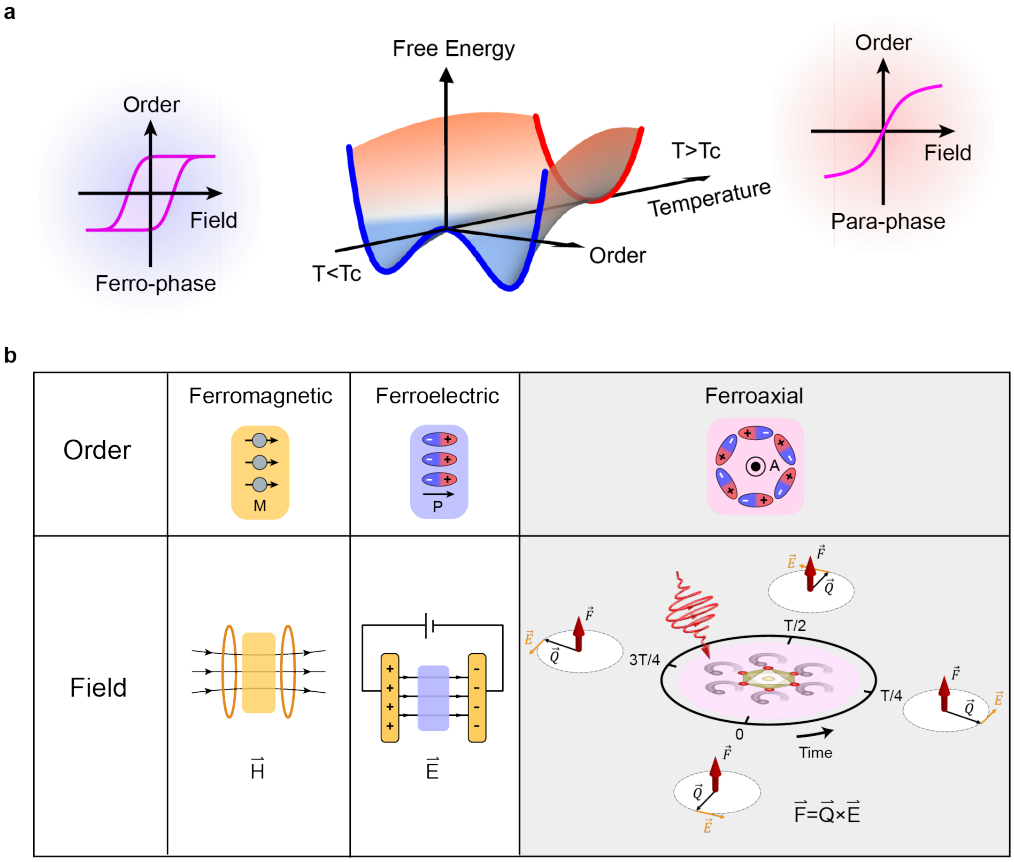

Figure 4.15: Effective conjugate field for axial order. (a) Schematic free energy landscape as a function of order parameter and temperature. Left: order parameter as a function of conjugate field below T_C. Right: order parameter as a function of conjugate field above T_C. (b) Similar to ferromagnetism and ferroelectric, circular phonon excitation serves as the conjugate for ferroaxial order.

道可道，非常道。名可名，非常名。

The Dao that can be stated cannot be eternal Dao. The Name that can be named cannot the eternal Name.

— Laozi, *Dao De Jing*

Es gibt keine ewigen Tatsachen, ebenso wie es keine absoluten Wahrheiten gibt.

There are no eternal facts, just as there are no absolute truths.

— Friedrich Nietzsche, *Human, All Too Human* (1878)

5 Conclusion and Outlook

This thesis has investigated how light-matter interactions can be employed to control emergent order in solids through nonlinear lattice dynamics. By resonantly exciting infrared-active phonons with intense laser fields at terahertz frequencies, nonlinear phonon-phonon interactions lead to transient and selective distortions of the crystal lattice [20]. These distortions can dynamically break the symmetry of the system and give rise to functionalities on an ultrafast timescale [12]. Two cases have been investigated: the induction of chirality in the antiferro-chiral crystal BPO_4 and the control of ferroaxial order in $RbFe(MoO_4)_2$.

Chapter 3 demonstrated that resonant excitation of selected phonon modes in BPO_4 can dynamically lower the crystal symmetry, giving rise to a transient chiral state and measurable optical activity. Theoretical analysis and symmetry considerations showed that linearly polarised light, when tuned to selectively excite one of the two degenerate phonon modes, induces a chiral distortion of the lattice. Changing the polarisation direction to drive the orthogonal mode results in the opposite handedness. This prediction was confirmed by time-resolved optical

measurements, which directly captured the light-induced breaking of inversion and mirror symmetries—demonstrating a key advance in the dynamic control of structural chirality.

In Chapter 4, resonant excitation of circular phonons was applied to control ferroaxial order in $RbFe(MoO_4)_2$. Theoretical analysis showed that circular phonon excitation generates an effective axial field that couples to the ferroaxial order parameter, with the direction of this field determined by the helicity of the phonon excitation. Ultrafast optical measurements confirmed that such selective phonon pumping enables reversible switching of the axial order in the ferroaxial phase and induces a transient axial polarisation in the para-axial phase. These findings highlight the fundamental role of lattice dynamics in enabling symmetry-selective control over exotic ferroic orders in solids.

These findings illustrate the powerful capability of selective phonon pumping as a tool for engineering material functionalities. In particular, applications to correlated systems represent a promising but largely unexplored frontier. In these systems, the intricate interplay between charge, spin, orbital, and lattice degrees of freedom lead to rich phase diagrams and emergent phenomena. Selective control of the lattice structure and symmetry provide a pathway to stabilize novel electronic or magnetic phases [102, 103]. It also enables dynamical tuning of interactions and switching between competing ground states. Materials with strong electron-phonon coupling or proximity to structural instabilities are especially compelling candidates for such investigations.

Beyond linearly and circularly polarised excitation schemes, future studies in this field may explore phonon driving using elliptically polarised light as well as

multi-frequency fields that generate Lissajous trajectories. These more complex field configurations could enable coupling to otherwise inaccessible order parameters and activate new types of lattice dynamics, further expanding the landscape of light-induced phases and functionalities.

In conclusion, the work presented in this thesis establishes a pathway for the dynamic control of symmetry and order in solids through light–matter interactions. Through resonant phonon excitation and the exploitation of nonlinear phonon interactions, fundamental material properties can be manipulated on ultrafast timescales. As experimental and theoretical techniques continue to advance, this approach is expected to play an increasingly important role in the design and manipulation of functional and quantum materials.

Appendices

Il n'y a qu'un héroïsme au monde : c'est de voir le monde tel qu'il est et de l'aimer.

There is only one heroism in the world: to see the world as it is and to love it.

— Romain Rolland, *Jean-Christophe*

A

First-Principles Calculations of Nonlinear Phonon Couplings

Contents

A.1 Computational Framework 69
A.2 BPO_4 70
A.3 $RbFe(MoO_4)_2$ 72

In this appendix, the density functional theory (DFT) calculations used to determine phonon parameters, nonlinear phonon coupling coefficients in BPO_4 and $RbFe(MoO_4)_2$ are described.

A.1 Computational Framework

All calculations were performed using the Vienna *Ab-initio* Simulation Package (VASP) [104–106], with phonon-related computations carried out using the PHONOPY software package [107]. The Projector Augmented Wave (PAW) method [108] was employed to generate the pseudopotentials.

Local Density Approximation (LDA) was adopted for the exchange–correlation functional. Structural relaxations were performed until the total energy convergence criterion of 10^{-8} eV was met. A plane-wave energy cutoff of 600 eV is used to expand the electronic wavefunction. And a Monkhorst-Pack [109] k-point grid of $7 \times 7 \times 5$ were used for Brillouin-zone sampling.

Phonon frequencies and eigenvectors were obtained via the finite-displacement method. Nonlinear phonon couplings were extracted using the frozen-phonon approach by fitting the total energy change as a function of atomic displacements.

The calculation of dielectric and optical properties in BPO_4 are performed under independent particle approximation with the LOPTICS tag in VASP [110]. Convergence for optical properties was ensured by increasing the k-point mesh to $17 \times 17 \times 11$ and including 400 empty states.

The following sections describe the specific computational details and results for BPO_4 and $RbFe(MoO_4)_2$.

A.2 BPO_4

First-principles calculations in the DFT framework were applied to explore the phonon properties, anharmonic lattice coupling coefficients, and the optical response of BPO_4. The configured default pseudopotentials were used for B ($2s^2 2p^1$), P ($3s^2 3p^3$), and O ($2s^2 2p^4$).

The starting point of the calculations was the tetragonal cell of BPO_4, with an equilibrium volume $V_{\text{cell}} = 122.8$ Å^3 ($a = b = 4.30$ Å, $c = 6.62$ Å). The atomic positions correspond to Wyckoff sites: B ($2d$), P ($2a$), and O ($8g$) at (0.259, 0.141, 0.127). The relevant phonon eigenfrequencies and eigenvectors at

the Brillouin zone centre were determined, and the nonlinear coupling coefficients in the coupling term (Eq. 3.1) were obtained using the frozen-phonon approach. The results are summarized in Table A.1.

Phonon Mode	$\boldsymbol{\omega_{TO}/2\pi}$ (THz)	$\boldsymbol{\alpha}$ (meV/u$^{3/2}$Å^3)	$\boldsymbol{Z^*}$ ($e/\sqrt{u}$)
E(2)	18.1	–	0.76
B(1)	15.8	1.16	0.85
B(2)	17.6	39.93	0.37
B(3)	28.1	–16.62	0.87
B(4)	31.5	105.59	1.57

Table A.1: Relevant parameters of the optical phonons involved in the light-induced chiral state, obtained from DFT calculations: transverse optical phonon frequency, nonlinear coupling coefficient, and mode effective charge.

To relate structural distortions to the polarisation rotation signal, the changes in the symmetric and antisymmetric parts of the dielectric tensor arising from the lattice distortions along the coordinates of the four transiently displaced B-symmetry modes and the directly driven E(2) mode were computed. The results are listed in Tables A.2 and A.3.

Phonon Mode	$\partial\varepsilon_{11}/\partial Q_{B,i}$ (10^3 u$^{-1/2}$Å^{-1})	$\partial\varepsilon_{12}/\partial Q_{B,i}$ (10^3 u$^{-1/2}$Å^{-1})	$\partial\rho/\partial Q_{B,i}$ ($^\circ$ mm^{-1} u$^{-1/2}$Å^{-1})
B(1)	31	31	-23
B(2)	33	-8	-14
B(3)	5	5	-8
B(4)	-36	-44	-60

Table A.2: Phonon amplitude–dependent changes in the dielectric tensor elements and the optical activity relevant for the light-induced chiral state, obtained from DFT calculations for phonon modes with B-symmetry.

Phonon Mode	$\partial^2\varepsilon_{11}/\partial Q^2_{E,i}$ (10^3 u^{-1}Å^{-2})	$\partial^2\varepsilon_{12}/\partial Q^2_{E,i}$ (10^3 u^{-1}Å^{-2})	$\partial^2\rho/\partial Q^2_{E,i}$ ($^\circ$ mm^{-1} u^{-1}Å^{-2})
E(2)	0.03	0.009	1.0

Table A.3: Phonon amplitude–dependent quadratic changes in the dielectric tensor elements and the optical activity relevant for the light-induced chiral state, obtained from DFT calculations for the driven mode with E-symmetry.

A.3 $RbFe(MoO_4)_2$

For $RbFe(MoO_4)_2$, the same computational framework was employed with the addition of a Hubbard U correction ($U = 4$ eV, $J = 0$ eV) to account for the localized Fe $3d$ electrons [89]. The pseudopotentials used correspond to Rb ($4p^6 5s^1$), Fe ($3p^6 3d^7 4s^1$), Mo ($4d^5 5s^1$), and O ($2s^2 2p^4$).

The starting point was the $P\bar{3}m1$ high-temperature crystal structure, which was fully relaxed. The resulting lattice parameters and atomic coordinates are presented in Table A.4. Phonon calculations for this structure revealed an unstable A_{2g} ferroaxial soft mode with imaginary frequency, and the doubly degenerate $E_u(7)$ mode (24 THz) 4.3 that was resonantly driven in experiments.

Physical Property	**Site**	a (Å)/x	b (Å)/y	c (Å)/z
Lattice constants	/	5.65	5.65	7.20
Structural coordinates	Rb	0	0	1/2
	Fe	0	0	0
	2Mo	1/3	2/3	0.240
	$2O_a$	1/3	2/3	0.482
	$6O_p$	0.160	0.840	0.162

Table A.4: Relaxed lattice parameters of high-symmetry $RbFe(MoO_4)_2$.

To explore the ferroaxial low-temperature phase, a frozen-phonon approach was used by displacing the structure along the unstable A_{2g} mode. The resulting

double-well potential (Fig. A.1) indicates a structural instability toward a lower-symmetry $P\bar{3}$ ground state.

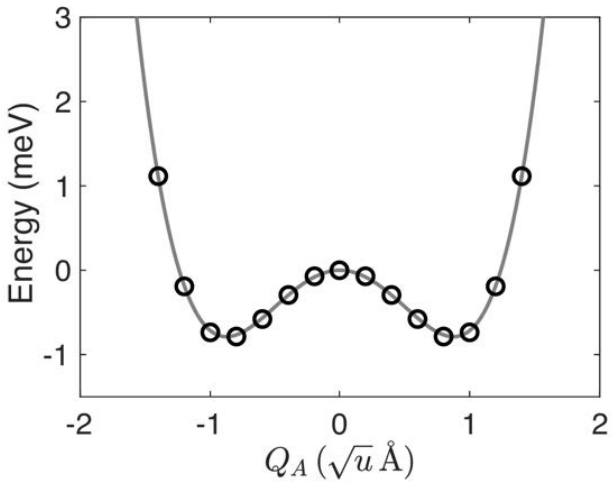

Figure A.1: Double-well potential energy of the A_{2g} ferroaxial mode in $RbFe(MoO_4)_2$. The two minima correspond to symmetry-broken configurations associated with the low-temperature $P\bar{3}$ phase, indicating a structural phase transition driven by the soft mode.

Finally, the coupling between the infrared-active E_u mode at 24 THz and the optically silent A_{2g} soft mode was quantified. The off-diagonal term of the mode-effective charge tensor as a function of the A_{2g} displacement was calculated, characterising the trilinear coupling term (Eq. 4.7) as $\alpha\,(\mathbf{Q}\times\mathbf{E})_z Q_A$. The resulting coupling coefficient $\alpha = 0.026\ q_e/\text{uÅ}$ gives rise to a tilted energy landscape for the axial order under circularly polarised excitation (Fig. 4.5).

La filosofia è scritta in questo grandissimo libro che continuamente ci sta aperto innanzi a gli occhi (io dico l'universo), ma non si può intendere se prima non s'impara a intender la lingua, e conoscer i caratteri ne' quali è scritto. Egli è scritto in lingua matematica.

Philosophy is written in this grand book—the universe—which stands continually open to our gaze, but it cannot be understood unless one first learns to comprehend the language in which it is written. It is written in the language of mathematics.

— Galileo Galilei, *Il Saggiatore* (1623)

The fundamental laws of nature are expressed in the language of mathematics.

— Paul A. M. Dirac

B

Data Analysis of Measurements on BPO_4

Contents

B.1 Permittivity and Optical Activity 74
B.2 Depth Dependence and Jones Matrix Analysis 76
B.3 Time Dependence and Functional Fits 77

In this appendix, the analysis procedure for the time-resolved polarisation rotation measurements on BPO_4 is presented.

B.1 Permittivity and Optical Activity

In the time-resolved experiments, the probe pulses propagate along the optical c-axis of the crystal, polarised in the a–b plane. The permittivity tensor elements along the crystal a- and b-axes are relevant and considered as follows.

Due to the $\bar{4}$ symmetry of BPO_4, the static permittivity in the a–b plane is isotropic:

$$\boldsymbol{\varepsilon} = \begin{pmatrix} \varepsilon_{11} & 0 \\ 0 & \varepsilon_{11} \end{pmatrix}. \tag{B.1}$$

Atomic displacements along the B-symmetry phonon modes induce both optical activity and birefringence. The birefringence shares the same symmetry as the B-mode displacements. The permittivity tensor including birefringence takes the symmetric form

$$\boldsymbol{\varepsilon}' = \begin{pmatrix} \varepsilon_{11} + \Delta\varepsilon_{11} & \Delta\varepsilon_{12} \\ \Delta\varepsilon_{12} & \varepsilon_{11} - \Delta\varepsilon_{11} \end{pmatrix}. \tag{B.2}$$

By rotating the coordinate frame around the c-axis, the tensor can be diagonalized as

$$\boldsymbol{\varepsilon}'' = \begin{pmatrix} \varepsilon_{11} - b & 0 \\ 0 & \varepsilon_{11} + b \end{pmatrix}, \qquad b = \sqrt{\Delta\varepsilon_{11}^2 + \Delta\varepsilon_{12}^2}. \tag{B.3}$$

Optical activity adds an imaginary antisymmetric component via the optical activity tensor element g_{33}:

$$\Delta\varepsilon_{ij}(\omega) = i\,\ell_{ijk}\,g_{kl}(\omega)\,k_l(\omega), \tag{B.4}$$

where ℓ_{ijk} is the Levi-Civita symbol and k is the wave vector. The probe, polarised in the a–b plane, is sensitive to g_{33}, which is zero at equilibrium and becomes nonzero when the B-mode is driven.

The modified permittivity tensor is then

$$\boldsymbol{\varepsilon}''' = \begin{pmatrix} \varepsilon_{11} - b & ic \\ -ic & \varepsilon_{11} + b \end{pmatrix}, \tag{B.5}$$

where c represents the effective optical activity and b the birefringence.

B.2 Depth Dependence and Jones Matrix Analysis

Due to the finite extinction depth δ of the THz excitation, the light-induced changes decay exponentially with depth:

$$\boldsymbol{\varepsilon}'''(z) = \begin{pmatrix} \varepsilon_{11} - b(0)e^{-z/\delta} & ic(0)e^{-z/\delta} \\ -ic(0)e^{-z/\delta} & \varepsilon_{11} + b(0)e^{-z/\delta} \end{pmatrix}. \tag{B.6}$$

Since the penetration depth of the 808 nm probe (≈5 mm) greatly exceeds the sample thickness, the measured signal represents an integration over the entire sample volume.

We employed Jones matrix analysis to separate contributions from optical activity and birefringence [111]. At equilibrium, the probe remains linearly polarised; after excitation, it decomposes into two elliptically polarised eigenmodes. Defining $f = c(0)/b(0)$, their eigenvectors are:

$$\mathbf{e}_1 = \begin{pmatrix} \dfrac{i(-1+\sqrt{1+f^2})}{f\sqrt{1+\frac{(-1+\sqrt{1+f^2})^2}{f^2}}} \\ \dfrac{1}{\sqrt{1+\frac{(-1+\sqrt{1+f^2})^2}{f^2}}} \end{pmatrix}, \qquad \mathbf{e}_2 = \begin{pmatrix} \dfrac{-i(1+\sqrt{1+f^2})}{f\sqrt{1+\frac{(1+\sqrt{1+f^2})^2}{f^2}}} \\ \dfrac{1}{\sqrt{1+\frac{(1+\sqrt{1+f^2})^2}{f^2}}} \end{pmatrix}. \tag{B.7}$$

The refractive indices for these eigenvectors are

$$n_{1,2} = \sqrt{\varepsilon_{11} \pm \sqrt{b(z)^2 + c(z)^2}}. \tag{B.8}$$

We note that the decay of the strength of the light-induced state over the extinction depth δ does not change the eigenvectors themselves, but only the difference in the splitting in the refractive indices (see Fig. B.1a).

The phase delay between them accumulates with propagation:

$$\frac{d\gamma}{dz} = \frac{2\pi}{\lambda_0}(n_1 - n_2) \approx \frac{2\pi}{\lambda_0 n_0}\sqrt{b^2 + c^2}. \tag{B.9}$$

Integrating over the entire sample thickness d, we acquire the phase difference between the two eigenvectors (see also Fig. B.1b)

$$\gamma = \frac{2\pi\delta}{\lambda_0 n_0}\sqrt{b(0)^2 + c(0)^2}\left(1 - e^{-d/\delta}\right). \tag{B.10}$$

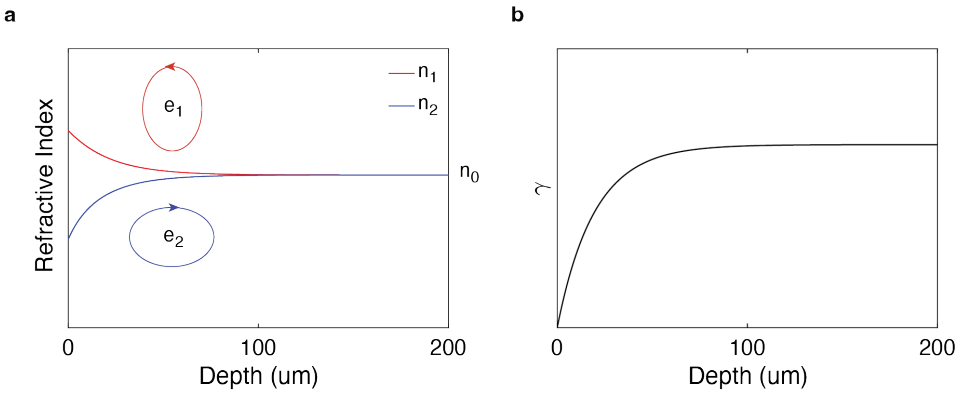

Figure B.1: Schematic of the light-induced polarisation rotation signal. (a) Refractive indices for the two elliptically polarised eigenvectors as a function of propagation depth in BPO_4. (b) Accumulated phase difference as a function of propagation depth.

B.3 Time Dependence and Functional Fits

After recombination and detection, the normalized polarisation rotation signal is

$$\theta(\phi) = \frac{I_1 - I_2}{2(I_1 + I_2)} = \frac{1}{2\sqrt{1 + 1/f^2}}\sin(\gamma) + \frac{\cos(\gamma) - 1}{4(1 + f^2)}\sin(4\phi - \varphi), \tag{B.11}$$

where ϕ is the incoming probe polarisation angle and φ is the angle between the pump and the optical axis of the transient birefringent state.

For small $\gamma \ll 1$, we expand $\sin\gamma \approx \gamma$ and $\cos\gamma \approx 1 - \gamma^2/2$, yielding:

$$\theta(\phi) = \frac{\pi\delta(1 - e^{-d/\delta})}{\lambda_0 n_0}\, c(0) - \frac{\pi^2\delta^2(1 - e^{-d/\delta})^2}{2\lambda_0^2 n_0^2}\, b(0)^2 \sin(4\phi). \tag{B.12}$$

The signal thus consists of two components: (i) a polarisation-independent term proportional to $c(0)$ (optical activity), and (ii) a four-fold symmetric term proportional to $b(0)^2$ (birefringence).

Averaging $\theta(\phi)$ over all probe polarisations removes the birefringence contribution, isolating $c(0)$.

Hence, the pure optical activity c is proportional to the average value of the polarisation rotation signal over all incoming probe polarisations. The pump-induced polarisation rotation $\theta(\phi)$ was fitted using the above expression at each time delay. The fitting results for the experimental data shown in Fig. 3.6B are presented in Fig. B.2.

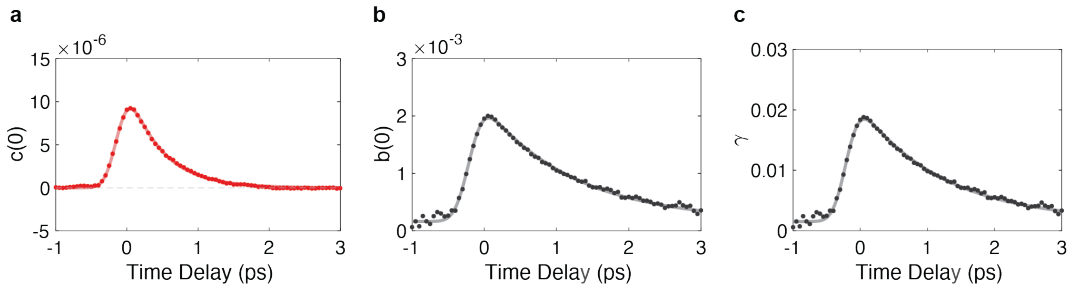

Figure B.2: Parameter fitting results Parameter fitting results for the polarisation rotation signal in Fig. 3.6. (a) Optical activity. (b) Birefringence. (c) Phase difference.

The rotary power ρ is defined as

$$\rho = \frac{\pi c}{\lambda_0 n_0}, \tag{B.13}$$

and the birefringence-induced refractive index difference as

$$\Delta n = \frac{2\pi b}{\lambda_0 n_0}. \tag{B.14}$$

The time-dependent rotary power, extracted from the experiments (Figs. 3.6c, 3.6e), was fitted using

$$\theta(t) = A\Big[\,\mathrm{erf}\left(\tfrac{t-t_0}{\sigma}\right) + 1\Big]e^{-t/\tau}, \tag{B.15}$$

where σ and τ represent the rise and decay times, respectively.

Figure B.3 illustrates the contribution to polarisation rotation signal from birefringence. When a linearly polarised pulse passes through a birefringent crystal, the outgoing beam becomes elliptically polarised. The projection on the x- and y-axes (the balancing axes for the incoming polarisation) will differ depending on the relative angle between the incoming polarisation and the fast axis of the birefringent material. The resulting signal exhibits a four-fold symmetry with respect to the incoming polarisation.

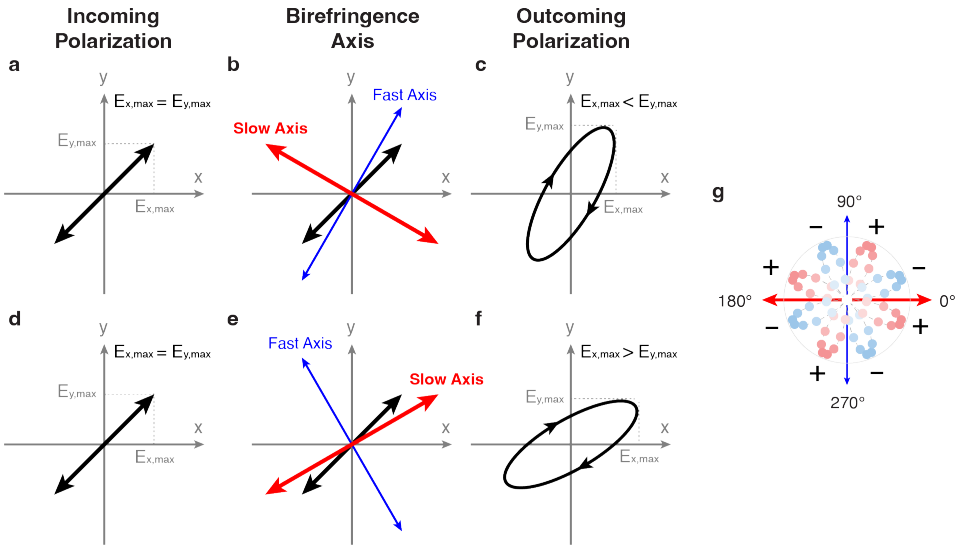

Figure B.3: Illustration of the birefringence contribution to the polarisation rotation signal. (a) Linearly polarised input. (b–f) Orientation of the birefringent axes relative to the input polarisation. (g) Polarisation rotation signal as a function of incident polarisation angle.

na kvacit pratiṣṭhitaṃ cittam utpādayitavyam.

应无所住，而生其心。

Let the mind arise without abiding anywhere.

— *The Diamond Sutra (Vajracchedikā Prajñāpāramitā Sūtra)*

C

Sample Preparation and Characterisation

Contents

C.1 BPO_4 . . . . . **80**

C.2 $RbFe(MoO_4)_2$ **81**

In this appendix, the procedure for sample preparation and characterisation is presented.

C.1 BPO_4

Polycrystalline BPO_4 powder was first synthesized using high-purity H_3BO_3 (99.9995%) and $NH_4H_2PO_4$ (99.998%) powders. The powders were ground, pelletized, and sintered. Single crystals were grown from this powder using Li_2MoO_4 flux via the top-seeded solution growth technique in a platinum crucible at temperatures up to 975 °C. After homogenization, the melt was slowly cooled, resulting in the growth of high-quality BPO_4 single crystals.

These crystals were characterised by x-ray diffractometry and oriented with

an optically flat (001) surface using focused ion beam (FIB) milling. Xenon ions were accelerated at 30 kV with a beam current of 2.5 mA for surface orientation. To reduce roughness, the sample was finally milled at grazing incidence with a beam current of 200 nA [112]. The thickness of the sample used in this experiment was approximately 200 µm.

The static optical properties in the THz frequency range were characterised by Fourier-transform infrared reflectivity (FTIR) measurements, with the light electric field polarised along the *a* axis.

C.2 $RbFe(MoO_4)_2$

Single-crystal $RbFe(MoO_4)_2$ was grown using the flux method and characterised by x-ray diffractometry. A sample with an optically flat *c*-cut surface and a thickness of approximately 200 µm was used in the experiment. During the measurements, the sample was cooled and heated at a slow rate of 0.1 K/min near the 190 K ferroaxial phase transition temperature.

The static optical properties in the THz frequency range were characterised by Fourier-transform infrared reflectivity (FTIR) measurements, with the light electric field polarised in the crystal *ab* plane. As shown in Figure C.1, four E_u-symmetry optical phonon modes of $RbFe(MoO_4)_2$ were observed in the reflectivity spectrum, which was fitted using the dielectric function for infrared-active phonons 3.6.

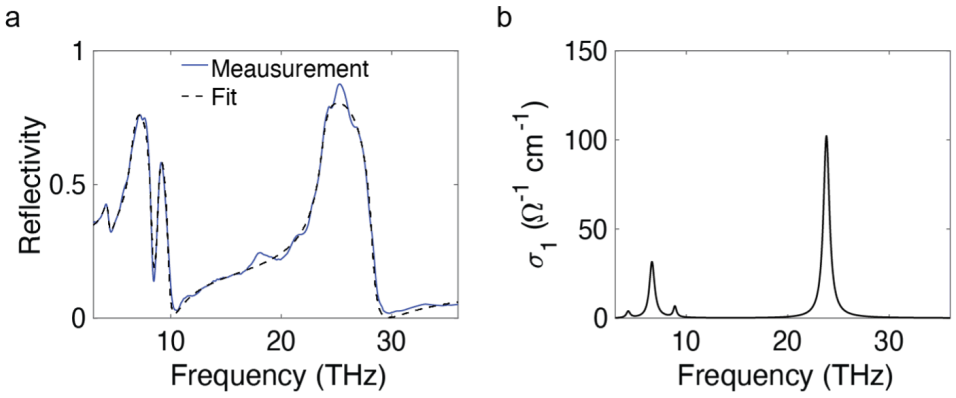

Figure C.1: Static optical characterisation of the $RbFe(MoO_4)_2$ sample. (a) Measured reflectivity spectrum in the THz range with the electric field polarised in the crystal ab-plane, along with the corresponding fit. (b) Frequency dependent real part of the optical conductivity extracted from the fit.

The results of this fit are summarized in Table C.1, where the numbering of the modes follows that in Table 4.3. The $E_u(7)$ mode at 24 THz was resonantly excited in the experiments.

Phonon Mode	$\omega_{\mathrm{TO},j}/2\pi$ (THz)	$\omega_{\mathrm{LO},j}/2\pi$ (THz)	$\gamma_j/2\pi$ (THz)	ε_∞
$E_u(3)$	4.3	4.8	0.45	/
$E_u(4)$	6.6	9.9	0.61	/
$E_u(5)$	8.9	9.2	0.38	/
$E_u(5)$	23.8	27.8	0.72	/
/	/	/	/	4.01

Table C.1: Fitted parameters of the infrared-active E_u phonon modes of $RbFe(MoO_4)_2$.

If I have seen further, it is by standing on the shoulders of giants.

— Isaac Newton

References

[1] Lev Davidovich Landau and Evgenii Mikhailovich Lifshitz. *Statistical Physics: Volume 5*. Vol. 5. Elsevier, 2013.

[2] Pierre Curie. "Sur la symétrie dans les phénomènes physiques, symétrie d'un champ électrique et d'un champ magnétique". In: *Journal de physique théorique et appliquée* 3.1 (1894), pp. 393–415.

[3] Masatoshi Imada, Atsushi Fujimori, and Yoshinori Tokura. "Metal-insulator transitions". In: *Reviews of modern physics* 70.4 (1998), p. 1039.

[4] Eduardo Fradkin et al. "Nematic Fermi fluids in condensed matter physics". In: *Annu. Rev. Condens. Matter Phys.* 1.1 (2010), pp. 153–178.

[5] Bernhard Keimer et al. "From quantum matter to high-temperature superconductivity in copper oxides". In: *Nature* 518.7538 (2015), pp. 179–186.

[6] Lev Davidovich Landau. "On the theory of phase transitions". In: *Zh. eksp. teor. Fiz* 7.19-32 (1937), p. 926.

[7] Elbio Dagotto. "Complexity in strongly correlated electronic systems". In: *Science* 309.5732 (2005), pp. 257–262.

[8] Darrell G Schlom et al. "Elastic strain engineering of ferroic oxides". In: *Mrs Bulletin* 39.2 (2014), pp. 118–130.

[9] Jochen Mannhart and Darrell G Schlom. "Oxide interfaces—an opportunity for electronics". In: *Science* 327.5973 (2010), pp. 1607–1611.

[10] Harold Y Hwang et al. "Emergent phenomena at oxide interfaces". In: *Nature materials* 11.2 (2012), pp. 103–113.

[11] DN Basov, RD Averitt, and D Hsieh. "Towards properties on demand in quantum materials". In: *Nature materials* 16.11 (2017), pp. 1077–1088.

[12] Ankit S Disa, Tobia F Nova, and Andrea Cavalleri. "Engineering crystal structures with light". In: *Nature Physics* 17.10 (2021), pp. 1087–1092.

[13] Daniele Fausti et al. "Light-induced superconductivity in a stripe-ordered cuprate". In: *science* 331.6014 (2011), pp. 189–191.

[14] Roman Mankowsky et al. "Ultrafast reversal of the ferroelectric polarization". In: *Physical review letters* 118.19 (2017), p. 197601.

[15] Ankit S Disa et al. "Polarizing an antiferromagnet by optical engineering of the crystal field". In: *Nature Physics* 16.9 (2020), pp. 937–941.

[16] Alaska Subedi, Andrea Cavalleri, and Antoine Georges. "Theory of nonlinear phononics for coherent light control of solids". In: *Physical Review B* 89.22 (2014), p. 220301.

[17] Martin Dressel and George Grüner. *Electrodynamics of solids: optical properties of electrons in matter*. Cambridge university press, 2002.

[18] Max Born and Kun Huang. "Dynamical theory of crystal lattices Oxford University Press". In: *London, New York* (1954), pp. 160–173.

[19] KUN Huang. "Lattice vibrations and optical waves in ionic crystals". In: *Nature* 167.4254 (1951), pp. 779–780.

[20] Michael Först et al. "Nonlinear phononics as an ultrafast route to lattice control". In: *Nature Physics* 7.11 (2011), pp. 854–856.

[21] Michael Först et al. "Displacive lattice excitation through nonlinear phononics viewed by femtosecond X-ray diffraction". In: *Solid State Communications* 169 (2013), pp. 24–27.

[22] Dominik Maximilian Juraschek, Michael Fechner, and Nicola Ann Spaldin. "Ultrafast structure switching through nonlinear phononics". In: *Physical review letters* 118.5 (2017), p. 054101.

[23] Paolo G Radaelli. "Breaking symmetry with light: Ultrafast ferroelectricity and magnetism from three-phonon coupling". In: *Physical Review B* 97.8 (2018), p. 085145.

[24] Sebastian Maehrlein et al. "Terahertz sum-frequency excitation of a Raman-active phonon". In: *Physical review letters* 119.12 (2017), p. 127402.

[25] Dominik M Juraschek and Sebastian F Maehrlein. "Sum-frequency ionic Raman scattering". In: *Physical Review B* 97.17 (2018), p. 174302.

[26] Michael Kozina et al. "Terahertz-driven phonon upconversion in SrTiO3". In: *Nature Physics* 15.4 (2019), pp. 387–392.

[27] Mingqiang Gu and James M Rondinelli. "Coupled Raman-Raman modes in the ionic Raman scattering process". In: *Applied Physics Letters* 113.11 (2018).

[28] Andrea Cartella et al. "Parametric amplification of optical phonons". In: *Proceedings of the National Academy of Sciences* 115.48 (2018), pp. 12148–12151.

[29] A. von Hoegen et al. "Probing the interatomic potential of solids with strong-field nonlinear phononics". In: *Nature* 555.7694 (2018), pp. 79–+.

[30] Blake S Dastrup, Jacob R Hall, and Jeremy A Johnson. "Experimental determination of the interatomic potential in LiNbO3 via ultrafast lattice control". In: *Applied Physics Letters* 110.16 (2017).

[31] Roman Mankowsky et al. "Nonlinear lattice dynamics as a basis for enhanced superconductivity in YBa2Cu3O6. 5". In: *Nature* 516.7529 (2014), pp. 71–73.

[32] Meredith Henstridge et al. "Nonlocal nonlinear phononics". In: *Nature Physics* 18.4 (2022), pp. 457–461.

[33] T Mertelj and VV Kabanov. "Comment on "ultrafast reversal of the ferroelectric polarization"". In: *Physical Review Letters* 123.12 (2019), p. 129701.

[34] Daniele Nicoletti and Andrea Cavalleri. "Nonlinear light–matter interaction at terahertz frequencies". In: *Advances in Optics and Photonics* 8.3 (2016), pp. 401–464.

[35] SA Zvyagin et al. "Terahertz-range free-electron laser electron spin resonance spectroscopy: techniques and applications in high magnetic fields". In: *Review of Scientific Instruments* 80.7 (2009).

[36] Alexander Sell, Alfred Leitenstorfer, and Rupert Huber. "Phase-locked generation and field-resolved detection of widely tunable terahertz pulses with amplitudes exceeding 100 MV/cm". In: *Optics letters* 33.23 (2008), pp. 2767–2769.

[37] R Baumgartner and Robert Byer. "Optical parametric amplification". In: *IEEE Journal of Quantum Electronics* 15.6 (1979), pp. 432–444.

[38] Robert W Boyd, Alexander L Gaeta, and Enno Giese. "Nonlinear optics". In: *Springer Handbook of Atomic, Molecular, and Optical Physics*. Springer, 2008, pp. 1097–1110.

[39] Matthias C Hoffmann and József András Fülöp. "Intense ultrashort terahertz pulses: generation and applications". In: *Journal of Physics D: Applied Physics* 44.8 (2011), p. 083001.

[40] Charles V Shank. "Investigation of ultrafast phenomena in the femtosecond time domain". In: *Science* 233.4770 (1986), pp. 1276–1280.

[41] Qi Wu and X-C Zhang. "Free-space electro-optic sampling of terahertz beams". In: *Applied Physics Letters* 67.24 (1995), pp. 3523–3525.

[42] Jean-Louis Coutaz, Frederic Garet, and Vincent Wallace. *Principles of Terahertz time-domain spectroscopy*. CRC Press, 2018.

[43] Kai Liu, Jingzhou Xu, and X-C Zhang. "GaSe crystals for broadband terahertz wave detection". In: *Applied physics letters* 85.6 (2004), pp. 863–865.

[44] C Kübler et al. "Ultrabroadband detection of multi-terahertz field transients with GaSe electro-optic sensors: Approaching the near infrared". In: *Applied physics letters* 85.16 (2004), pp. 3360–3362.

[45] Nick CJ Van der Valk, Willemine AM van der Marel, and Paul CM Planken. "Terahertz polarization imaging". In: *Optics letters* 30.20 (2005), pp. 2802–2804.

[46] Ranxi Zhang et al. "Polarization information for terahertz imaging". In: *Applied Optics* 47.34 (2008), pp. 6422–6427.

[47] Natsuki Nemoto et al. "Highly precise and accurate terahertz polarization measurements based on electro-optic sampling with polarization modulation of probe pulses". In: *Optics Express* 22.15 (2014), pp. 17915–17929.

[48] Maximilian Frenzel et al. "Quartz as an accurate high-field low-cost THz helicity detector". In: *Optica* 11.3 (2024), pp. 362–370.

[49] William Lawrence Bragg. "The structure of some crystals as indicated by their diffraction of X-rays". In: *Proceedings of the Royal Society of London. Series A, Containing papers of a mathematical and physical character* 89.610 (1913), pp. 248–277.

[50] Yvon Le Page and Gabrielle Donnay. "Refinement of the crystal structure of low-quartz". In: *Acta Crystallographica Section B: Structural Crystallography and Crystal Chemistry* 32.8 (1976), pp. 2456–2459.

[51] Ben L Feringa and Richard A Van Delden. "Absolute asymmetric synthesis: the origin, control, and amplification of chirality". In: *Angewandte Chemie International Edition* 38.23 (1999), pp. 3418–3438.

[52] Zhihua Li et al. "Crystal growth, optical properties measurement, and theoretical calculation of BPO4". In: *Chemistry of materials* 16.15 (2004), pp. 2906–2908.

[53] Gerhard H Fecher, Jürgen Kübler, and Claudia Felser. "Chirality in the solid state: Chiral crystal structures in chiral and achiral space groups". In: *Materials* 15.17 (2022), p. 5812.

[54] François Arago. *Sur une modification remarquable qu'éprouvent les rayons lumineux dans leur passage à travers certains corps diaphanes, et sur quelques autres nouveaux phénomènes d'optiques: lu le 11 août 1811*. Firmin-Didot, 1812.

[55] Jean-Baptiste Biot. *Mémoire sur un nouveau genre d'oscillation que les molécules de la lumiere éprouvent en traversant certains cristaux*. Chez Firmin Didot, 1814.

[56] AS Barker Jr. "Temperature Dependence of the Transverse and Longitudinal Optic Mode Frequencies and Charges in SrTi O 3 and BaTi O 3". In: *Physical Review* 145.2 (1966), p. 391.

[57] Cristian Manzoni et al. "Single-shot detection and direct control of carrier phase drift of midinfrared pulses". In: *Optics letters* 35.5 (2010), pp. 757–759.

[58] Makoto Kuwata-Gonokami et al. "Giant optical activity in quasi-two-dimensional planar nanostructures". In: *Physical review letters* 95.22 (2005), p. 227401.

[59] Carsten Rockstuhl et al. "Optical activity in chiral media composed of three-dimensional metallic meta-atoms". In: *Physical Review B* 79.3 (2009), p. 035321.

[60] Mariastefania De Vido et al. "Optical rotatory power of quartz between 77 K and 325 K for 1030 nm wavelength". In: *Optical Materials Express* 9.6 (2019), pp. 2708–2715.

[61] Michael Först et al. "Spatially resolved ultrafast magnetic dynamics initiated at a complex oxide heterointerface". In: *Nature materials* 14.9 (2015), pp. 883–888.

[62] Dmytro Afanasiev et al. "Ultrafast control of magnetic interactions via light-driven phonons". In: *Nature Materials* 20.5 (2021), pp. 607–611.

[63] A Stupakiewicz et al. “Ultrafast phononic switching of magnetization”. In: *Nature Physics* 17.4 (2021), pp. 489–492.

[64] Sebastian Fava et al. “Magnetic field expulsion in optically driven YBa2Cu3O6. 48”. In: *Nature* (2024), pp. 1–6.

[65] Holger Bech Nielsen and Masao Ninomiya. “The Adler-Bell-Jackiw anomaly and Weyl fermions in a crystal”. In: *Physics Letters B* 130.6 (1983), pp. 389–396.

[66] AA Zyuzin and AA Burkov. “Topological response in Weyl semimetals and the chiral anomaly”. In: *Physical Review B* 86.11 (2012), p. 115133.

[67] NP Ong and Sihang Liang. “Experimental signatures of the chiral anomaly in Dirac–Weyl semimetals”. In: *Nature Reviews Physics* 3.6 (2021), pp. 394–404.

[68] J Ishioka et al. “Chiral charge-density waves”. In: *Physical review letters* 105.17 (2010), p. 176401.

[69] Su-Yang Xu et al. “Spontaneous gyrotropic electronic order in a transition-metal dichalcogenide”. In: *Nature* 578.7796 (2020), pp. 545–549.

[70] Wencan Jin et al. “Observation of a ferro-rotational order coupled with second-order nonlinear optical fields”. In: *Nature Physics* 16.1 (2020), pp. 42–46.

[71] AF Andreev and IA Grishchuk. “Spin nematics”. In: *Sov. Phys. JETP* 60.2 (1984), p. 267.

[72] VM Dubovik, LA Tosunyan, and VV Tugushev. “Axial toroidal moments in electrodynamics and solid-state physics”. In: *Zh. Eksp. Teor. Fiz* 90.2 (1986), pp. 590–605.

[73] RD Johnson et al. “Cu 3 Nb 2 O 8: a multiferroic with chiral coupling to the crystal structure”. In: *Physical review letters* 107.13 (2011), p. 137205.

[74] RD Johnson et al. “Giant improper ferroelectricity in the ferroaxial magnet CaMn 7 O 12”. In: *Physical review letters* 108.6 (2012), p. 067201.

[75] J Hlinka et al. “Symmetry guide to ferroaxial transitions”. In: *Physical review letters* 116.17 (2016), p. 177602.

[76] Sang-Wook Cheong et al. “Broken symmetries, non-reciprocity, and multiferroicity”. In: *npj Quantum Materials* 3.1 (2018), pp. 1–7.

[77] Sang-Wook Cheong. “SOS: symmetry-operational similarity”. In: *npj Quantum Materials* 4.1 (2019), pp. 1–9.

[78] T Hayashida et al. “Visualization of ferroaxial domains in an order-disorder type ferroaxial crystal”. In: *Nature communications* 11.1 (2020), pp. 1–8.

[79] T Hayashida et al. “Phase transition and domain formation in ferroaxial crystals”. In: *Physical Review Materials* 5.12 (2021), p. 124409.

[80] Hiroko Yokota et al. “Three-dimensional imaging of ferroaxial domains using circularly polarized second harmonic generation microscopy”. In: *npj Quantum Materials* 7.1 (2022), pp. 1–6.

[81] Gan Liu et al. “Electrical switching of ferro-rotational order in nanometre-thick 1T-TaS2 crystals”. In: *Nature Nanotechnology* (2023), pp. 1–7.

[82] Ken-ichi Uchida and Joseph P Heremans. “Thermoelectrics: From longitudinal to transverse”. In: *Joule* 6.10 (2022), pp. 2240–2245.

[83] A Hunter et al. “Non-Fermi liquid quasiparticles in strain-tuned Sr2RuO4”. In: *arXiv preprint arXiv:2503.11311* (2025).

[84] Renliang Yuan et al. “Identification and mechanical control of ferroelastic domain structure in rhombohedral CaMn 7 O 12”. In: *Physical Review B* 91.5 (2015), p. 054102.

[85] Dominik M Juraschek et al. “Dynamical multiferroicity”. In: *Physical Review Materials* 1.1 (2017), p. 014401.

[86] Jiaming Luo et al. “Large effective magnetic fields from chiral phonons in rare-earth halides”. In: *Science* 382.6671 (2023), pp. 698–702.

[87] Martina Basini et al. “Terahertz electric-field driven dynamical multiferroicity in SrTiO3”. In: *Nature* 628 (2024), pp. 534–539.

[88] CS Davies et al. “Phononic switching of magnetization by the ultrafast Barnett effect”. In: *Nature* 628 (2024), pp. 540–544.

[89] Zhiren He and Guru Khalsa. “Optical control of ferroaxial order”. In: *Physical Review Research* 6.4 (2024), p. 043220.

[90] M Mączka et al. “Pressure-induced phase transitions in multiferroic RbFe (MoO4) 2—Raman scattering study”. In: *Journal of Solid State Chemistry* 184.10 (2011), pp. 2812–2817.

[91] SA Klimin et al. “Structural phase transition in the two-dimensional triangular lattice antiferromagnet RbFe (MoO 4) 2”. In: *Physical Review B* 68.17 (2003), p. 174408.

[92] Malcolm E Lines and Alastair M Glass. *Principles and applications of ferroelectrics and related materials*. Oxford university press, 2001.

[93] Charles Kittel and Paul McEuen. *Introduction to solid state physics*. John Wiley Sons, 2018.

[94] David R Gaskell and David E Laughlin. *Introduction to the Thermodynamics of Materials*. CRC press, 2024.

[95] Zeeshan H Amber et al. “Quantifying the coherent interaction length of second-harmonic microscopy in lithium niobate confined nanostructures”. In: *Journal of Applied Physics* 130.13 (2021).

[96] Yiping Wang et al. “Axial Higgs mode detected by quantum pathway interference in RTe3”. In: *Nature* 606.7916 (2022), pp. 896–901.

[97] Yoichi Kajita et al. “Ferroaxial Transitions in Glaserite-Type Na2BaM (PO4) 2 (M= Mg, Mn, Co, and Ni)”. In: *Chemistry of Materials* (2024).

[98] Junjie Yang, Fei-Ting Huang, and Sang-Wook Cheong. "Unlocking magnetic ferro-rotational functionalities". In: *Journal of Physics: Condensed Matter* (2025).

[99] Anne S Zimmermann, Dennis Meier, and Manfred Fiebig. "Ferroic nature of magnetic toroidal order". In: *Nature communications* 5.1 (2014), p. 4796.

[100] Satoru Hayami, Rikuto Oiwa, and Hiroaki Kusunose. "Electric ferro-axial moment as nanometric rotator and source of longitudinal spin current". In: *Journal of the Physical Society of Japan* 91.11 (2022), p. 113702.

[101] Satoru Hayami, Rikuto Oiwa, and Hiroaki Kusunose. "Unconventional Hall effect and magnetoresistance induced by metallic ferroaxial ordering". In: *Physical Review B* 108.8 (2023), p. 085124.

[102] AS Disa et al. "Photo-induced high-temperature ferromagnetism in YTiO3". In: *Nature* 617.7959 (2023), pp. 73–78.

[103] Batyr Ilyas et al. "Terahertz field-induced metastable magnetization near criticality in FePS3". In: *Nature* 636.8043 (2024), pp. 609–614.

[104] Georg Kresse and Jürgen Furthmüller. "Efficiency of ab-initio total energy calculations for metals and semiconductors using a plane-wave basis set". In: *Computational materials science* 6.1 (1996), pp. 15–50.

[105] Georg Kresse and Jürgen Hafner. "Ab initio molecular dynamics for liquid metals". In: *Physical review B* 47.1 (1993), p. 558.

[106] Georg Kresse and Jürgen Furthmüller. "Efficient iterative schemes for ab initio total-energy calculations using a plane-wave basis set". In: *Physical review B* 54.16 (1996), p. 11169.

[107] Atsushi Togo. "First-principles phonon calculations with phonopy and phono3py". In: *Journal of the Physical Society of Japan* 92.1 (2023), p. 012001.

[108] G. Kresse and D. Joubert. "From ultrasoft pseudopotentials to the projector augmented-wave method". In: *Physical Review B* 59.3 (1999). PRB, pp. 1758–1775.

[109] Hendrik J Monkhorst and James D Pack. "Special points for Brillouin-zone integrations". In: *Physical review B* 13.12 (1976), p. 5188.

[110] M Gajdoš et al. "Linear optical properties in the projector-augmented wave methodology". In: *Physical Review B—Condensed Matter and Materials Physics* 73.4 (2006), p. 045112.

[111] R Clark Jones. "A new calculus for the treatment of optical systemsi. description and discussion of the calculus". In: *Josa* 31.7 (1941), pp. 488–493.

[112] Philip JW Moll. "Focused ion beam microstructuring of quantum matter". In: *Annual Review of Condensed Matter Physics* 9 (2018), pp. 147–162.